DOCTORAL THESIS

Synthesis and Characterization of Pyrite FeS$_2$ Microcrystals for Photovoltaic Applications

Katriin Reedo

Synthesis and Characterization of Pyrite FeS$_2$ Microcrystals for Photovoltaic Applications

KATRIIN REEDO

TAL TECH PRESS

TALLINN UNIVERSITY OF TECHNOLOGY
School of Engineering
Department of Materials and Environmental Technology
The dissertation was accepted for the defence of the degree of Doctor of Philosophy on 14. January 2026

Supervisor: Dr. Taavi Raadik
                     Department of Materials and Environmental Technology
                     Tallinn University of Technology
                     Tallinn, Estonia

Co-supervisors: Dr. Mare Altosaar
                     Department of Materials and Environmental Technology
                     Tallinn University of Technology
                     Tallinn, Estonia

                     Dr. Advenit Makaya
                     European Space Research and Technology Centre
                     European Space Agency
                     Noordwijk, the Netherlands

Opponents: Dr. Rokas Kondrotas
                     Department of Characterisation of Materials Structure
                     Center for Physical Sciences and Technology (FTMC)
                     Vilnius, Lithuania

                     Prof. Vambola Kisand
                     Institute of Physics
                     University of Tartu
                     Tartu, Estonia

Defence of the thesis: 26. February 2026, Tallinn
Declaration:
Hereby I declare that this doctoral thesis, my original investigation and achievement, submitted for the doctoral degree at Tallinn University of Technology, has not been submitted for any academic degree elsewhere.

Katriin Reedo

_____
                                          signature

Püriitsete FeS$_2$ mikrokristallide süntees ja iseloomustamine päikesepatareides kasutamiseks

KATRIIN REEDO

Contents

List of Publications

The present Ph.D. thesis is based on the following publications that are referred to in the text by Roman numbers.

I **K. Kristmann***, M. Altosaar, J Raudoja, J. Krustok, M. Pilvet, V. Mikli, M. Grossberg, M. Danilson, T. Raadik. "Pyrite as prospective absorber material for monograin layer solar cell", Thin Solid Films, 743, 139068, 2022. DOI: 10.1016/j.tsf.2021.139068

II **K. Kristmann***, T. Raadik, M. Altosaar, M. Grossberg-Kuusk, J. Krustok, M. Pilvet, V. Mikli, M. Kauk-Kuusik, A. Makaya. "Pyrite as promising monograin layer solar cell absorber material for in-situ solar cell fabrication on the Moon", *Acta Astronautica*, 199, 420-424, 2022. DOI: 10.1016/j.actaastro.2022.07.043

III **K. Kristmann***, T. Raadik, M. Altosaar, M. Danilson, J. Krustok, P. Paaver, Y. Butenko. "Characterization of FeS_2 pyrite microcrystals synthesized in different flux media", *Materials Advances*, 5, 1565, 2024. DOI: 10.1039/d3ma00697b

IV **K. Reedo***, T. Raadik, M. Altosaar, A. Gutjuma, P. Paaver. "Scalable Phosphorus Doping of p-Type FeS_2 Microcrystals for Photovoltaic Applications", *ACS Omega*, 2025. DOI: 10.1021/acsomega.5c07455

In addition, the author has contributed to a patent application based on the technology developed in the frames of the doctoral studies:

K. Reedo*, T. Raadik, M. Altosaar, A. Gutjuma. "Meetod p-tüüpi juhtivusega püriidi mikrokristallide valmistamiseks", Application P202500042 for Estonian patent.

Author's Contributions to the Publications

I   Synthesis of the pyrite materials, fabrication of the Schottky diodes, characterization of materials by scanning electron microscopy, Raman spectroscopy, X-ray diffraction, and I-V curves. Analysis and visualization of the results, part of the writing, and a major part of the revision.

II Synthesis of the pyrite microcrystals, fabrication of the Schottky diodes, characterization of materials by scanning electron microscopy, Raman spectroscopy, X-ray diffraction, and I-V curves, analysis and visualization of the results, and a major part of the writing.

III Synthesis of the pyrite microcrystals in different molten salt media, characterization of materials by scanning electron microscopy, sieving analysis, Raman spectroscopy, X-ray diffraction, time-of-flight secondary ion mass spectroscopy. Analysis and visualization of the results, and a major part of the writing.

IV Synthesis of the pyrite microcrystals, post-treatments and recrystallization of the materials, characterization of materials by scanning electron microscopy, hot probe measurements, and Raman spectroscopy. Analysis and visualization of the results, and a major part of the writing.

Introduction

Global electricity demand is growing at an unprecedented rate following the post-COVID recovery, with an annual increase of approximately 4% [1]. A significant portion of this growth can be attributed to the rising energy consumption of artificial intelligence data centers and increasingly frequent heat waves across the globe. In 2024, renewable energy accounted for less than 34% of the global electricity supply, with the majority of electrical power still delivered by nonrenewable sources such as coal, gas, nuclear, and oil [2]. Utilizing sustainable and renewable energy sources is essential for mitigating the impacts of the global climate crisis.

Solar energy is considered one of the most promising renewable energy sources due to its vast and virtually inexhaustible reserves. Solar energy can be converted into electricity through solar panels, which offer several advantages, including the absence of moving parts and minimal maintenance requirements [3]. The global installed capacity of solar energy grew by 520 GW in 2024, and is expected to make up 80% of the total global renewable electricity capacity increase in the coming years [3,4]. The total global capacity of solar energy production has now reached over 2.2 TW [5], which makes up about 26.7% of the total share of renewable electricity produced in 2024 [3].

97% of the solar energy technologies are based on crystalline silicon, which is a widely researched material with solar cell efficiencies nearing the theoretical efficiency maximum of 31% [6]. The increase in solar energy capacity is set to double over the next five years, increasing the need for Si materials [3]. Silicon is also a key material in the electronics industry and in solar panels that are used in space applications. Growing demand has led to higher raw material costs of Si [7]. As a result, there has been significant research focused on discovering cost-effective alternatives for use in solar cells. Suitable alternative solar energy materials must be available in abundance, be non-toxic for the environment, and deliver similar power conversion efficiencies in devices.

Pyrite FeS_2 has emerged as a promising candidate for low-cost and environmentally sustainable solar cells. The widespread availability of iron and sulfur, coupled with the ability to process FeS_2 at significantly lower temperatures than silicon, offers the potential for the most cost-effective electricity production among all known solar cell materials [8]. FeS_2 is a semiconductor with a simple cubic crystal lattice, a suitable band gap of around 0.95 eV, and an exceptionally high light absorption coefficient in the visible range - $\alpha > 10^5$ cm^{-1} for hν > 1.3 eV, enabling to absorb more than 90% of sunlight in a 100 nm thick pyrite layer [9, 10]. These characteristics make pyrite solar cells theoretically capable of achieving efficiencies as high as 25%. Due to its promising efficiency and low cost, FeS_2 has been considered for extraterrestrial applications, with ongoing research focused on developing solar cell technologies for future lunar habitats. As part of NASA and the European Space Agency's Artemis missions, research efforts are being focused on establishing a sustainable human presence on the Moon while using as many locally available materials as possible — a process known as *in-situ* resource utilization (ISRU) [11]. A key challenge in this endeavor is the development of reliable energy systems to support lunar infrastructure. Given that solar energy is the most accessible and abundant power source on the Moon, this study, in collaboration with the European Space Agency, explores the potential of pyrite-based solar cells as a sustainable energy solution for lunar applications.

Despite intermittent research efforts over several decades, the efficiency of pyrite solar cells has not exceeded 3% [10, 12]. The efficiency deficit has been attributed to the low open circuit voltage (V_{OC}) of the pyrite devices and the so-called surface inversion phenomenon. The surface of pyrite has been demonstrated to exhibit lattice

contortions with broken sulfur bonds, causing the iron ion in the pyrite lattice to change its coordination from the Fe 3d state and split into four energy levels, including levels inside the band gap [10, 13]. This, together with the pinning of the Fermi level, creates a leaky internal barrier within the pyrite crystal, with the surface exhibiting p-type conductivity and the bulk n-type conductivity.

Sulfur vacancies have been identified as another important variable in producing high-quality pyrite absorber material. Pyrite's n-type bulk is unintentionally doped by these vacancies, which act as deep donors [14, 15]. The concentration of S vacancies and thus the electronic transport properties of pyrite can be adjusted during crystal growth by varying the sulfur vapor pressure, with higher sulfur pressures leading to fewer vacancies. However, a discrepancy remains between theory and experiment. Individual sulfur vacancies have high calculated formation energies, yet experiments show they are abundant [16]. Density functional theory suggests that vacancy clusters have lower formation enthalpies, and a tetra-vacancy complex with high binding energy has been proposed. Such clusters may therefore explain the observed n-type doping in pyrite.

The majority of previous research in pyrite devices concerns thin film applications where the properties of the pyrite surface are more prevalent compared to the bulk. Doping pyrite with halogens, which behave as donors, has been attempted to control its electrical properties better [17]. Doping and alloying with transition metals has been demonstrated to tune the band gap of pyrite [18, 19] while As-, Se-, and Te-substituted pyrites have been shown to exhibit p-type conductivity [20]. Voigt et al. [21] were the first who demonstrated p-type doping of pyrite crystals with phosphorus in 2023. However, a significant research gap remains in understanding the effect and control of impurities and the behavior of the inverse surface layer in pyrite.

The novelty of this study is in the synthesis-growth of individual pyrite microcrystals to further utilize the crystals as the absorber of a monograin layer solar cell. Synthesis conditions to obtain FeS_2 microcrystals with suitable morphology are identified. Different molten fluxes, such as sulfur, KI, LiI, CsI, and Na_2S_x, and different synthesis temperatures are compared. The effect of alkali metal impurities in pyrite is addressed as a research gap in the doping studies of pyrite. It is found that impurities in the bulk of the material have a strong effect on the recombination mechanisms of the charge carriers in pyrite, as well as on the height of the valence band maximum and the position of the Fermi level. Lastly, phosphorus-doping is addressed as one of the most promising strategies to obtain thoroughly p-type pyrite crystals with uniform properties. A unique approach to phosphorus doping is developed that allows the treatment of thousands of crystals simultaneously.

This thesis comprises three chapters and is based on four publications. The first chapter gives a literature overview of the existing photovoltaic technologies and the monograin layer solar cell technology that is central to this study. State-of-the-art research on FeS_2 solar cells is outlined, with research gaps identified. The experimental procedure and characterization methods are described in the second chapter. The third chapter presents the results and discussion of the experimental work, including the findings of the four research papers this thesis is based on. The last section of the chapter concludes this thesis.

Abbreviations, terms and symbols

α	Light absorption coefficient
CIGS	$Cu(In, Ga)Se_2$
C-V	Capacitance-voltage
DSSC	Dye-sensitized solar cells
E_{CBM}	Energy of the conduction band minimum
E_{cutoff}	Secondary electron cutoff energy
EDX	Energy dispersive X-ray spectroscopy
E_F	Energy of the Fermi level
E_i	Activation energy of donors
ESA	European Space Agency
E_{VBM}	Energy of the valence band maximum
HR-SEM	High-resolution scanning electron microscopy
$h\nu$	Energy of a photon
ICPMS	Inductively coupled plasma mass spectrometry
ISRU	*in-situ* resource utilization
I-V	Current-voltage
J_{SC}	Short-circuit current density
MEH-PPV	Poly[2-methoxy-5-(2-ethylhexyloxy)-1,4-phenylene-vinylene]
MGL	Monograin layer
NASA	National Aeronautics and Space Administration
N_D	Bulk donor concentration
OSC	Organic solar cells
P3HT	Poly(3-hexylthiophene)
PCBM	[6,6]-phenyl-C61-butyric acid methyl ester
PCE	Power conversion efficiency
PEC	Photoelectrochemical
PEDOT:PSS	Poly(3,4-ethylenedioxythiophene) polystyrene sulfonate
PL	Photoluminescence
ppm	Parts per million
PV	Photovoltaics
RT	Room temperature
TCO	Transparent conductive oxide
ToF-SIMS	Time-of-flight secondary ion mass spectrometry
UPS	Ultraviolet photoelectron spectroscopy
UV	Ultraviolet
V_{OC}	Open-circuit voltage
XPS	X-ray photoelectron spectroscopy
XRD	X-ray diffraction
ϕ	Work function
ψ	Band bending, calculated from the wave function

1 Literature Review

1.1 Photovoltaic technologies and absorber materials

Over the past 70 years, photovoltaic (PV) or solar energy technologies have made significant advancements, with several technologies now approaching their theoretical efficiency limits. The maximum efficiency of a solar cell, known as the Shockley–Queisser limit, is determined by the band gap of the absorber material. Silicon, which currently dominates approximately 97% of the solar energy market, benefits from a nearly ideal band gap of 1.1 eV and has achieved a record efficiency of 27.8% [22]. With global PV capacity reaching 2.2 TW in 2024 [5] and silicon's established role in the electronics industry, demand for silicon-based technologies continues to grow.

Other PV technologies offer complementary advantages and expand the range of usable materials and device architectures for a variety of applications. Thin-film $Cu(In, Ga)Se_2$ (CIGS) solar cells, while representing a smaller share of the market, have achieved a competitive efficiency of 23.6% [23] and demonstrate strong performance in diverse practical applications [24]. CdTe solar cells, with a record efficiency of 23.1% [23], continue to develop as an important thin-film technology, particularly as research progresses toward scalable manufacturing approaches [25]. Perovskite solar cells, which have reached efficiencies of 27%, have attracted considerable attention for their tunable optoelectronic properties and compatibility with various device architectures [26]. Ongoing research aims at further improving their operational stability and fabrication reproducibility. GaAs solar cells, with a record efficiency of 29.1%, remain highly valued in the space industry due to their excellent radiation tolerance [27], and advancements in epitaxial growth methods continue to support progress in this area. Figure 1, showing the best research-cell efficiencies from the National Renewable Energy Laboratory, highlights the collective progress of these diverse PV technologies.

Figure 1: Best Research-Cell Efficiencies chart by the National Renewable Energy Laboratory showcases the progress that has been made in efficiencies of main photovoltaic device technologies throughout the years [23]. The chart is from January 2025, and some values have already increased.

As many leading PV technologies approach their single-junction efficiency limits, future developments are increasingly focused on expanding material choices, reducing environmental impact, and improving manufacturing accessibility. In this context, exploring non-toxic, abundantly available, and easily processed materials can

complement existing silicon-based technologies and contribute to a more diversified and resilient PV landscape. Rather than replacing established technologies, these emerging thin-film materials offer opportunities to address specific application needs and broaden the overall portfolio of sustainable solar energy solutions.

1.2 Low-cost and Earth-abundant solar cell materials

Several alternative solar energy materials have been proposed to complement silicon and broaden the range of technologies available for sustainable photovoltaics. A clear example of sustainable and low-cost photovoltaics includes kesterites with a variable chemical formula of $Cu_2ZnSn(S, Se)_4$. Kesterites are a promising group of materials due to their composition of Earth-abundant elements copper, zinc, tin, and sulfur and/or selenium. The theoretical maximum efficiency of kesterite solar cells is 30% with record cells reaching 16.5% [28] in 2025. Kesterites are primarily used in thin film solar cells, which is advantageous as it reduces material usage.

Emerging inorganic chalcogenide materials have attracted considerable interest for photovoltaics due to their excellent chemical stability, tunable band gap, and high light absorption coefficient [29]. Among them, Sb-based chalcogenides such as Sb_2S_3, Sb_2Se_3, and their solid solutions show particular promise, as they can be deposited by a wide variety of different techniques with efficiencies reaching 10.7% [30].

Organic solar cells (OSCs) have gained considerable interest in recent years because of their tunable absorption spectra, adjustable energy levels, lightweight nature, flexibility, and semi-transparency [31]. The efficiency of OSCs has progressed rapidly, now exceeding 20%. However, the high efficiency achieved in current OSCs relies on the use of highly toxic solvents such as chloroform or chlorobenzene.

Dye-sensitized solar cells (DSSCs) have emerged as promising solar energy technology due to their straightforward design, scalability, cost-effectiveness, and efficiency currently at 13% [32]. Compared to silicon solar cells, DSSCs offer several advantages, including lower costs, minimal environmental impact, and ease of manufacturing, but the use of platinum remains the primary counter-electrode catalyst in DSSCs.

Pyrite FeS_2 has been proposed as a potential PV material, as it may offer pathways toward low-cost energy production. In a comparative analysis [8], 23 candidate materials, including silicon, were assessed based on their annual electricity production potential and production cost (¢ per W). FeS_2 outperformed all other materials, revealing that a 4% efficient FeS_2 solar cell could deliver power at a cost comparable to that of a 19% efficient silicon-based solar cell. Despite very promising material properties, pyrite absorbers have not been very successful in practical devices with a power conversion efficiency below 3% and open circuit voltage <0.3 V [10, 12, 13]. Several theories have been proposed by the research community as the possible reason for the poor performance.

1.3 Chemical and physical properties of pyrite FeS_2

Also known as "fool's gold" because of its gold-like appearance, pyrite rose to materials researchers' attention in the 1970s, with focus increasing in the 1980s following the global oil crisis [13]. Pyrite has a band gap of 0.95 eV and demonstrates a high absorption coefficient ($\alpha > 10^5$ cm^{-1} for hν > 1.3 eV) [9, 10, 33] which suggests that only a 100 nm thin pyrite absorber layer could absorb up to 90% of sunlight. Pyrite exhibits a minority carrier diffusion length of 100-1000 nm, a high electron mobility up to 360 cm^{2}V^{-1}s^{-1} and hole mobility around 11 cm^{2}V^{-1}s^{-1} at room temperature [34]. These characteristics bring pyrite solar cells' theoretical efficiency up to 25% [35].

Pyrite belongs to the group of transition metal sulfides, which also entails iron sulfide forms like pyrrhotite, mackinawite, and troilite. Iron disulfide specifically occurs in two polymorphs: pyrite and marcasite [13, 36]. Due to the multitude of possible Fe-S phases with different chemistries, it is of utmost importance to follow the correct regions of the Fe-S system phase diagram [37], shown in Figure 2, to benefit from the suitable semiconductor properties of the pyrite phase. The pyrite phase exists in the temperature region between 445-617 °C in a stoichiometric ratio of 66.6 atomic% (at%) S and 33.3 at% Fe. Pyrrhotite, which is a non-stoichiometric variant of FeS, starts to form above 617 °C. Marcasite phase begins to dominate below 445 °C.
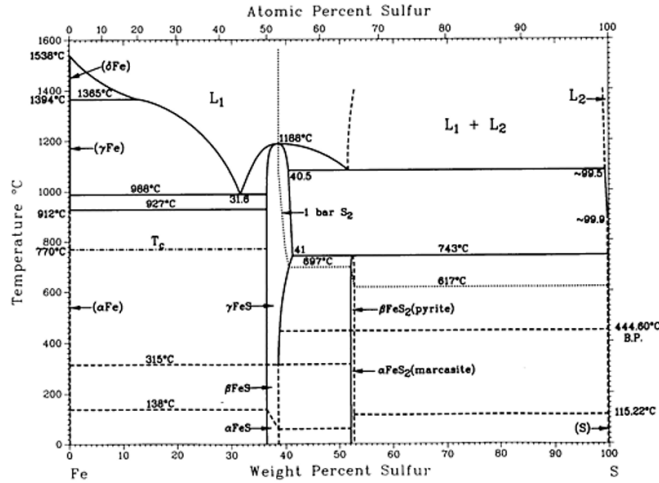

Figure 2: Phase diagram of the iron-sulfur system [37]. Greek symbols correspond to the different space groups. αFeS_2 (marcasite) belongs to the space group of Pnnm and has an orthorhombic structure. βFeS_2 (pyrite) belongs to the Pa$\bar{3}$ space group and has a cubic structure.

Pyrite adopts a simple cubic structure similar to that of sodium chloride (NaCl), where iron atoms take the place of sodium and sulfur dimers replace chloride. In this arrangement, four iron atoms and eight sulfur atoms make up the unit cell, resulting in a 1:2 atomic ratio, with the chemical formula FeS_2. The unit cell contains four FeS_2 formula units. Pyrite's crystal structure is classified within the space group Pa$\bar{3}$ and its lattice parameter measures 5.415 Å under standard conditions [38]. In the cubic structure, low-spin iron atoms at the corners and face centers are coordinated with six sulfur atoms, forming an octahedral coordination. Meanwhile, disulfide groups (S_2^{2-}) are positioned at the center of the unit cell, where sulfur atoms are bonded to three iron atoms and one sulfur atom, forming a fourfold coordination.

The Fe–S and S–S bond lengths are 0.23 nm and 0.21 nm, respectively, while the Fe–Fe distance is 0.382 nm along the (110) face. The bond angles between Fe–S–Fe, S–S–Fe, and S–Fe–S are 115.5°, 94.34°, and between 85.66° and 94.34°, respectively [36]. The crystal structure of pyrite FeS_2 is depicted in Figure 3.

1.4 Electrical transport properties and surface inversion layer

Undoped pyrite is known to exhibit electronic transport behavior that is strongly influenced by intrinsic lattice defects, particularly iron and sulfur vacancies. Among these, sulfur (S) vacancies are typically the most abundant and act as donor defects,
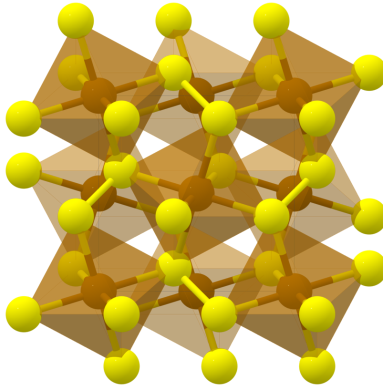
Figure 3: FeS$_2$ pyrite structure. Pyrite belongs to the Pa$\bar{3}$ space group, Fe ion (faded in orange) is bonded to six equivalent S ions (yellow) to form corner-sharing octahedra [39].

causing the natural *n*-type conductivity observed in bulk FeS$_2$. Electronic transport studies have confirmed [14, 40] that sulfur vacancies can reach concentrations on the order of 10^{20} cm^{-3}, forming deep donor levels within the band gap. The ionization of the deep donor states produces a nonuniform charge distribution and an unusually narrow surface space-charge region. This narrow region restricts the achievable barrier height in pyrite and has been linked to the low photovoltage and limited photovoltaic performance reported for pyrite-based solar cells. Furthermore, the high density of deep donor states is believed to inhibit minority-carrier diffusion within the nonconstant space-charge region [40].

In contrast, pyrite also contains surface acceptor states that largely govern the interfacial charge equilibration in single-crystal FeS$_2$ [14, 41]. These acceptor states are associated with iron vacancies, which act as hole generators. Such defects typically originate during the synthesis or growth of pyrite materials. Ultimately, and because of these very characteristic defects, pyrite has been shown to behave as an *n*-type material in the bulk but as a *p*-type material at its surface, leading to significant inversion [13, 14, 41–43]. This phenomenon has also been addressed as the internal *p-n* junction of pyrite. The creation of a *p*-type layer on the surface of pyrite crystals results in band bending and Fermi level pinning in pyrite, also shown in Figure 4, and is believed to be the main reason for the low efficiency and open-circuit voltage in pyrite devices.

Liang et al. used the Hall effect to explain the presence of the reverse surface layer [44]. Their findings suggest that traditional models and mechanisms can not be used to fully understand the electron transitions between the conduction and valence bands of pyrite. It has been suggested that the rich surface states on pyrite originate from the loss of sulfur ligands at the surface, a hypothesis that has been revisited using scanning tunneling spectroscopy [45]. The dangling sulfur bonds seek an electron to neutralize and may borrow it from a nearby Fe^{2+} ion. The dangling bonds oxidize the Fe^{2+} into a Fe^{3+} state, which causes the Fe 3d state to degenerate and split into four energy levels, with levels inside the band gap [46]. These hypotheses were confirmed by Liang et al. [44] by direct transport measurements and numerical modeling. They found that the Fermi level on the surface is close to or even enters the valence band, as shown in Figure 4. Sharp upward
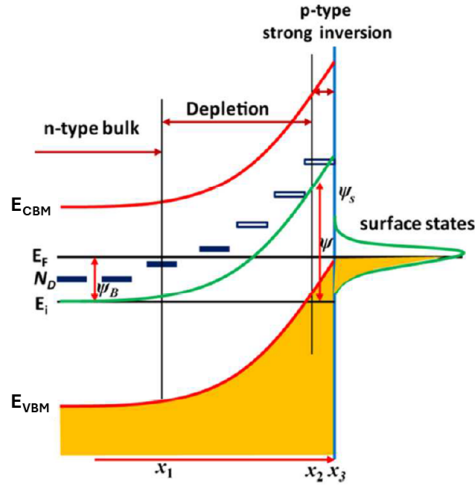
Figure 4: Schematic band diagram of bending energy bands a few nm deep in the pyrite surface [44]. Where ψ stands for the barrier height, N_D stands for the bulk donor concentration, and E_i for its activation energy.

bending of the energy bands, induced by these surface states, leads to the formation of a thin tunneling region, which is thought to be responsible for the observed low V_{OC}. Numerical results showed strong upward band bending of 1.08 eV, effectively pinning the Fermi level below the valence band maximum by about 300 meV.

1.5 Effects of alloying and doping

Introducing impurities or dopants into the crystal lattice of pyrite is an effective strategy for altering or enhancing its properties, particularly for photovoltaic applications. An increasing number of studies have been published on adjusting pyrite's band gap and electronic properties through doping and structural modifications.

Zuniga-Puelles et al. examined the effects of arsenic doping on the properties of pyrite [47]. Arsenic was incorporated up to 0.01 at%, forming $FeAs_xS_{2-x}$, which altered the transport mechanism and turned pyrite from *n*-type to *p*-type. It also reduced the band gap of pyrite from 0.96 eV to approximately 0.2 eV. Doping with silicon dioxide, titanium dioxide, and zirconium dioxide was examined in the same study, but no influence on the electrical transport properties was found. However, it did decrease pyrite's thermal conductivity.

Metals such as osmium, ruthenium, and zinc have been shown by Liu et al. to increase the band gap of pyrite when codoped with oxygen [48]. The study employed density functional theory calculations along with other simulations and found that the band gap of pyrite increased with the incorporation of oxygen atoms by approximately 12.5%. Structures doped with ruthenium and osmium exhibited even higher band gaps when combined with oxygen, while the codoping of zinc and oxygen led to a reduction in the band gap compared to undoped FeS_2.

Zhao et al. investigated doping with oxygen and selenium to enhance the photovoltaic properties of pyrite [49]. They found that replacing sulfur with oxygen in the pyrite crystal lattice resulted in an increased band gap, which they attributed to oxygen's higher

electronegativity and smaller atomic radius. Conversely, the introduction of selenium led to a decrease in the band gap, which was linked to its similar electronegativity to sulfur and larger atomic radius.

The effects of cobalt doping in pyrite have been studied by Shi et al. among others [19, 50, 51]. They found that Co altered the electrical properties of pyrite by converting the material from *p*-type to *n*-type. The most significant changes were observed at a cobalt concentration of 4 at%, beyond which the charge carrier mobility started to reduce from 6.52 to 4.3 $cm^2V^{-1}s^{-1}$ with increasing cobalt concentration. Doping with Co had little impact on the structural and optical band gap. In a separate study, Voigt et al. focused on using metallic CoS_2 contacts to address the internal *p*–*n* junction of pyrite and access the interior properties of the crystals [52]. Co was diffused into pyrite from the contacts and introduced a shallow donor, which resulted in heavy *n*-type doping of the surface. They also introduced Co and S vacancies and defined donor activation energies as low as 5 meV for Co in FeS_2. The work of Voigt et al. [52] improved the understanding of electron mobility in pyrite crystals and identified an additional transport regime in the lattice.

The first unambiguous and controlled *p*-type doping in FeS_2 crystals was demonstrated in 2023 by researchers at the University of Minnesota [21]. According to their study, pyrite was doped with phosphorus (P) during the chemical vapor transport growth. The P levels reached up to 100 ppm, which introduced around 10^{18} holes/cm^3 at 300 K, without affecting the crystal structure or quality. Pyrite crystals, which are naturally *n*-doped due to sulfur vacancies, transitioned to *p*-type as the phosphorus concentration increased to 25 ppm and 55 ppm, as confirmed by Seebeck and Hall effect measurements, respectively. Detailed transport measurements showed that the phosphorus acceptor level is located 175 ± 10 meV above the valence band maximum. These results confirmed that the transition to *p*-type occurs within the bulk material rather than being a result of hopping conduction.

1.6 Pyrite-based photovoltaic devices

Over the past four decades, pyrite has been explored in a variety of photovoltaic device configurations, most commonly as a thin-film absorber exhibiting *p*-type conductivity. Despite intermittent research activity during this period, the power conversion efficiency of practical pyrite-based solar cells has generally remained around ∼3% [10, 12, 16], whether in photoelectrochemical cells with liquid junctions or in solid-state heterojunction devices. To date, no homojunction devices have been demonstrated, even though pyrite can exhibit both *n*- and *p*-type conductivity [9, 53, 54]. This absence is primarily due to the persistent challenges and uncertainty surrounding the control and understanding of doping mechanisms in FeS_2 [21]. Some of the most significant results from recent years include the work of Prabukanthan [55] and Law [42, 56, 57].

Prabukanthan and colleagues have reported the highest known efficiency of pyrite-based photovoltaic devices [55]. They successfully deposited cobalt-doped pyrite thin films using electrochemical deposition and evaluated their performance in a solar cell with the ITO/FeS_2/ZnSe/Au configuration. Their findings indicated enhanced photoresponse and improved stability when 3 mol% Co^{2+} was introduced, achieving a power conversion efficiency of up to 5.42%. The improved performance was attributed to the partial substitution of Fe^{2+} by Co^{2+}, which reduced the material's band gap and promoted more efficient charge separation at the ZnSe interface. They also conducted a comparative analysis with undoped pyrite in a similar device structure, which exhibited lower values for power conversion efficiency (PCE) and open-circuit voltage. Although Prabukanthan et al. reported an efficiency exceeding 5% for their pyrite-based solar cell,

the research community continues to recognize Ennaoui's original result of 2.8% [12] as the benchmark for the highest reliably achieved efficiency.

The research group led by Matt Law at the University of California, Irvine, has dedicated over ten years to the investigation of pyrite films and crystals as a photovoltaic absorber, including studying the surface defect chemistry [15, 42] and several surface passivation techniques, different junction partners to pyrite (ZnS, NiO, CdS, ZnO) [57], and alloying with oxygen to increase the band gap of pyrite [58]. These substantial contributions in understanding the optoelectronic properties of pyrite concluded with the fabrication of pyrite-based diodes [56], incorporating a layered structure of glass/Mo/MoS$_2$/pyrite/ZnS/i-ZnO/contact. The heterostructures exhibited open-circuit voltages exceeding 400 mV, with peak values reaching up to 610 mV under $\sim$ 1 sun illumination at room temperature (RT). The highest V$_{OC}$ values were achieved using pyrite films synthesized through the solution-phase elemental ink method. Despite the promising photovoltages, the devices demonstrated low short-circuit current (J$_{SC}$) densities of approximately 10 μA, causing the efficiencies to range from 0.0002% to 0.0014% for the devices. The underlying cause of the high V$_{OC}$ and low J$_{SC}$ was not fully understood, but the electronic band offset between FeS$_2$ and ZnS was suggested as a possible reason.

Table 1: Summary of research on pyrite-based solar cells since the 1990s, highlighting the highest reported power conversion efficiencies and corresponding device architectures.

Method	PCE	Ref.
FeS$_2$/I:I$_3$ PEC cell	2.8%	Ennaoui, 1993 [12]
TiO$_2$/FeS$_2$ nanocrystals/PEDOT	3%	Lingli Luo, 2015 [59]
P3HT/FeS$_2$ nanocrystals/PEDOT	0.16%	Lin, 2009 [60]
FeS$_2$/ZnS	0.0014%	Law, 2015 [57]
Co^{2+} doped FeS$_2$/ZnSe	5.42%	Prabukanthan, 2017 [55]
FeS$_2$/ZnSe	1.98%	Prabukanthan, 2017 [55]
FeS$_2$ nanocrystals/CdS	1.1%	Kirkeminde, 2012 [61]
P3HT:PCBM:FeS$_2$ quantum dots	3.62%	Alam Khan, 2014 [62]
PEDOT:PSS/MEH-PPV polymer:FeS$_2$	0.064%	Middya, 2014 [63]
P3HT:PCBM:FeS$_2$ nanocrystals	2.79%	Richardson, 2013 [64]

Table 1 provides an overview of the research on pyrite-based solar cells reported in the literature. The data presented focus specifically on the efficiencies and device architectures of solid-state FeS$_2$ photovoltaic junctions, as these are most relevant to the scope of this thesis. As a notable exception, the photoelectrochemical cell results from Ennaoui et al. [12] are included, as their work represents the first documented demonstration of pyrite functioning as a photovoltaic material with measurable efficiency. This study [12] is widely regarded in pyrite-related literature and serves as a reference point for much of the subsequent research in the field.

1.7 Monograin powder technology

As outlined in the previous chapter, experimental pyrite-based solar cells have predominantly been explored in thin film and nanocrystal configurations [55, 59–61, 64]. The properties of films are strongly influenced by pyrite's surface properties, which can pose significant challenges during fabrication and device integration [42, 44]. As an alternative, employing discrete pyrite crystals in photovoltaic applications may offer

distinct advantages. The monograin layer solar cell concept combines the benefits of thin, membrane-like solar cells, such as reduced material consumption, with the use of semiconductor microcrystals as the absorber layer, rather than a continuous thin film [65–68]. The monograin layer (MGL) technology decouples the fabrication of the absorber material from the assembly of the solar cell module and allows the development of flexible, lightweight, and cost-effective solar panels. The production of MGL solar cells is relatively straightforward and does not rely on high-vacuum environments, high-power inputs, or extensive specialized equipment - requirements often associated with traditional thin film technologies. The MGL technology has not been previously applied to fabricate pyrite-based solar cells.

The MGL solar cell structure is schematically shown in Figure 5. It adopts a superstrate configuration, consisting of the following layer sequence: back contact / absorber / buffer / transparent conductive oxide (TCO) [65–68]. This layered structure is adhered to a supportive substrate, typically glass or a polymer film. The absorber is composed of a single layer of nearly monodisperse semiconductor powder crystals, embedded in a polymer matrix, usually an epoxy, whose thickness is less than the diameter of the crystals. Each crystal surface is uniformly coated with a thin buffer layer, typically applied through solution-based deposition, to facilitate the formation of a *p/n* junction. Following buffer layer deposition and subsequent mild thermal treatment, each coated crystal effectively functions as an individual photovoltaic microcell. All microcell crystals are connected in parallel.
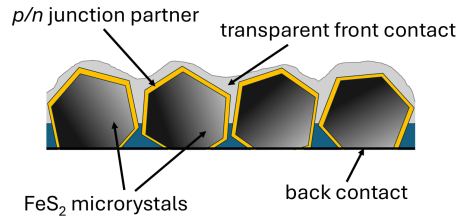

Figure 5: Schematic drawing of the monograin layer solar cell structure. Pyrite microcrystals serve as the absorber layer.

In this thesis, pyrite absorber crystals are synthesized using the monograin powder technology [65–68]. This process requires suitable precursor materials, which are consumed during the formation of the semiconductor compound, as well as a flux salt that serves as a medium for crystal growth. The precursors for pyrite synthesis are weighed in stoichiometric ratios (one mole of iron for two moles of sulfur) and placed in quartz ampoules. A flux salt is added so that the volume of the molten phase would approximately match the volume of the solid precursors. The ampoules are then degassed and hermetically sealed. These sealed ampoules are subsequently heated in a furnace to elevated temperatures, where the flux becomes molten while the forming semiconductor crystals remain in the solid phase. During synthesis, both the precursors (along with any residual impurities) and the synthesized crystals dissolve in the molten flux, up to their solubility limit at the given synthesis temperature. Once the primary reaction is complete, crystal growth proceeds via recrystallization through the Ostwald ripening mechanism [69], wherein larger crystals grow at the expense of smaller dissolved particles. The growth rate is governed by the solubility of both the precursors and the product crystals in the flux; higher solubility enhances mass transport, leading to faster

and larger crystal formation [68]. Depending on the required semiconductor and the used flux, the synthesis of microcrystals with sizes ranging from 30 to 200 μm requires approximately 5 to 14 days [65, 70, 71]. The size of the resulting crystals follows the Gaussian size distribution.

1.7.1 Flux Materials

Flux materials are employed in monograin powder technology to synthesize semiconductor microcrystals with the morphology and physical properties required for the fabrication of monograin layer solar cells. Ideally, these microcrystals, referred to as monograins, should be monocrystalline, exhibit smooth surfaces and uniform shapes, and fall within the size range of 50 to 150 μm. The most effective method for producing such monograins is the molten salt synthesis-growth method. In this method, the salt or flux forms a liquid phase at the synthesis temperature, enabling the dissolution of precursors and small semiconductor seed crystals. Flux salt is added to the synthesis ampoules in quantities that ensure the volume of the resulting liquid phase is approximately equal to that of the solid microcrystals [72, 73]. This specific volume ratio promotes the independent growth of semiconductor, or FeS_2 particles, during synthesis, as repulsive capillary forces act to separate and space them apart. Following the crystal growth process, the flux is removed, leaving behind the synthesized microcrystals.

Several important criteria must be considered when selecting the flux material:

- The melting point of the flux must be lower than that of the semiconductor.

- The flux must not react with the precursor materials or with the semiconductor.

- The flux should be readily removable after the synthesis-growth process, preferably through dissolution in water.

- The precursors should be soluble in the liquid phase of the flux material.

- The vapor pressure of the flux should be low at the process temperatures.

- The flux material should be affordable and environmentally sustainable.

The research group led by M. Law has conducted extensive studies on the synthesis of pyrite crystals using flux materials [42, 74]. In their work, sodium polysulfide (Na_2Sx) was employed as the flux, selected for its low melting point across a broad range of compositions and temperatures [75]. The Na-S system exhibits eutectic points as low as 240 °C and features a wide region of binary liquid immiscibility above 253 °C [75]. Na_2S_x also shares a common anion with pyrite and contains a cation that does not significantly incorporate into the growing crystal structure [42]. Salk et al. [74] synthesized pyrite single crystals isothermally in quartz ampoules at 780 °C for six hours using Na_2S_x as the flux. After synthesis, the flux was removed by dissolution in water. This method yielded pyrite single crystals several millimeters in diameter. A similar synthesis regime was utilized by Uchiyama [76], who heated the pyrite precursors and Na polysulfides at 810 and 600 °C for 6 h and 10 days, respectively, and obtained FeS_2 crystals with a diameter of about 7 mm.

Zavrazhnov et al. [77] synthesized pyrite in the liquid phase of iron(II) halides (FeX_2, where X = Cl, Br, I) under a controlled sulfur vapor pressure. They also employed the eutectic melts of $KCl-FeCl_2$ and $NaCl–KCl–FeCl_2$ as solvents. The experimental setup consisted of a two-zone furnace and a sealed ampoule containing iron sulfides and halides at one end, and elemental sulfur at the other. The authors observed that in this closed,

non-isothermal system, iron halide melts reacted with sulfur vapors. At low pressures (< 0.4 atm), pyrrhotite was formed, whereas higher pressures favored the growth of FeS_2 crystals. Notably, in the cases of $FeBr_2$ and FeI_2 melts, pyrite formed even without the addition of iron sulfide precursors, due to the direct reaction of the iron halide liquid phase with sulfur vapor.

Our laboratory has primarily employed alkali iodide salts for the synthesis of semiconductor microcrystals, with substantial experience in the growth of kesterite and CIGS materials using this approach [65, 68, 72, 78, 79]. The monograin powder technology has not yet been employed for pyrite. Considering the favorable properties of alkali iodide salts, particularly their alignment with the selection criteria described above, it is the logical starting point for an investigation. At the same time, it is important to consider that, during the molten salt synthesis-growth process, constituent elements of the flux may diffuse into and become incorporated within the semiconductor crystals being synthesized [68, 79]. While iodide has a relatively large ionic radius [80], it is less likely to substitute into the pyrite crystal lattice; however, alkali metal cations present in the flux may act as unintentional dopants. This potential for alkali incorporation must be taken into account when evaluating the purity and electronic properties of pyrite crystals grown via this method.

1.8 Pyrite-based solar cells for lunar applications

In recent years, pyrite has garnered growing attention for its potential use in space applications, particularly in the context of renewable energy generation for the future lunar habitat. This interest was spurred by announcements from the European Space Agency (ESA) and NASA [11, 81] regarding renewed efforts to return to the Moon, with the long-term goal of establishing a permanent outpost. The conceptual layout of a future lunar habitat is drawn by the European Space Agency in Figure 6a. As plans progress toward sustained human presence on the lunar surface, ensuring a reliable and autonomous energy supply becomes essential. Solar energy remains one of the few viable options for *in situ* power generation. While transporting solar panels from Earth is technically feasible, given the recent decline in launch costs, this approach remains environmentally burdensome and logistically complex. Instead, there is a strong incentive to enhance the sustainability of lunar infrastructure by minimizing dependence on Earth-based resources. This has led to the proposal of utilizing locally available materials, such as those found in the lunar regolith, to manufacture photovoltaic devices on-site. The development of such technologies, including pyrite photovoltaics for lunar applications, has emerged as a crucial avenue of research.

Assessing the elemental and mineralogical composition of the lunar regolith is essential for planning to utilize lunar resources. Apollo mission samples remain the primary reference, revealing significant amounts of silicon (mainly in oxide form), along with iron, aluminum, calcium, magnesium, and titanium [85–87]. While silicon is abundant and widely used in both terrestrial and space-based photovoltaics, its application on the Moon poses challenges, including the need for high-temperature processing around 1450 °C, high sensitivity to defects, and the necessity for extreme purity [88, 89]. The vast amount of energy that goes into processing silicon wafers increases the time for economic return for solar panels. That is critical in the extreme energy scarcity conditions during the first stages of the lunar base. GaAs, which is another widely used PV material in space applications, would be extremely challenging to source and produce from materials available on the lunar surface. In contrast, pyrite presents a compelling opportunity, with the potential to enable low-cost energy production, if
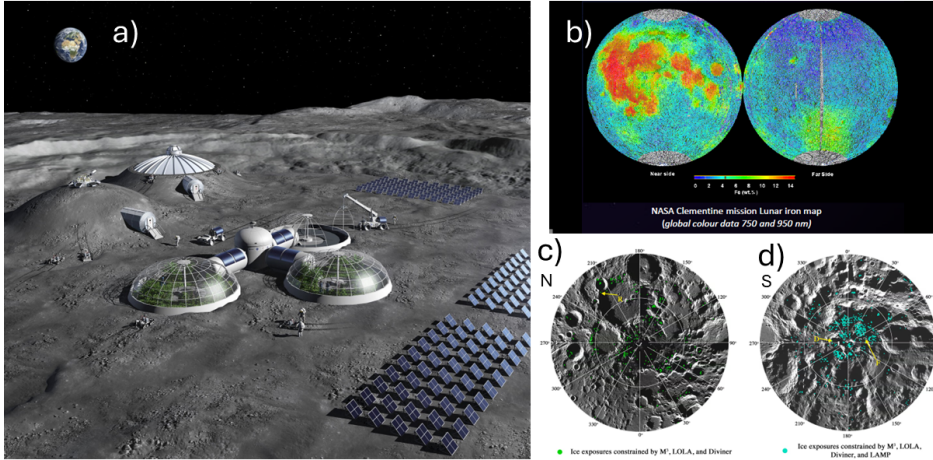
Figure 6: a)Artist impression of a lunar habitat concept [82]. b) Lunar iron map, based on the data retrieved from the NASA Clementine mission [83]. c,d) Map of the lunar water ice [84]. The lunar South Pole region, Fig. 6d, holds a significant amount of water ice and has been chosen as one of the best candidates for a future habitat location.

greater research focus were directed toward overcoming the remaining material and device challenges.

Pyrite has a high light absorption coefficient FeS_2 $\alpha > 10^5$ cm^{-1} [9], compared with Si $\alpha > 10^3$ cm^{-1} [90]. That means, a 100 μm thick layer of Si will absorb the same amount of light as only a 1 μm thick layer of FeS_2. Pyrite can also be synthesized or treated at a lower temperature, starting from 440 °C [37], making it a sustainable choice for extraterrestrial energy production and on-site missions.

The constituent elements of pyrite can be sourced on the Moon. Iron is abundantly present in the lunar regolith, predominantly in the form of silicate and oxide phases. The overall iron content of the lunar crust is well-known thanks to the thorough data set of the NASA Clementine mission, launched in 1994 [83, 91]. The Clementine data have recently been complemented with data from the Chang'e-5 mission, run by China in 2020 [92]. Lunar highland crusts contain approximately 3 weight% of Fe, while the lower regions contain 7-8 weight% of Fe. The majority of the lunar iron is found in oxide minerals. The average abundance of FeO is 8.94 weight% [92]. Troilite (FeS) is the most common sulfide mineral on the lunar surface and makes up around 0.05-0.2 vol.% of the mare basalts and highland crust, as observed from the Apollo mission samples [93]. It serves as a promising precursor for the synthesis of pyrite, for which an additional sulfur source must be added. Sulfide minerals identified in lunar rocks also include mackinawite $(Fe,Ni)_{1+x}S$, sphalerite $(Zn, Fe)S$, chalcopyrite $CuFeS_2$, and cubanite $CuFe_2S_3$ [94]. These sulfide phases are often associated with magmatic Fe–Ti oxides [95], a relationship analogous to that observed in terrestrial samples, particularly when lunar mare basalts are compared to their Earth-based counterparts. The average lunar highland geology contains up to 0.1 wt% of sulfur, and typical lunar mare soils up to 0.2 at% S [96, 97]. Although not richly concentrated on the Moon, sulfur is present in association with other useful elements, making the mining of lunar sulfur worth serious consideration [97].

The development of pyrite-based solar cell technology may become particularly relevant when human exploration expands to other celestial bodies. Mars, for example, has a higher abundance of iron-bearing minerals compared to the Moon and even the

Earth [98]. This may support the production of FeS$_2$-based solar cells in the future.

However, theoretical properties are of limited value without clear technological pathways for producing efficient FeS$_2$-based solar cells. Advancing pyrite-based technology with significantly higher power conversion efficiencies is essential for sustainable green energy production on Earth and beyond.

1.9 Summary of literature review and aim of the study

Photovoltaics represent one of the most promising pathways toward achieving environmental sustainability in the energy sector. Currently, most solar panels are made using silicon - a material that demands significant energy for extraction and purification, and whose cost has risen due to growing demand from the electronics industry. As a result, considerable research efforts have been directed toward the development of Earth-abundant, low-cost, and non-toxic solar energy materials, such as kesterites, CIGS, organic photovoltaics, and other emerging solar energy materials.

Pyrite (FeS$_2$) has been identified as the most cost-effective material ever proposed for photovoltaic applications [8], attracting attention both on Earth and for space applications. Composed of abundant, non-toxic, and inexpensive elements, pyrite attracted significant research interest in the 1980s, when Ennaoui et al. [99, 100] demonstrated its application in a photoelectrochemical cell, achieving a power conversion efficiency of 2.8% [12]. Despite intermittent research over several decades, the efficiency of pyrite-based solar cells has not surpassed 5.4% [55], with many contemporary studies still citing the 1993 result as the benchmark [13, 21, 35]. This discrepancy between the low experimental efficiencies and pyrite's high theoretical efficiency of 25% is primarily attributed to limited understanding of its doping mechanisms and the so-called surface inversion effect.

As a result of the surface inversion, pyrite crystals exhibit *n*-type conductivity, while thin films are commonly reported as *p*-type [9, 42, 43, 45]. This inhomogeneity is largely due to the dominance of surface states in thin-film pyrite, where surface properties significantly outweigh bulk characteristics. These surface states lead to the formation of an "inverse" surface layer that dictates the electrical behavior. The low V$_{OC}$ and limited efficiency observed in pyrite solar cells are often attributed to strong upward band bending at the surface, which creates a thin tunneling barrier that impedes efficient charge separation.

The majority of photovoltaics research on pyrite has focused on thin films and nanocrystals, while bulk pyrite crystals remain largely underexplored. One possible reason is the limited number of photovoltaic technologies that utilize individual crystals as the absorber. The monograin layer solar cell technology presents a potential solution; it employs an absorber of individual microcrystals and is a simple and cost-efficient method of fabricating solar cells [65, 73]. To date, monograin powder technology has not been applied to pyrite. This approach involves using a molten salt flux as the synthesis medium for semiconductor microcrystals. Elements from the flux can incorporate into the growing crystals, leading to unintentional doping and influencing their optoelectronic properties [68]. To date, alkali metals have not been employed as dopants in pyrite. Therefore, synthesizing pyrite in various alkali metal salt fluxes serves a dual purpose: it provides insight into the behavior of FeS$_2$ formation in a molten salt flux environment and enables the investigation of the effects of alkali metal incorporation on the structural and electronic properties of pyrite.

Another potential strategy to improve the properties of pyrite is to decrease the detrimental effects of the surface inversion layer by achieving uniformly *p*-type

23

conductivity throughout the entire crystal. This could lead to more consistent and predictable electrical behavior across the material. To date, only one study has reported successful p-type doping of bulk pyrite crystals, but the community lacks a mechanistic understanding of the doping route and a scalable doping strategy for p-type FeS_2 crystals.

The aim of this thesis is to apply the monograin powder technology and find the optimal synthesis conditions to develop pyrite (FeS_2) microcrystals that could be used in the absorber of a monograin layer solar cell. The thesis seeks to deepen the understanding of the optoelectrical effects introduced by different dopants in pyrite and to develop a method for controlling the conductivity type of pyrite microcrystals. To reach the aim, the specific objectives of the thesis are:

- Find the optimal synthesis-growth conditions for single-phase pyrite FeS_2 microcrystals by using the molten salt synthesis-growth method and comparing two different flux environments - potassium iodide and elemental sulfur.

- Study the effects of alkali metal impurities in pyrite by synthesizing FeS_2 microcrystals in the liquid phase of KI, LiI, CsI, and Na_2S_x, with the aim to increase understanding of the structural, morphological, and optoelectronic properties of the dopants.

- Develop a doping strategy to obtain p-type pyrite crystals by introducing red phosphorus into pyrite by three different established semiconductor doping techniques. Illustrate the incorporation mechanism of phosphorus within the pyrite lattice.

2 Experimental

Divided into four parts, this chapter describes the main experimental procedures and methods. The first three subsections describe the synthesis conditions of FeS_2 microcrystals, the effects of different growth environments, and the doping routes with phosphorus. The fourth subsection summarizes the characterization methods used in this study.

2.1 Preparation of FeS_2 microcrystals

The FeS_2 pyrite materials studied in this thesis were synthesized by the monograin powder technology in the liquid phase of a flux material. Commercially available FeS (99.9%, Thermo Fischer) and elemental S (99.999%, Alfa Aesar) were used to synthesize pyrite. Elemental S was also used in some experiments as the molten flux medium. Sulfur was chosen as a flux because it shares an anion with FeS_2 and does not add any unwanted impurities from the constituent elements into the pyrite crystals. In a parallel experiment, FeS_2 was synthesized in the KI (99.95%, Acros Organics) flux. The different fluxes were considered in Paper I. The precursors FeS and S were added into quartz ampoules in the amounts necessary to receive stoichiometric pyrite. S or KI were added in the amounts that the volume of the melt will be equal to the volume of the solid microcrystals at the synthesis temperature. The ampoules were degassed under a dynamic vacuum, sealed in a propane-oxigen flame, and placed into the furnace for the synthesis-growth process. The ampoules with the sulfur flux and precursor mixtures were heated at 500, 550, and 600 °C for 7 days and then cooled by quenching the ampoules in water. The ampoules with the KI flux and precursor mixtures were heated at 740 °C for 7 days, then the temperature was lowered to 575 °C, kept there for 24 h, and cooled by quenching water. Higher temperature was chosen for the ampoules with the KI flux because the melting point of KI is at 681 °C [101] and its vapor pressure is not a concern at high temperatures, as opposed to sulfur. The temperature was lowered to 575 °C to bring the ampoules into the pyrite phase region of the Fe-S system, according to the phase diagram [37].

Some of the FeS_2 material obtained from the synthesis in sulfur was recrystallized in KI to receive a more suitable morphology and composition. The recrystallization steps are considered in Paper II. For the recrystallization, the obtained FeS_2 mixture was placed into an ampoule, and a KI flux was added. The ampoule was heated at 740 °C for 7 days and cooled as described in the paragraph above. The details of finding the correct synthesis regime are summarized in Table 2.

The sulfur flux was partially removed by vacuum sublimation, followed by etching with a 10% KCN solution to release the pyrite crystals from the used flux. The KI flux was removed by leaching with deionized water in an ultrasonic bath. All the materials were dried in a thermostat at 50 °C. For the fabrication of monograin membranes, the obtained crystals were sieved into narrow granulometric fractions between 38-125 μm.

2.2 Comparison of different growth environments

Once the optimal synthesis conditions had been established, the next step was to investigate the impact of different fluxes and the potential impurities introduced by them. The comparison of the effects of different fluxes is described in Paper III. KI, LiI, CsI, and Na_2S_x were selected, as the influence of alkali metal impurities on pyrite had not been thoroughly studied. In contrast, alkali metal dopants in other semiconductors, particularly chalcogenide materials such as CIGS and CdTe, have been shown to enhance efficiency and passivate defects. Na_2S_x had previously been employed as a flux for growing pyrite

Table 2: Synthesis conditions of FeS$_2$ microcrystals.

Precursors	Flux, synthesis	Flux, recrystallization	Temperature regime, synthesis	Temperature regime, recrystallization
FeS and S	S	-	RT -> 500 °C, rapid cooling	-
FeS and S	S	-	RT -> 550 °C, rapid cooling	-
FeS and S	S	-	RT -> 600 °C, rapid cooling	-
FeS and S	S	KI	/as above/	RT -> 740 -> 575 °C, rapid cooling
FeS and S	KI	-	RT -> 740 -> 575 °C, rapid cooling	-

crystals, making it a good reference material. The iodides were chosen due to their solubility in water and the expectation that iodine, owing to its large ionic radius [80], would be unlikely to incorporate into the pyrite lattice. A further objective was to determine whether the solubility of pyrite precursors was higher in LiI, CsI, or Na$_2$S$_x$ compared to KI, as increasing precursor solubility could enable the growth of crystals with a larger average diameter.

The pyrite materials were synthesized in different fluxes, similarly to the method described above. The precursors, FeS and S, were placed in quartz ampoules in stoichiometric amounts. The flux materials KI, LiI (99%, Acros Organics), CsI (99.999%, Alfa Aesar), and Na$_2$S$_x$ (99.5% AnalaR Normapur) were added into their respective ampoules, considering that they would yield equal volumes of solid and liquid phases at the synthesis temperature. By default, all syntheses in this thesis use the 99.9% purity FeS precursor, acquired from Thermo Scientific. One synthesis was carried out in this series, using a precursor with a higher purity - FeS 99.99% purity, acquired from Apollo Scientific. This synthesis was carried out in the KI flux. A summary of the heating regimes and used materials is brought in Table 3. A parallel synthesis was carried out without any flux. Later, some FeS$_2$ material that had been synthesized in the KI flux was recrystallized with four times and ten times the flux amounts V$_{flux}$ = 4 x V$_{pyrite}$ and V$_{flux}$ = 10 x V$_{pyrite}$.

Table 3: Synthesis conditions of FeS$_2$ crystals grown in different environments and flux conditions.

Starting material	Flux	Synthesis temp. °C
FeS and S	KI	690
FeS and S	LiI	690
FeS and S	CsI	690
FeS and S	Na$_2$S$_x$	475
FeS and S	-	500
4N FeS and S	KI	690
FeS$_2$ prepared in KI	Recrystallized in KI, 4x volume	Recrystallized at 690
FeS$_2$ prepared in KI	Recrystallized in KI, 10x volume	Recrystallized at 690

2.3 Doping pyrite with phosphorus

Paper IV focuses on the *p*-type doping of the FeS_2 microcrystals. Three doping strategies, widely used in semiconductor processing, were employed to investigate the incorporation of red phosphorus into FeS_2. Technical-grade red phosphorus (99.5%, Reahim) was used in all experiments. In the first series, phosphorus was introduced via the vapor phase. FeS_2 microcrystals, previously synthesized in the KI flux medium, were placed on one side of a two-chamber ampoule, while elemental phosphorus was placed in the opposite chamber. The chambers were connected by a narrow neck, allowing phosphorus vapor to diffuse toward the FeS_2 during thermal treatment. The ampoules were sealed and heated at 500 °C for 48 hours. The schematic diagram of the heat treatment is visualized in Figure 7.1. After cooling, the treated FeS_2 material was collected for analysis.
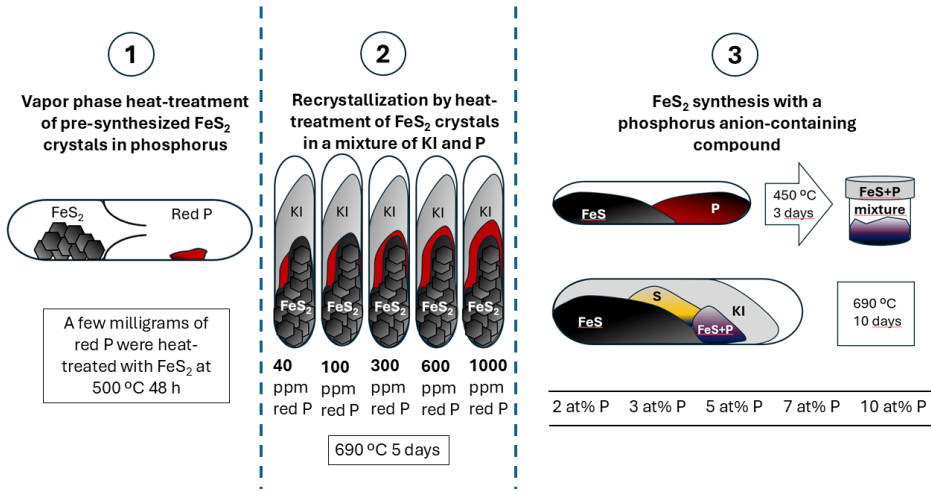

Figure 7: Schematic representation of the three applied doping treatments: (1) in the vapor phase, (2) during recrystallization, and (3) during synthesis of pyrite crystals.

In the second series, phosphorus was introduced via the liquid phase during the recrystallization of FeS_2 microcrystals. Red phosphorus was mixed with potassium iodide, and this mixture was added to the recrystallization ampoules containing previously synthesized pyrite crystals. The amounts of the mixture were calculated to achieve target phosphorus concentrations of 40, 100, 300, 600, and 1000 ppm in FeS_2 on a molar basis, corresponding to 0.004, 0.01, 0.03, 0.06, and 0.1 at%. The sealed ampoules were heated at 690 °C for 5 days and removed from the furnace to cool naturally to room temperature. The visualization of the recrystallization treatment is shown in Figure 7.2.

In the third series, pyrite was synthesized directly from precursors in the presence of phosphorus. The phosphorus precursor was prepared by mixing equimolar amounts of FeS and red P, followed by heating the mixture in a sealed ampoule at 450 °C for 3 days. This FeS+P mixture was then added into the pyrite synthesis ampoules to achieve target phosphorus concentrations of 2, 3, 5, 7, and 10 at% relative to sulfur in the final FeS_2 crystals. The ampoules were heated at 690 °C for 10 days and allowed to cool naturally to room temperature. The third doping approach is visualized in Figure 7.3.

2.4 Characterization methods

The characterization methods used in this study are summarized in Table 4. More detailed descriptions of the chosen characterization tools are provided in papers I-IV.

Table 4: Characterization methods used in this thesis.

Properties	Characterization tool	Apparatus	Paper
Morphology	Scanning Electron Microscopy	(HR-SEM) Merlin, Zeiss ULTRA 55	[I-IV]
Phase composition	Raman Spectroscopy	Horiba's LabRam HR800 spectrometer	[I-IV]
	X-Ray Diffraction	Rigaku Ultima IV diffractometer	[I-IV]
Elemental composition	Energy Dispersive X-Ray Spectroscopy	Zeiss ULTRA 55 Bruker Esprit 1.8 system	[I-IV]
	X-ray photoelectron spectroscopy	Kratos Analytical Axis Ultra DLD spectrometer	[I]
	Time-of-flight secondary ion mass spectrometry	IONTOF 5 LMIG 25 keV	[III]
	Inductively coupled plasma mass spectrometry	Agilent 8800 ICPMS/MS	[III][IV]
Conductivity type	Hot probe method	Soldering iron, contacts, cables, multimeter	[I][II][IV]
Electronic band structure	Ultraviolet photoelectron spectroscopy	Axis Ultra DLD photoelectron spectrometer by Kratos Analytical	[III]
Recombination processes	Photoluminescence spectroscopy	532 nm laser, Horiba Jobin Yvon FHR640 single grating monochromator and Hamamatsu InGaAs photomultiplier tube detector	[III]
P-n junction formation	Current-voltage measurements	Keithley 2400 source meter	[I][II]
Charge carriers' density	Capacitance-voltage measurements	Wayne Kerr 6500B impedance analyser	[I][II]

3 Results

This chapter presents the results and discussion of synthesizing pyrite microcrystals for photovoltaic applications. Initially, optimal synthesis conditions are identified for obtaining single-phase pyrite microcrystals with suitable morphology for use in the absorber of monograin layer solar cells. Particular attention is given to the characterization of the microcrystals' outermost surface. The developed synthesis method is further employed to investigate the effects of alkali metal impurities (Li, Na, K, Cs) on pyrite. This understanding of impurity effects and doping methods is then applied to develop a synthesis technique for phosphorus-doped FeS_2 microcrystals, enabling p-type doping of pyrite.

3.1 Structural and elemental composition of FeS_2 synthesized in S flux

FeS_2 crystals synthesized using elemental sulfur as a flux were found by the energy dispersive X-ray spectroscopy (EDX) and Raman analyses to be sulfur-deficient, primarily due to challenges in removing excess sulfur post-synthesis. Since sulfur is insoluble in water, removal was achieved via vacuum sublimation under mild heating (<100 °C), followed by leaching in a 10% KCN solution. The results of the phase analysis by Raman spectroscopy are shown in Figure 8. Raman spectroscopy after sublimation revealed strong signals corresponding to elemental sulfur, indicating incomplete flux removal. Subsequent KCN treatment significantly enhanced the pyrite signals while reducing those of sulfur-deficient pyrrhotite ($Fe_{x-1}S$), hematite (Fe_3O_4), and residual elemental sulfur (paper I).
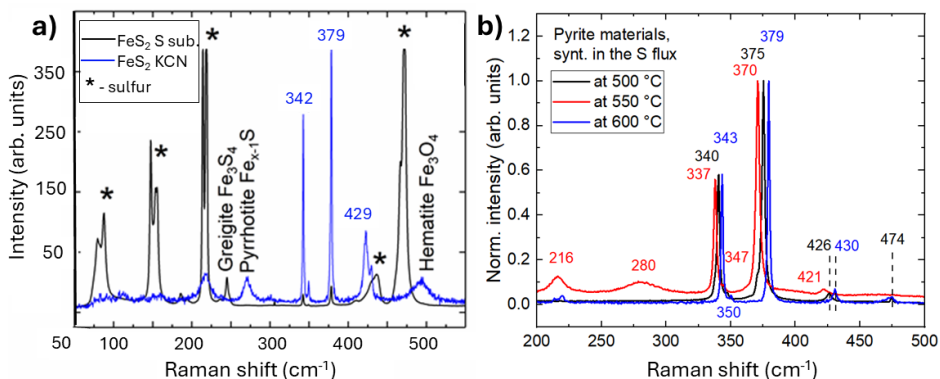

Figure 8: *Raman spectra of the FeS_2 materials synthesized in the sulfur flux at different temperatures. a) black line: sulfur flux has been removed by sublimation under vacuum. Blue line: Material has been etched with a KCN solution after sublimation. b) Comparison of pyrite materials synthesized at different temperatures in S flux. The flux has been removed by sublimation and etching for all samples.*

Figure 9 presents the XRD analysis results of the KCN-etched samples and reveals the presence of multiple phases - pyrrhotite, marcasite (isomer of FeS_2), hematite, and elemental sulfur - alongside pyrite. These results suggest that the sulfur removal steps may have partially depleted sulfur from the surface of the FeS_2 matrix itself (paper I).

A particularly notable observation emerged when comparing FeS_2 samples synthesized at 500, 550, and 600 °C, Figure 8. All were subjected to identical sulfur removal procedures. Raman peak positions, which typically appear at 343, 379, and
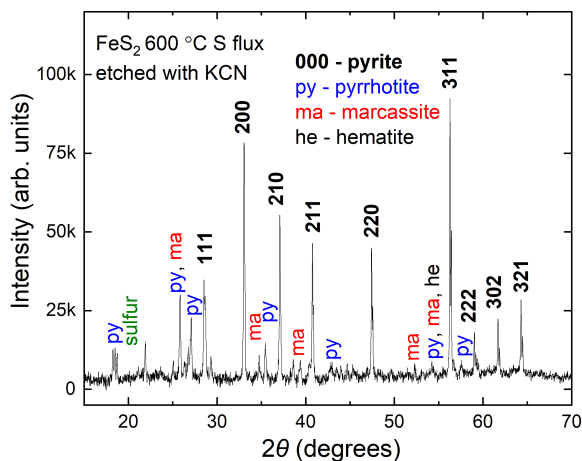
Figure 9: X-ray diffraction data of the FeS$_2$ materials synthesized in the sulfur flux at 600 °C. The flux was removed by sublimation and etching in KCN.

430 cm^{-1} for stoichiometric pyrite [102–105], shifted by up to 9 cm^{-1} to lower values in the lower-temperature samples. This is an established indicator of sulfur deficiency in chalcogenide systems [106] and indicates the increase of the Fe-S bond length due to the stress-strain effect caused by the lower S concentration (paper I).

The morphology of the materials synthesized in S flux is illustrated in Figure 10. The microcrystals synthesized at 500 and 550 °C are not yet formed as monograins; instead, they consist of smaller sintered particles with an average diameter of 500 nm. The shape of the crystallites is not uniform, and the crystal surfaces appear rough. The materials synthesized at 600 °C have developed larger crystallites with an average size of 1 μm but the crystallites are sticking together due to sintering and are also not suitable for further application. All the images compared in Figure 10 depict materials where the S flux had been removed by vacuum sublimation and KCN etching.
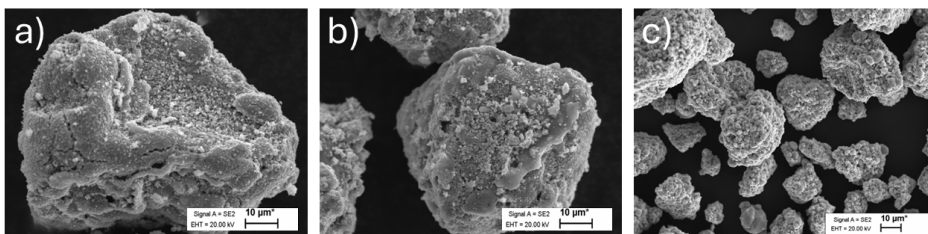

Figure 10: SEM images of the FeS$_2$ crystals synthesized in the sulfur flux at a) 500 °C, b) 550 °C, c) 600 °C.

Elemental composition of the materials was characterized by EDX and is shown in Table 5. The analysis revealed that the lowest FeS$_2$ synthesis temperature (500 °C) yielded the most sulfur-poor composition with 39.2 at% iron and 60.8 at% sulfur. Higher synthesis temperatures (550 and 600 °C) resulted in a near-stoichiometric FeS$_2$ composition of 33.1

Table 5: Elemental composition of the materials synthesized in liquid sulfur and in potassium iodide, analyzed by EDX.

Sample	Fe (at%)	S (at%)
500 °C, S flux	39.2 at%	60.8 at%
550 °C, S flux	33.1 at%	66.9 at%
600 °C, S flux	33.4 at%	66.6 at%
740 °C, KI flux	33.7 at%	66.3 at%

at% Fe and 66.9 at% S for material synthesized at 550 °C and 33.4 at% Fe and 66.6 at% S for materials synthesized at 600 °C.

3.2 Structural and elemental composition of FeS_2 recrystallized or synthesized in KI flux

FeS_2 materials synthesized in S flux at 600 °C were recrystallized in KI flux at 740 °C. The phase analysis by Raman spectroscopy and XRD, as shown in Figure 11, indicates that high-temperature recrystallization promotes the transformation of secondary sulfur-deficient phases into highly crystalline pyrite. The lattice parameter of the cubic pyrite was calculated from the XRD pattern as a = b = c = 5.4154 Å which corresponds well with the published literature [77, 107]. Sharp and narrow Raman peaks are positioned at 343 cm^{-1}, which corresponds to the E_g mode, 379 cm^{-1} for the A_g mode, and 430 cm^{-1} for the T_g Raman mode. Another weak Raman peak is often shown for pyrite at 350 cm^{-1}, which also corresponds to the T_g mode [104]. A_g and T_g Raman modes reflect the in-phase and out-of-phase stretching vibrations of the sulfur dimer S_2. In the E_g phonon mode, sulfur atoms are displaced perpendicular to the axis of the S-S bond [105].
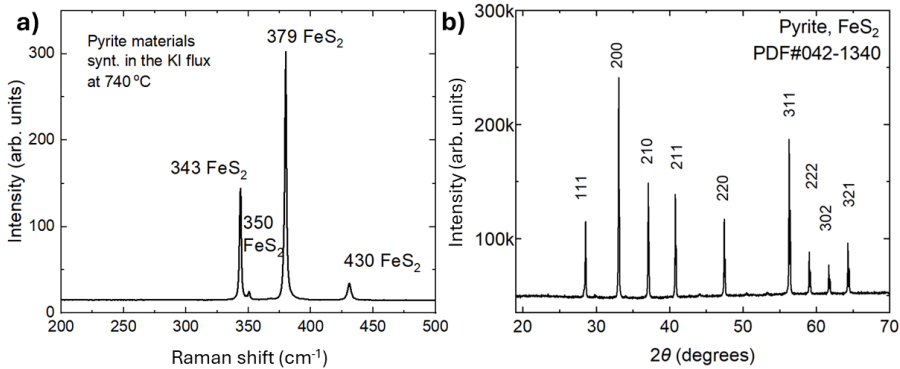

Figure 11: a) Raman spectra and b) XRD pattern of the FeS_2 microcrystals synthesized in the liquid phase of KI. The analysis revealed a high crystalline quality of only the pyrite phase.

The morphology of the pyrite microcrystals recrystallized in KI is illustrated in Figure 12. The individual crystals are formed as monograins and exhibit mostly uniform shapes and smooth surfaces. Some sintering of smaller crystallites is still present, though its impact on the final properties is less significant. The average crystal size is between 36-100 μm, suitable for application in the absorber of a monograin layer solar cell. The EDX analysis confirmed a near-stoichiometric ratio of Fe and S with an average composition of 33.71 at% Fe and 66.29 at% S, also shown in Table 5.

The superior performance of KI as a flux is likely attributed to its lower viscosity at synthesis temperatures, which facilitates improved precursor dissolution and mass transport, promoting the growth of larger microcrystals. The viscosity of KI at 740 °C is 0.0012 Pa*s [108], while the viscosity of sulfur at its boiling point 445 °C (below the synthesis temperature), is 0.1 Pa*s [109].
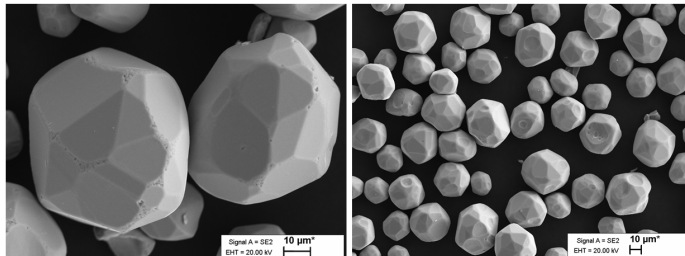

Figure 12: SEM images of the FeS$_2$ microcrystals synthesized in the liquid phase of KI at 740 °C.

To simplify the pyrite synthesis-growth process, some samples were synthesized directly in KI flux, omitting the initial sulfur-flux synthesis step and subsequent KI recrystallization. These directly synthesized pyrite materials exhibited similarly high crystallinity and superior morphological quality. Due to the high similarity between the materials recrystallized in KI and synthesized in KI, the Figures 11 and 12 represent both of these material groups.

Hot probe measurements revealed that all FeS$_2$ crystals synthesized in KI flux exhibit *n*-type conductivity.

This synthesis method was taken as a basis to carry out all the subsequent experiments in this thesis.

3.3 Surface composition of FeS$_2$ microcrystals synthesized in S and KI flux

X-ray photoelectron spectroscopy (XPS) was employed to investigate the surface composition of the FeS$_2$ crystals, as the surface chemistry of pyrite is widely recognized as a critical factor influencing its physical and electronic properties. Crystals synthesized in both sulfur flux and KI flux were analyzed. For the samples synthesized in sulfur, XPS measurements were conducted following the flux removal via vacuum sublimation, and again after subsequent etching with a 10% KCN solution. In the case of the materials synthesized in KI, the flux was removed by leaching in water prior to analysis. An additional etching step was performed to investigate the surface further, using a 3:1 volume ratio of H$_2$SO$_4$ and H$_2$O$_2$. The mixture is commonly referred to as "Piranha" solution. "Piranha" etching has been reported [57] to effectively strip the oxidized surface layer of pyrite, exposing a cleaner, more representative surface. XPS spectra were recorded after this treatment as well.

Due to the high surface sensitivity of XPS, it is common practice to perform mild argon ion (Ar$^+$) sputtering to remove surface contaminants before spectral acquisition. In this study, XPS spectra of the pyrite materials were recorded both before and after surface cleaning by Ar$^+$ sputtering. The Fe 2p and S 2p core-level spectra are presented in Figure 13. Prior to sputtering, the Fe 2p region displays peaks at 707, 708, and 713.8 eV (Figure 13a). The dominant signal at 707.0 eV is attributed to Fe^{2+} [46], which is characteristic of stoichiometric pyrite. The additional peaks at 708 and 713.8 eV correspond to Fe^{3+} species [46, 110, 111], likely resulting from surface oxidation. Following Ar$^+$ sputtering,

these distinct peaks merge into a broader, less resolved envelope, making it difficult to distinguish between Fe^{2+} and Fe^{3+} states (Figure 13a). The impact of sputtering is even more pronounced in the S 2p region (Figure 13b). Before sputtering, the spectra exhibit a well-defined doublet at 162.5 eV (S $2p_{3/2}$) and 163.6 eV (S $2p_{1/2}$), with a spin–orbit splitting of 1.2 eV, consistent with the disulfide S_2^{2-} species in pyrite [46, 111]. After Ar^+ sputtering, a new, intense peak emerges at 161.3 eV, corresponding to monosulfide S^{2-} species [112]. This shift indicates that the Ar^+ etching not only removes surface contamination but also induces chemical damage to the pyrite surface, altering the original oxidation states and forming new sulfide species. This phenomenon is consistent with the surface degradation observed during mechanical fracturing of pyrite, as previously reported by Nesbitt et al. [46]. Given the destructive effects of Ar^+ sputtering on the surface chemistry, all XPS data presented in Figure 13 correspond to measurements taken before ion etching.
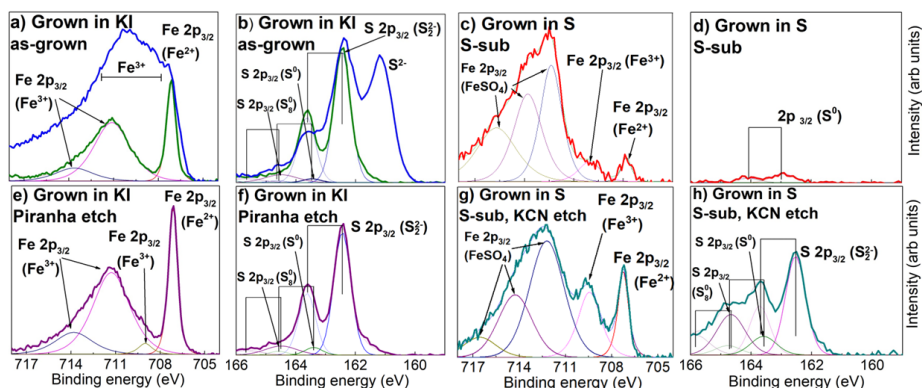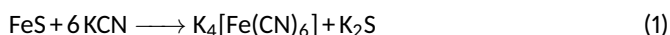

Figure 13: XPS core level spectra of pyrite samples from the Fe 2p and S 2p spectral regions. a-b) Fe 2p and S 2p spectra of FeS$_2$ synthesized in KI flux, the flux has been removed by leaching in water. Green line: before (Ar$^+$) sputtering, blue line: after (Ar$^+$) sputtering. Because the sputtering had a strong negative effect on the readability of the spectra, the fitting and analyses for the rest of the materials were done before (Ar$^+$) sputtering. e,f) Fe 2p and S 2p spectra of the same material, after etching with the "Piranha" solution (H$_2$SO$_4$ + H$_2$O$_2$). c, d) Fe 2p and S 2p spectra of FeS$_2$ synthesized in sulfur flux, the flux has been removed by vacuum sublimation. g, h) Fe 2p and S 2p spectra of the same material, after etching with a 10% KCN solution.

In the case of materials synthesized in KI flux, the Fe^{2+} signal at 707 eV is consistently accompanied by Fe^{3+} components, indicating the formation of a fractured surface even after simple flux removal via water leaching (Figure 13a). This behavior highlights the intrinsic instability of the pyrite surface, where S–S bonds are prone to breaking, sometimes even under ultra-high vacuum conditions [46]. Upon cleavage of these disulfide bonds, the resulting dangling sulfur bonds require electronic compensation, often drawing electrons from neighboring Fe^{2+} ions and thereby oxidizing them to Fe^{3+}. This surface oxidation leads to the introduction of defect states within the pyrite band gap [10, 46, 111]. Following etching with the "Piranha" solution, the Fe^{2+} signal becomes more prominent relative to the Fe^{3+} peaks, suggesting partial reduction of the oxidized surface (Figure 13e). However, a new Fe^{3+} peak also emerges post-treatment, indicating the possible formation of a secondary Fe$_2$O$_3$ phase [111]. In contrast, the Fe 2p spectral region of samples synthesized in liquid sulfur flux exhibits markedly different characteristics. When the sulfur flux was removed solely by vacuum sublimation, the Fe^{2+} signal at 707 eV had a similar intensity to the Fe^{3+} signal, but there were intense peaks associated with FeSO$_4$ [110, 111], observed between 712.2 and 716.6 eV (Figure 13c). The

presence of sulfate species is likely attributable to oxygen contamination introduced via impure synthesis precursors or aged sulfur flux exposed to ambient air, leading to surface oxidation prior to crystal growth. After etching with a KCN solution, an increase in the Fe^{2+} signal is observed; however, the Fe^{3+} signal also intensifies, and the $FeSO_4$ peaks remain prominent (Figure 13g). These results suggest that the KCN etching process may dissolve iron species from the surface in multiple oxidation states, rather than selectively reducing the oxidized layer. The following surface reaction is responsible for the dissolution of Fe on the surface:

$$FeS + 6\,KCN \longrightarrow K_4[Fe(CN)_6] + K_2S \tag{1}$$

In the S 2p region of the XPS spectra for materials synthesized in KI flux, several sulfur species are observed. Alongside the characteristic S_2^{2-} doublet at 162.5 eV (S $2p_{3/2}$) and 163.6 eV (S (S $2p_{1/2}$)) [112, 113], signals corresponding to elemental sulfur (S^0) appear at 163.5 and 164.7 eV, as well as features associated with polymeric sulfur species (S^8) at 164.6 and 165.8 eV (Figure 13b). These additional signals are attributed to residual unreacted sulfur on the crystal surface. Notably, etching with the "Piranha" solution did not significantly alter the sulfur chemical states (Figure 13f). For materials synthesized in sulfur flux, the XPS analysis revealed a markedly different surface composition. After sulfur removal via vacuum sublimation, virtually no sulfur was detected on the surface, indicating that sublimation is highly effective, not only in removing residual flux but also in depleting sulfur from the outermost atomic layers of the pyrite lattice (Figure 13d). As discussed in previous chapters, this results in an extremely sulfur-deficient surface. Following etching with a KCN solution, the characteristic disulfide S_2^{2-} doublet at 162.5 and 163.6 eV reappears, along with signals corresponding to elemental sulfur (Figure 13h). These findings prove that KCN treatment selectively removed iron from the pyrite surface according to reaction (1), thereby exposing a more stoichiometric sulfur surface typical of pyrite.

In summary, the XPS analysis revealed that a) vacuum sublimation proved overly aggressive, resulting in a surface composition inconsistent with stoichiometric pyrite; b) the "Piranha" etching treatment, as applied in this study, had limited effectiveness in reducing surface oxidation or restoring the pyrite surface; c) materials synthesized in KI flux more closely resembled stoichiometric pyrite, exhibiting lower levels of surface oxidation and minimal formation of $FeSO_4$.

3.4 Pyrite-based Schottky diodes and heterostructure

Pyrite microcrystals, synthesized via the molten salt synthesis-growth method in KI, were sieved into narrow size fractions and used to fabricate monograin membranes. The detailed procedures for monograin membrane fabrication are provided in Papers I and II. In an effort to mitigate or reduce the extent of this inversion layer, surface etching using a "Piranha" solution was employed, a method previously reported in the literature [42, 56]. Although the XPS results presented in Paper I indicated minimal positive impact from this treatment, junction fabrication was conducted to confirm these findings. Etching durations of 10 and 60 seconds were applied to assess any potential improvements.

Schottky diodes were fabricated as an initial step in junction formation. While the work function of pyrite is commonly reported to be approximately 4.7 eV [114, 115], our measurements indicated higher values, ranging between 5.9 and 6.0 eV (Paper III). This discrepancy could be caused by the different measurement techniques used to extract the ϕ value. The work function reflects a material's surface condition, and pyrite's surface can differ under different preparation or environmental conditions. In our case, the

crystals exhibit an inhomogeneous surface compared with thin films. This makes UPS measurements challenging and naturally results in spatial variation in the extracted ϕ values. To ensure junction formation, a contact metal with a higher work function is required. Platinum (ϕ = 6.1 eV, [116]) and gold (ϕ = 5.45 eV, [117]) were selected and sputtered onto the pyrite monograin membranes. Figure 14a presents the current–voltage (I–V) characteristics of the resulting Schottky diodes. The data confirm the formation of weakly rectifying junctions, although the built-in voltage could not be determined from the I–V curves. A slight improvement in the curve shape was observed following surface etching with "Piranha" solution.
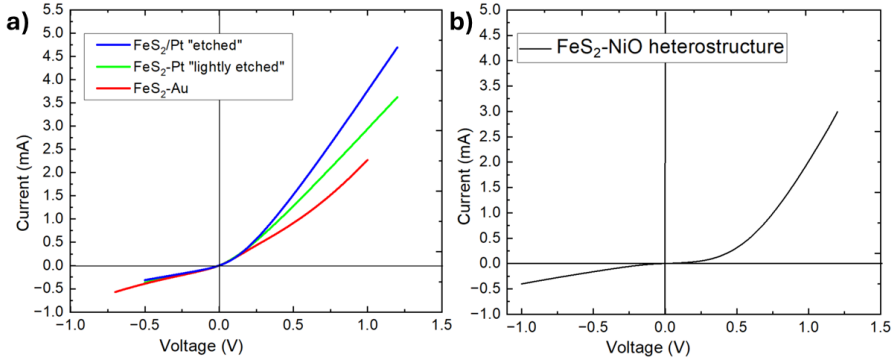

Figure 14: Current-voltage graphs of pyrite-based devices in the dark. a) Schottky diodes based on pyrite-gold and pyrite-platinum junctions. The pyrite-Pt junctions have been etched with the "Piranha" solution for either 10 s for "lightly etched", or 60 s for "etched". b) pyrite-nickel oxide heterostructure.

To form a *p–n* junction, the *n*-type pyrite membranes were coated with a thin film of *p*-type nickel oxide (NiO). The NiO layer was deposited via solution deposition, using a procedure adapted from Akaltun et al [118]. The corresponding I–V characteristics are shown in Figure 14b. While a modest rectification was observed in the shape of the I-V curve, a negligible photocurrent generation was detected under illumination, indicating an ineffective photoresponse in the device. Compared to the Schottky diodes, the heterostructure's I-V curve shape was improved, showing a high potential for further improvement with optimization of the solar cell architecture. In the latter device, the absorber material is still affected by the surface inversion layer; if the surface effects can be removed or bypassed by synthesizing doped materials, the device's photoresponse could likely increase.

Carrier concentrations of 6.2×10^{16} cm^{-3} and 2.5×10^{17} cm^{-3} were determined from capacitance–voltage (C–V) measurements of FeS$_2$/NiO heterojunctions and FeS$_2$/Pt Schottky diodes, respectively. These values fall within the desirable range for semiconductor applications in photovoltaic devices and are consistent with those reported in the literature [119, 120].

3.5 Effects of alkali metal impurities in pyrite microcrystals

Pyrite microcrystals were synthesized in different flux salt environments as described in the Experimental section, Chapter 2.2, Table 3. It was hypothesized that FeS$_2$ precursors have different solubilities in different flux environments, potentially enabling the growth of larger crystals. Microcrystals with larger diameters are generally more manageable
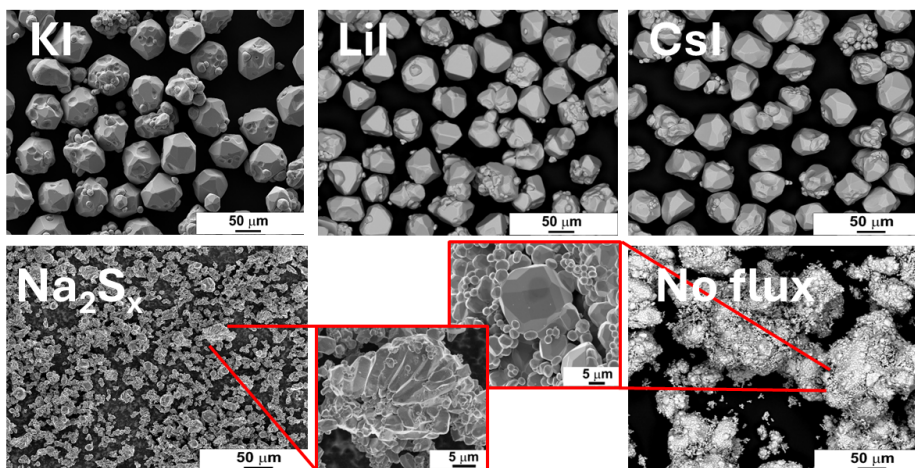
Figure 15: *Scanning electron micrographs of pyrite microcrystals synthesized in KI, LiI, CsI, Na_2S_x, and without any flux. The crystals grown in iodide salts have formed as individual monograins.*

for handling and analysis. Additionally, it is known that constituent elements of the flux salt can incorporate into the growing crystals during synthesis. The inclusion of alkali metal impurities presented an opportunity to explore their influence on the material's properties, as it had not been investigated before.

3.5.1 Changes in the morphology and average size of crystals

The morphology of crystals synthesized in different fluxes was analysed by SEM and is illustrated in Figure 15. The FeS_2 crystals obtained from KI, LiI, and CsI fluxes exhibited similar features, characterized by rounded crystal shapes and smooth surfaces. Some smaller crystallites were also attached to larger ones because during synthesis, FeS_2 crystals are dispersed in the liquid flux. As the system cools and the flux solidifies, these small crystals can no longer grow into larger ones. The synthesis mixture contains sulfur, which is liquid above 112.9 °C [109] while KI is already solid. The liquid sulfur can cause some crystals to adhere and "stick" to one another.

The particle size distribution of pyrite crystals synthesized in KI, LiI, and CsI fluxes is presented in Figure 16. The data indicate no significant variation in the average crystal size across the different fluxes, suggesting that the solubility of the precursors is comparable in all three iodide salts. Given that crystal growth during synthesis proceeds predominantly via a single mechanism (the Ostwald ripening [69]), the resulting size distribution approximates a Gaussian profile.

The materials synthesized in Na_2S_x exhibited similar morphology to those obtained without the use of any flux (Figure 15, Na_2S_x and no flux). In both cases, well-defined individual crystals were not observed. Instead, the products consisted of small crystallites that had sintered together, forming polycrystalline aggregates. These syntheses were conducted at lower temperatures compared to those using iodide salts, due to the lower melting point of Na_2S_x (above 250 °C [75]) and the formation temperature of FeS_2 (445 °C [37]). The observed morphology suggests that crystal growth proceeded too slowly at these lower temperatures, which is likely the reason for the lack of distinct crystal formation. Another likely reason for the observed sintering is an insufficient amount of liquid phase between solid particles during the synthesis-growth.
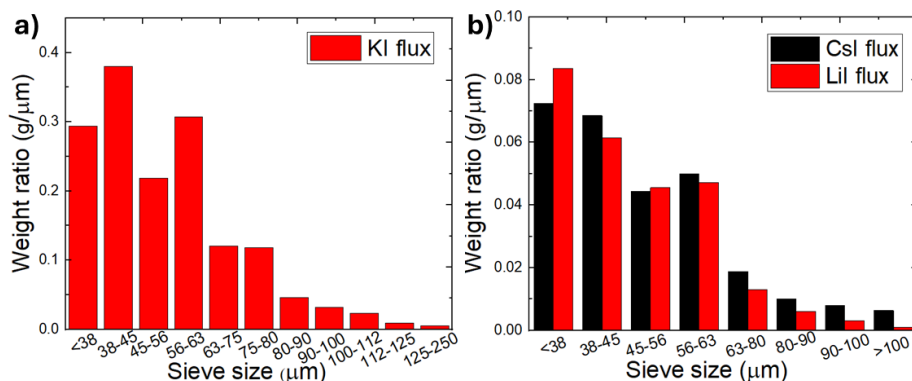
Figure 16: Particle size distribution analysis of pyrite materials synthesized in a) potassium iodide flux, and b) lithium iodide and cesium iodide flux.

Due to the polycrystalline nature of the products synthesized in Na_2S_x and without flux, particle size distribution analysis was not performed.

3.5.2 Composition and impurities concentration in pyrite microcrystals

All FeS_2 materials synthesized in different flux salts exhibited near-stoichiometric Fe/S ratios ($\sim$0.5), as determined by EDX. Exact atomic percentages are provided in Paper III. While the Fe and S ratios of pyrite crystals were consistent across different materials, impurity concentrations varied significantly. Impurities were analyzed via inductively coupled plasma mass spectrometry (ICPMS) and revealed that, despite using potassium- and sodium-containing salts, these impurities were either undetectable or present below the detection limit. A high lithium impurity concentration of 4×10^{19} cm^{-3} was observed only in the material synthesized with LiI. This result is consistent with expectations; however, such a high level suggests the potential formation of a solid solution. The comparison of Li impurity concentrations is shown in Figure 17a.

A high cesium (Cs) impurity concentration of 10^{19} cm^{-3} was detected in the material synthesized with CsI, illustrated in Figure 17b. Interestingly, a relatively high Cs concentration was also found in the material synthesized with LiI. Analysis of the flux salts revealed that the LiI contained Cs impurities, likely due to similar fabrication conditions or cross-contamination during manufacturing. Additionally, materials synthesized in iodide salts showed iodide concentrations ranging from 1–4 $\times 10^{19}$ cm^{-3}. This was unexpected, as iodine has a relatively large ionic radius compared to Fe and S, and its incorporation at such high levels could distort the pyrite crystal lattice.

Similar trends were confirmed through qualitative analysis using time-of-flight secondary ion mass spectrometry (ToF-SIMS), Figure 17c. While ToF-SIMS does not provide absolute impurity concentrations, it also detected the presence of Li and Cs in the samples. K and Na impurities, which were not detected by ICPMS, were recognized by the very sensitive ToF-SIMS. Cu and Ni were also identified in comparable intensities, along with iodine in materials synthesized using iodide salts. Due to the surface sensitivity of ToF-SIMS and matrix effects inherent to the technique, the measured concentrations are only comparable within each impurity type, between pyrite samples synthesized by different methods.

The concentration of transition metal impurities (Cr, Cu, Co, and Ni) in all pyrite samples ranged around $\sim$$10^{18}$ atoms per cm^3, as found by ICPMS. The exact
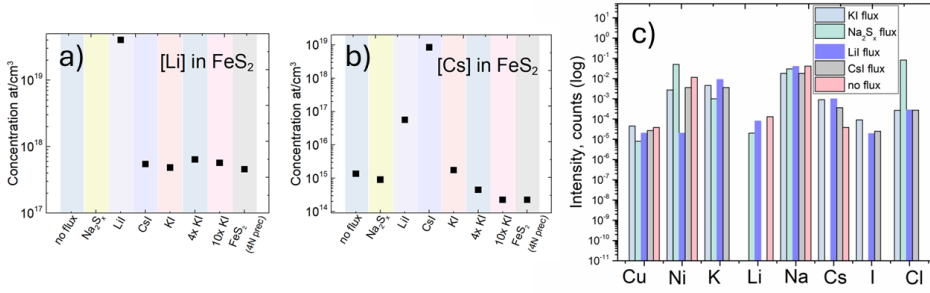
Figure 17: Impurity concentrations in the pyrite materials synthesized in different flux media. a) Li impurity concentration across the materials, analysed by ICPMS. b) Cs impurity concentration, analysed by ICPMS. c) Qualitative comparison of different impurity elements in pyrite materials, analysed by ToF-SIMS.

concentrations are brought in Paper III. The similarity in impurity levels across samples suggests a common source: the FeS precursor. ICPMS analysis of the FeS precursor confirmed the presence of transition metal impurities at concentrations of $\sim 10^{18}$ cm^{-3}. To improve purity, a higher-grade (99.99%) FeS precursor was tested; however, its impurity profile was nearly identical to that of the initial 99.9% purity FeS precursor. This unexpected result led us to explore alternative methods for reducing transition metal impurities.

A common method in semiconductor processing, the liquid-phase recrystallization, was employed to investigate impurity reduction. Larger quantities of KI were used, as the purification relies on the impurity's difference in solubility between the solid and liquid phases at the recrystallization temperature, governed by the impurity's distribution coefficient. Recrystallization in increased amounts of KI was effective in significantly reducing the copper impurity, while concentrations of other transition metals (Cr, Co, Ni) either decreased marginally or remained unchanged. This is a notable result, as Cu in pyrite is known to form chalcopyrite secondary phases with narrower band gaps (0.53–0.63 eV) than pyrite, or nanocrystals with band gaps around 1.2 eV [121]. Our own experiments have confirmed that Cu incorporation suppresses photoluminescence in pyrite, indicating increased non-radiative recombination. In summary, Cu exhibits high solubility in KI, and recrystallization using four to ten times the standard flux amount effectively reduces the Cu impurity - an outcome not achieved by using a higher purity (99.99%) FeS precursor alone.

3.5.3 Phase composition and electronic band structure of FeS$_2$ crystals with different impurities' concentrations

The next step was to investigate how the detected impurities influence the properties of pyrite. Phase analysis was performed using Raman spectroscopy and X-ray diffraction (XRD), as shown in Figure 18. Characteristic Raman peaks for the pyrite phase were observed at 343, 379, and 430 cm^{-1}, with a weaker peak at 350 cm^{-1}. The peaks at 343, 379, and 430 cm^{-1} correspond to the E$_g$, A$_g$, and T$_g$ Raman modes, respectively [104].

XRD analysis confirmed a single pyrite phase, with a calculated lattice parameter of a = b = c = 5.4154 Å. Neither the lattice parameter nor the positions of the Raman peaks varied across the samples, suggesting that the impurity concentration is sufficiently low to avoid affecting the crystal lattice - a controversial result, as we had observed a relatively high impurity concentration from the mass spectroscopy data.
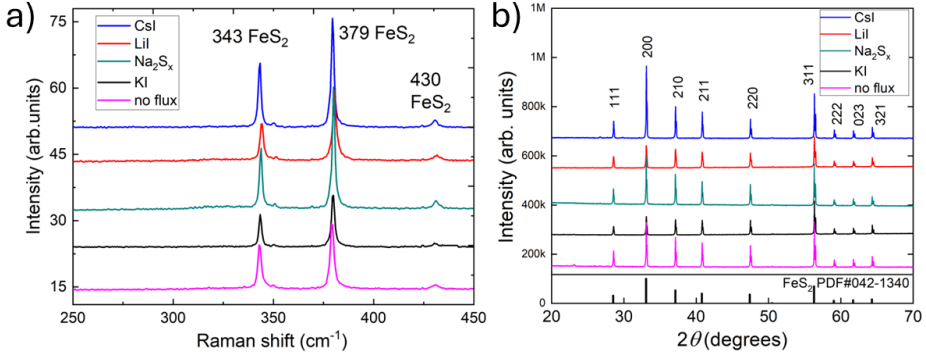
Figure 18: Comparison of the phase composition of the pyrite samples synthesized in different flux media by a) Raman spectroscopy, and b) X-ray diffraction.

Ultraviolet photoelectron spectroscopy (UPS) was used to determine the valence band maxima (E_{VBM}) and Fermi levels of pyrite materials synthesized in different fluxes. All measurements were performed under identical UV excitation conditions and fixed geometries between the samples and the UV source to ensure comparability. Similar to XPS (discussed in Section 3.3), UPS is highly surface-sensitive, and surface contamination is commonly removed via Ar^+ sputtering. However, due to the defect-sensitive nature of pyrite surfaces, sputtering rendered the UPS spectra unreadable. Therefore, all spectra presented in Figure 19 were recorded prior to Ar^+ sputtering.

Figure 19a presents a comparison of the full He(I) UPS spectra of FeS_2 in the binding energy range, which enables the determination of the work function (ϕ) and extraction of the Fermi level. The work function of FeS_2 was calculated using Equation (2) [122].

$$\phi = h\nu - E_{cutoff} \qquad (2)$$

where $h\nu$ is the excitation energy of He(I) line at 21.21 eV, and E_{cutoff} is the secondary electron cutoff energy, obtained by linearly fitting the high binding energy edge of the FeS_2 spectra. The energy difference between the Fermi level (E_F) and the E_{VBM} was extracted by fitting the low binding energy edge of the spectra shown in Figure 19b. All FeS_2 samples exhibit a low-intensity peak near E_F (0 eV), which introduces some ambiguity in fitting this region. This feature is most pronounced in the sample synthesized without any flux, suggesting the presence of states above the E_{VBM}, with intensity proportional to the photoelectron counts. A similar phenomenon was previously reported by Cabán-Acevedo et al. [40] in their investigation of pyrite's band structure, though its origin remains unresolved. One plausible explanation is a sulfur-deficient surface, not unknown for pyrite, which induces metal-like behavior and shifts the surface chemistry toward the narrower band gap of FeS [123]. If this modified surface region is sufficiently thin, it might not be detected by EDX or XRD, but be observable by surface-sensitive methods like UPS. All E_F values were extracted without accounting for the low-intensity peaks near 0 eV, as fitting them would yield negative energy values, not representative of the properties of pyrite.

Figure 20 shows the energy band diagrams of all pyrite samples, constructed from the UPS measurement data. The materials synthesized or recrystallized in KI exhibit similar band alignments, with E_{VBM} values around –6.0 eV relative to the vacuum level. In contrast, samples synthesized in LiI, CsI, and Na_2S_x display shifted band diagrams, with
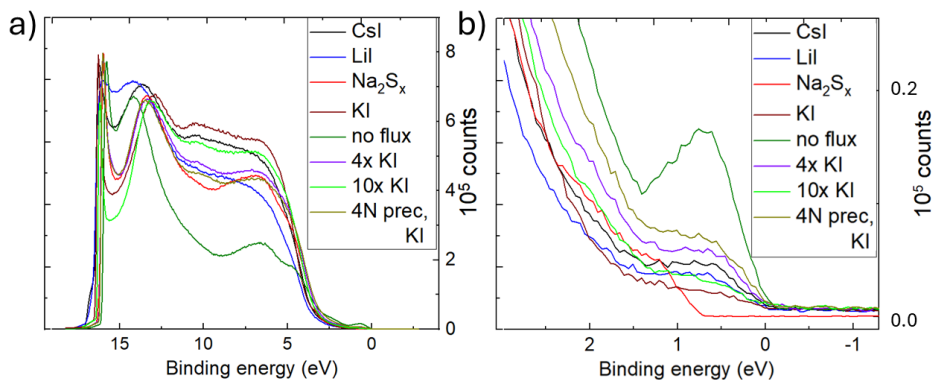
Figure 19: a) Full He(I) UPS spectra of pyrite materials synthesized in different flux media. b) The same spectra zoomed in near the E_F, exhibiting a brief increase in counts near 0 eV.
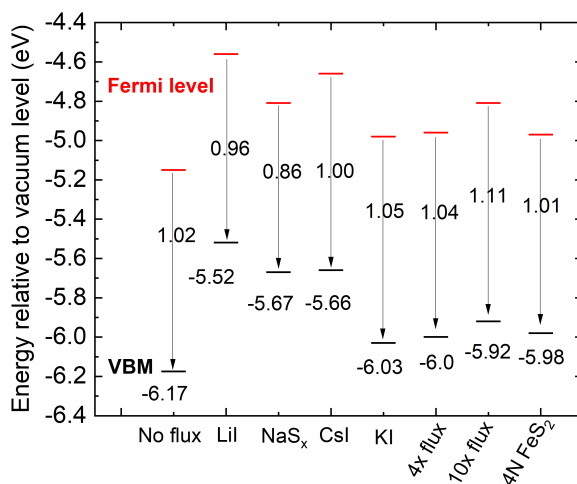

Figure 20: Energy band diagram of the pyrite materials synthesized in different flux media, based on the data derived from the UPS measurements.

lower E_{VBM} energies. Changes in E_{VBM} values suggest the formation of solid solutions, further supported by the mass spectroscopy results discussed in Section 3.4.2, which revealed elevated concentrations of Li and Cs impurities in these samples. Interestingly, phase analysis by Raman spectroscopy and XRD did not indicate the presence of secondary phases. It is therefore proposed that secondary phases such as Li_2S and Cs_2S may exist only at the surfaces of the pyrite crystals and in quantities too low to be detected during phase analysis.

The work function values of the various FeS_2 samples were determined from the E_{cutoff} edge using Equation (2). The extracted ϕ values ranged from 4.6 to 5.1 eV, aligning well with literature-reported values for pyrite, which typically fall between 4.8 and 5.4 eV.

The band gap of pyrite is commonly reported to be approximately 1 eV. Based on the measured positions of the valence band maximum (E_{VBM}) and Fermi level (E_F), and

40

considering the expected location of the conduction band minimum (E_{CBM}), there is strong evidence that the materials exhibit *n*-type conductivity, as E_F lies closely under the E_{CBM}.

Among all samples, the material synthesized without flux is expected to be closest to intrinsic pyrite, due to its lower impurity concentration. The band diagrams most similar to this reference sample are those of materials synthesized in the KI flux. Furthermore, all samples recrystallized in KI display highly similar band diagrams. This suggests that the substantial reduction in the Cu impurity, observed after recrystallization in high volume of KI, as discussed in Section 3.4.2, does not significantly affect the electronic band structure of pyrite.

3.5.4 Photoluminescence study of the pyrite materials synthesized in different fluxes

Photoluminescence (PL) spectroscopy is a reliable technique for investigating the recombination mechanisms of photoexcited charge carriers in semiconductors. Despite over three decades of research into pyrite as a photovoltaic absorber, PL studies on this material remain scarce in the literature. Therefore, research looking into the PL recombination in pyrite crystals was highly necessary. It is well documented [9, 41] and supported by our own observations that pyrite surfaces are prone to degradation under ambient conditions. Specifically, iron ions readily oxidize, and the surface may become sulfur-deficient, leading to altered electronic properties. To mitigate these surface-related effects, the pyrite samples were etched using an aqueous NH_3 solution and immediately coated with a thin ZnS layer via solution deposition. This protective ZnS film, approximately 10 nm thick, prevents further atmospheric interaction and surface inversion [124]. ZnS does not have a PL signal within the 0.8–1.3 eV spectral range, ensuring that it does not interfere with the pyrite signal.
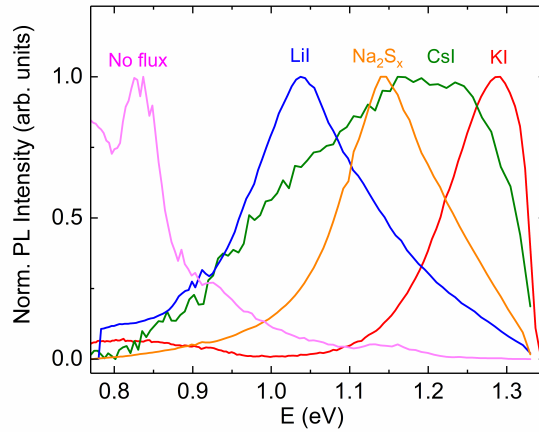

Figure 21: Normalized PL spectra of FeS$_2$ microcrystals synthesized in different molten salt media. The spectra were recorded at 10 K.

Low-temperature (10 K) PL spectra of FeS$_2$ samples synthesized using various molten salt fluxes are presented in Figure 21. The normalized spectra reveal that the PL bands differ in both peak position and spectral shape, indicating variations in the underlying recombination mechanisms and potentially reflecting changes in the FeS$_2$ band gap. Similar observations have been reported by Ghisani et al. [71], where materials

synthesized in different molten salt environments showed PL peaks at varying energies. The asymmetric shape of the PL bands suggests that the materials are heavily doped, and that recombination is likely dominated by transitions involving exponential band tails [125].

Among the studied samples, the material synthesized in KI exhibited the highest-energy PL band near 1.3 eV, accompanied by a weaker band at approximately 0.8 eV, as can be seen in Figure 21. Similarly, the sample synthesized without any flux displayed a low-intensity, noisy PL signal centered around 0.8 eV. The peaks near 0.8 eV likely originate from the same source, possibly related to deep defects. On the other hand, the UPS measurements suggested the possibility of the formation of solid solutions in the case of materials containing Li and Cs impurities. The samples synthesized in CsI, Na_2S_x, and LiI exhibited PL bands at 1.2 eV, 1.1 eV, and 1.05 eV, respectively. Given that the widely accepted band gap of pyrite FeS_2 lies in the range of 0.9–1.0 eV [9, 10], the observed PL bands above 1.0 eV could suggest a secondary phase. Another possible explanation is the formation of nanocrystals on the pyrite surface, where quantum confinement effects could result in a widened effective band gap. If these nanocrystals contain copper, a common impurity in the materials of this study, their emission characteristics could resemble chalcopyrite ($CuFeS_2$) nanocrystals, which are known to have a band gap around 1.2 eV [121]. Samples that were recrystallized in higher concentrations of KI, and in which the copper content was significantly reduced, did not exhibit any measurable PL signal, possibly proving this assumption. Another possible cause for the observed higher-energy PL bands for some of the materials is valence band splitting. This phenomenon has been reported in the case of transition metal disulfides like MoS_2. The group reported a change in the PL band positions to higher energies after increased valence band splitting due to spin-orbit coupling [126].

These results are preliminary and warrant further investigation. However, they suggest that variations in impurity content and secondary phase formation have a significant impact on the recombination mechanisms and possibly also on the apparent optical band gap of pyrite.

3.6 *P*-type doping of pyrite microcrystals with phosphorus

Hot probe measurements had confirmed that the synthesized crystals exhibit *n*-type conductivity (Papers I, II, III), which is consistent with literature reports [42, 53]. However, the outermost surface of pyrite crystals has been reported to exhibit *p*-type conductivity [9, 42–44]. There has been no significant progress in removing or passivating the surface layer in earlier studies, so the attention shifted to achieving uniform electrical properties across the bulk material.

Phosphorus (P), previously reported to induce *p*-type conductivity in pyrite synthesized via the chemical vapor transport method [21], was selected as the dopant for the synthesis of *p*-type FeS_2 microcrystals. Three doping strategies were explored to achieve *p*-type conductivity in pyrite. The first approach involved doping via the gas phase, a method commonly employed in semiconductor processing and adapted here accordingly. The second strategy leveraged our previous findings (Paper III), which demonstrated that elements from the flux salt are incorporated into the pyrite lattice during synthesis, thereby altering the electronic band structure and recombination mechanisms. Based on this, phosphorus was introduced through the molten flux phase. The third method involved synthesizing pyrite in the presence of a phosphorus-containing compound as a dopant source. A more detailed description of the experimental setup of phosphorus treatments is available in Paper IV.

3.6.1 Doping strategy 1: heat treatment in P vapor atmosphere

In the first doping strategy, previously synthesized FeS_2 crystals were placed in two-chamber quartz ampoules along with a few milligrams of elemental phosphorus. The ampoules were sealed and heat-treated at 500 °C for 48 hours. The FeS_2 material used for this treatment had been synthesized in KI flux, as described in Papers I and II. Following exposure to the phosphorus vapor atmosphere, the samples exhibited visible cracking and the formation of two distinct phases. EDX analysis identified a stoichiometric pyrite phase alongside a phosphorus-rich ternary region, with phosphorus concentrations of 20–25 at%. Cracking and fragmentation occurred within the ternary mixed phase. SEM images of the surface and cross-sections of the treated crystals are presented in Figure 22. The P-rich phase exhibited a leafy, layered morphology and appeared less dense than FeS_2, which may account for the observed cracking.

Phase analysis was performed using Raman spectroscopy, as shown in Figure 22. The spectra revealed characteristic peaks at 343, 350, 379, and 431 cm^{-1}, corresponding to the pyrite phase [102, 103]. Additional peaks at 247 and 279 cm^{-1} were observed in the mixed phase region and were attributed to the iron thiophosphide $FePS_3$ [127].

Hot probe measurements confirmed that the treated crystals exhibited *n*-type conductivity. These results suggest that this doping method is unsuitable for obtaining *p*-type pyrite crystals.
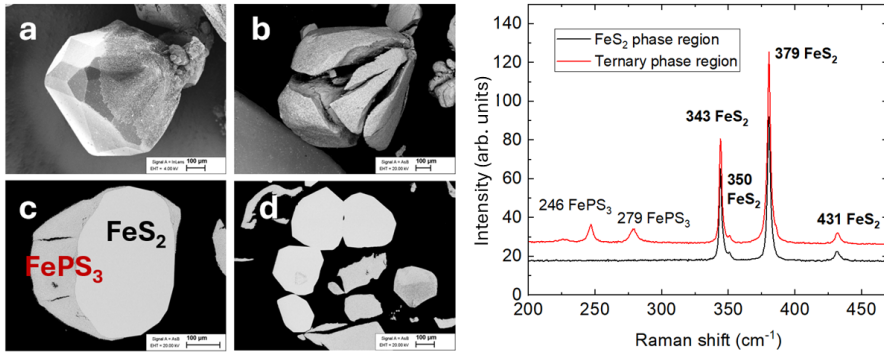

Figure 22: Left: SEM images of the FeS_2 microcrystals after heat treatment in the phosphorus vapor atmosphere. a-b) crystals' surface. c-d) cross-sectional images. Right: Raman spectra of the FeS_2 microcrystals cross-section after heat treatment in the phosphorus vapor atmosphere.

3.6.2 Doping strategy 2: recrystallization in the liquid mixture of KI and P

In the second doping series, phosphorus was added to the pyrite (FeS_2) crystals via the molten flux phase, enabling the dopant to be integrated into the lattice during the recrystallization process. Phosphorus concentrations ranging from 10 to 1000 ppm relative to FeS_2 were mixed with KI and added into quartz ampoules containing pre-synthesized pyrite microcrystals. Following recrystallization, the samples were examined by SEM, which revealed a significant improvement in crystal morphology compared to the previous series. As shown in Figure 23, no secondary phases or crystal fragmentation were observed. This result was further corroborated by Raman spectroscopy, shown in Figure 24, which displayed only sharp, well-defined peaks characteristic of the pyrite phase at 343, 350, 380, and 431 cm^{-1} [104]. However, hot probe measurements indicated *n*-type conductivity in the doped pyrite samples.
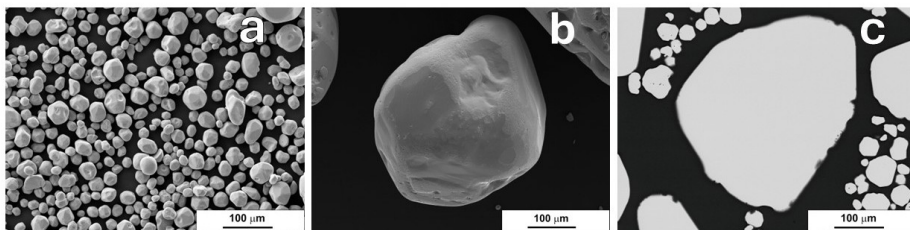
Figure 23: SEM images of the pyrite samples recrystallized in KI in the presence of 1000 ppm of phosphorus. a-b) crystals' surface. c) cross-sectional image.
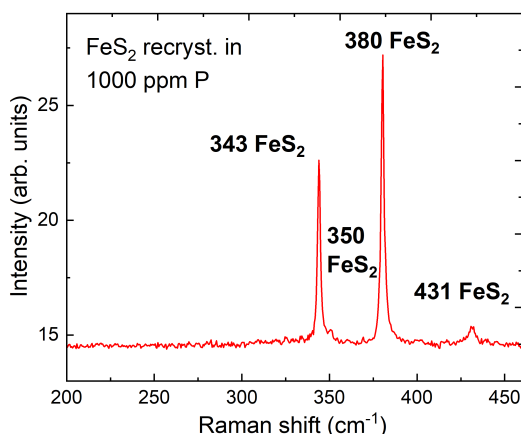

Figure 24: Raman spectrum of the pyrite material recrystallized in KI with 1000 ppm of phosphorus.

EDX analysis did not detect the presence of phosphorus, even in samples recrystallized with 1000 ppm P relative to FeS_2, meaning that the phosphorus concentration in pyrite is either below the detection limit of EDX or that phosphorus remained entirely dissolved in the molten KI flux without incorporating into the FeS_2 lattice. The latter scenario is plausible if the solubility of phosphorus in KI is significantly greater than in pyrite.

ICPMS measurements were conducted to investigate the concentration of phosphorus in the FeS_2 crystals, the results are presented in Table 6. Interestingly, the reference sample, which was not treated with any added phosphorus, exhibited the highest concentration of P impurity. In contrast, samples recrystallized in the presence of phosphorus displayed P concentrations below the detection limit of the ICPMS instrument. These findings suggest that phosphorus exhibits high solubility in molten KI, sufficient to prevent its incorporation into the pyrite lattice. KI is also able to extract the pre-existing phosphorus impurity from the solid phase. As a result, the final material contained a lower phosphorus concentration than the starting material. A similar "purification" effect was previously observed for the copper impurity, as reported in Paper III.

Building upon the findings from the first two doping strategies, it was determined that it is not feasible to incorporate phosphorus into the FeS_2 crystals after their synthesis. Phosphorus either reacts with pyrite or is lost between the solid and liquid phases when

Table 6: ICPMS analysis results of the pyrite materials recrystallized in the liquid phase of KI and added phosphorus.

Intended P level in FeS$_2$		Analyzed P content in FeS$_2$ ppm (molar basis)
0.004 at%	40 ppm	27 ppm
0.01 at%	100 ppm	29 ppm
0.03 at%	300 ppm	30 ppm
0.06 at%	600 ppm	32 ppm
0.1 at%	1000 ppm	39 ppm
Undoped, not treated		59 ppm

introduced in insufficient quantities. Rather, phosphorus must be incorporated into the pyrite lattice during the crystal growth process itself.

The limited incorporation of phosphorus in the previous series may be attributed to its oxidation state. According to The Chemistry of Imperfect Crystals by F. A. Kröger [128], effective doping of pyrite requires substitutional incorporation of phosphorus at sulfur lattice sites. Since sulfur in pyrite exists as S^{2-}, a phosphorus ion with the same charge state (P^{2-}) would not significantly influence the defect chemistry. To generate iron vacancies and promote *p*-type conductivity, phosphorus must be incorporated in the P^{3-} state. Thus, a suitable dopant must be a phosphorus-containing compound that remains chemically and thermally stable at the synthesis temperature, while also delivering phosphorus in a negatively charged state.

3.6.3 Doping strategy 3: synthesis of FeS$_2$ with a phosphorus anions

Two new precursors were synthesized to create stable compounds for doping pyrite with phosphorus. FeS and P were mixed in a 1:1 molar ratio (FeS+P), and Fe and P were prepared in the same way (Fe+P). The underlying hypothesis for the preparation of these precursors was to prevent the formation of the layered FePS$_3$ phase and to incorporate phosphorus in a favorable oxidation state. The FeS+P precursor was used for the synthesis and growth of pyrite crystals in molten KI flux. The FeS+P mixture was added into the synthesis ampoules in concentrations corresponding to 2, 3, 5, 7, and 10 at% phosphorus relative to sulfur in the pyrite lattice.

Following synthesis, the resulting materials were examined by SEM. Crystals synthesized with 2, 3, 5, and 7 at% phosphorus exhibited morphologies similar to those of undoped pyrite (as described in Papers I and II), with no signs of fragmentation or the presence of secondary phases. Representative images of the sample containing 5 at% phosphorus are provided in Figures 25a and 25b. In contrast, the sample synthesized with 10 at% phosphorus (Figures 25c and 25d) displayed minor surface cracking and some evidence of sintering, indicating possible structural stress or instability at higher doping levels.

Although the initial phosphorus concentrations used in the synthesis were relatively high, EDX detected only low amounts of phosphorus in the samples synthesized with 7 and 10 at% P, as summarized in Table 7. No phosphorus was detected by EDX in the samples with initial concentrations of 2, 3, and 5 at%. However, hot probe measurements indicated that the samples synthesized with 5, 7, and 10 at% phosphorus exhibited *p*-type conductivity. These results suggest that phosphorus doping of pyrite is feasible when a sufficiently high concentration of phosphorus is introduced in an appropriate chemical form or oxidation state. Based on this result, the material synthesized with 5 at%
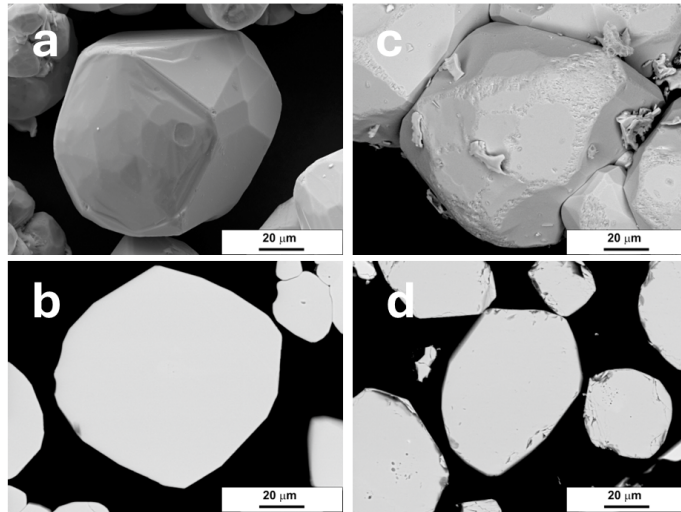
Figure 25: Surface and cross-sectional SEM images of the pyrite microcrystals synthesized with a,b) 5 at% phosphorus and c,d) 10 at% phosphorus.

Table 7: Phosphorus content detected by EDX, and corresponding conductivity type of pyrite crystals synthesized with 2–10 at% phosphorus.

Concentration of P in the FeS_2 synthesis	Concentration of P in the obtained material	Conductivity type, determined by hot probe
2 at%	0 at%	*n*-type
3 at%	0 at%	*n*-type
5 at%	0 at%	***p*-type**
7 at%	0-1.3 at%	***p*-type**
10 at%	0-1.4 at%	***p*-type**

phosphorus was selected for subsequent experiments and further characterization.

The phase composition of the material synthesized with 5 at% phosphorus was examined using Raman spectroscopy and XRD, as shown in Figure 26. Raman analysis revealed peaks characteristic of the pyrite phase, highly similar to the undoped reference sample synthesized in KI (Figure 26a). In contrast, the XRD pattern exhibited additional signals that were attributed to the presence of a secondary $FePS_3$ phase (Figure 26b). The $FePS_3$ phase was not detected during the Raman measurements, suggesting its presence in very low concentrations, as Raman analysis covers localized spots on individual crystals. In contrast, XRD collects data over a broader sample area. Importantly, the presence of this minor phase did not negatively impact any other crystal properties.

The precursor synthesized from elemental iron and phosphorus (Fe+P) was employed to synthesize phosphorus-doped pyrite with a target P concentration of 5 at%. The synthesis, as described previously, involved combining Fe+P, FeS, elemental sulfur, and KI, and heating the mixture at 690 °C. No significant changes in morphology or phase composition relative to undoped samples were revealed by SEM or Raman spectroscopy. All materials exhibited *n*-type conductivity, suggesting that doping was ineffective. Consequently, these results are not discussed further.
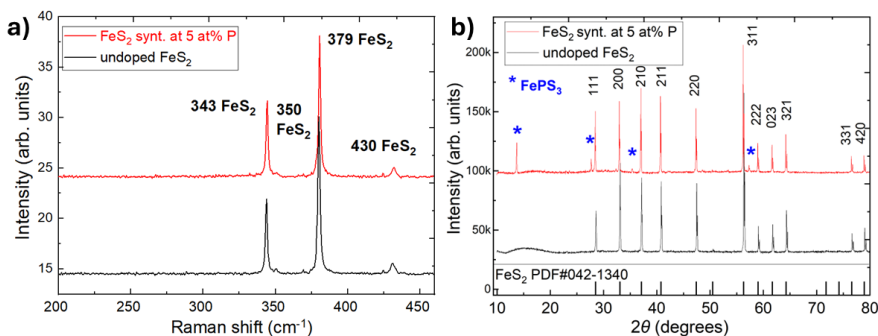
Figure 26: Phase analysis of the pyrite crystals synthesized in 5 at% phosphorus, compared to the undoped reference sample. a) Raman spectra, and b) X-ray diffractogram.

3.6.4 The proposed phosphorus compound and mechanism for doping pyrite

Identifying the compound that allows the effective p-type doping of FeS_2 crystals is critical for enhancing the reproducibility of this method. Phosphorus is known for adopting multiple oxidation states in different compounds [129, 130]. In the previous chapter, it was shown that the third doping approach, which uses the FeS+P precursor, successfully achieved conductivity type inversion, whereas using the Fe+P precursor did not yield p-type material. This suggests the presence of a specific compound in the FeS+P mixture, absent in the Fe+P system, that facilitates the incorporation of phosphorus into the FeS_2 lattice and promotes hole formation. XRD analysis was conducted to investigate the compositional differences between the two precursors and identify the phases present in each mixture. The results of this phase analysis are presented in Figure 27 and summarized in Table 8.
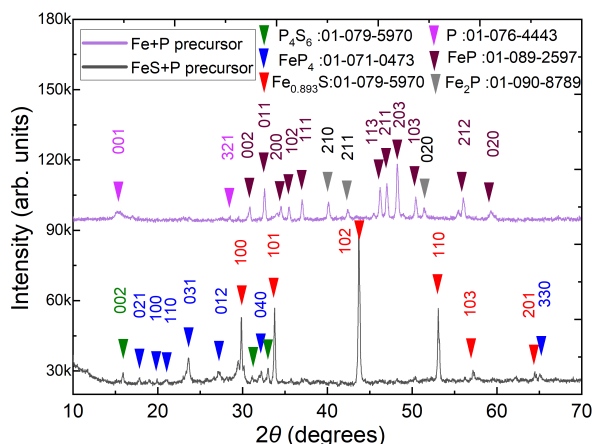

Figure 27: XRD patterns of the phosphorus precursors used to synthesize pyrite. Black line: precursor mixture prepared from FeS and P. Purple line: precursor mixture prepared from Fe and P.

The FeS+P precursor was found to contain P_4S_6, pyrrhotite ($Fe_{0.893}S$), and FeP_4, whereas the Fe+P precursor comprised elemental phosphorus, FeP, and Fe_2P. Among these, P_4S_6 and FeP_4 were unique to the FeS+P precursor, which was the only formulation that enabled successful phosphorus doping. This suggests that one of these compounds

Table 8: Summary of the phases present in the phosphorus precursors FeS+P and Fe+P, based on the XRD results.

Used precursor	Compounds present, determined by XRD	Quantity in the mixture	Charge of the phosphorus ion
Fe+P mixture, heated at 450 °C	Elemental phosphorus	9%	0
	FeP	72%	2-; 3-
	Fe_2P	19%	3-
FeS+P mixture, heated at 450 °C	P_4S_6	2%	3+
	Pyrrhotite ($Fe_{0.893}S$)	8%	n/a
	FeP_4	90%	2-; 3-

is responsible for the observed effect. In P_4S_6, sulfur acts as the anion while phosphorus adopts a 3+ oxidation state [131], which is incompatible with incorporation on the sulfur sites required for p-type doping [132]. In contrast, FeP_4 contains phosphorus in negative oxidation states and is therefore the more likely dopant source. Structurally, FeP_4 consists of Fe atoms octahedrally coordinated by six P atoms [133]. The phosphorus atoms form tetrahedral arrangements that include either two P atoms and two Fe atoms, or three P atoms and one Fe atom. These bonding configurations correspond to phosphorus oxidation states of 3- and 2-, supporting the hypothesis that FeP_4 provides the phosphorus anions necessary for successful doping.

The Fe+P precursor also includes FeP and Fe_2P phases, which host P in 3- and 2- charge, but in these compounds, phosphorus and iron are bound with double and triple bonds [134, 135]. The dissociation energies of these multinary bonds are up to 2 or 3 times higher than the Fe-P single bond. The synthesis conditions used do not enable breaking the higher-energy Fe-P multinary bonds, making the FeP_4 phase the only available compound for the p-type doping of pyrite microcrystals during the synthesis.

The proposed doping mechanism is based on the defect chemistry principles established by F. A. Kröger [128] and involves the substitution of sulfur atoms in the pyrite lattice by phosphorus ions. When FeP_4 is employed as the doping precursor, four phosphorus atoms are incorporated by replacing four sulfur atoms, while only a single iron atom is introduced into the lattice. This imbalance results in the formation of iron vacancies, which act as acceptor defects and contribute to p-type conductivity. Importantly, this doping process does not affect sulfur vacancies, which are neither filled nor eliminated by phosphorus incorporation. The concentration of sulfur vacancies is instead determined independently by the synthesis temperature and sulfur vapor pressure.

These initial results with the synthesis and doping of pyrite microcrystals demonstrate the potential of FeS_2 as a low-cost absorber material for terrestrial and extraterrestrial solar cells. Continued investigation is warranted to explore and enhance its performance in solar energy applications fully.

4 Conclusions

This thesis applies the monograin powder technology to synthesize and investigate pyrite FeS_2 microcrystals for their potential use as the absorber of the monograin layer solar cells. Based on the key findings, the main conclusions are summarized as follows:

- A synthesis procedure for growing pyrite microcrystals was developed, yielding crystals with suitable morphology and size for use as absorbers in monograin layer solar cells. All the used iodide fluxes, potassium iodide, lithium iodide, and cesium iodide, produced well-defined, individual microcrystals. Suitable synthesis-growth temperature was found at 690 °C.

  Pyrite microcrystals synthesized in the iodide salts exhibited uniform morphology with defined facets and smooth surfaces, and the cubic pyrite crystal structure, confirmed by XRD and Raman spectroscopy. Hot probe measurements indicated that synthesized FeS_2 crystals exhibit *n*-type conductivity.

  Elemental sulfur, when used as a flux, was found to be very difficult to remove without damaging the pyrite crystal surfaces.

- XPS analysis revealed that the pyrite crystals possess a surface layer, where Fe^{2+} states are oxidized to Fe^{3+} and S_2^{2-} dimers are cleaved into S^{2-} ions. These states, indicating a fractured surface layer, were not removed by etching the pyrite crystals with a mixture of H_2SO_4 and H_2O_2, or with a KCN solution.

- Different flux salts that were used in the synthesis-growth influence the impurity profile in the FeS_2 crystals, particularly by the incorporation of alkali metal impurities. Different impurity concentrations alter the energies of the valence band maximum and the position of the Fermi level in the synthesized materials, as evidenced by UPS measurements.

- Recrystallization of pyrite microcrystals in larger volumes of potassium iodide allowed partial removal of the copper impurity by dissolving Cu in the liquid flux. This purification relies on the distribution of impurities between solid FeS_2 and the molten KI flux. Increasing the amount of liquid flux enhances the dissolution of Cu into the KI, which is later removed. A similar behavior was found for intentional dopants; when phosphorus was added during the recrystallization step, it was preferentially removed, as it dissolved in the liquid KI flux.

- Phosphorus can be used to dope pyrite into *p*-type. To achieve this, a phosphorus source must first be synthesized with FeS and P, enabling the formation of FeP_4. This intermediate allows P^{3-} ions to substitute for sulfur in the pyrite lattice, leading to the creation of Fe vacancies, which are acceptor defects in pyrite. The phosphorus source must be added to the synthesis-growth of FeS_2 crystals. During post-synthesis treatments in the P vapor, phosphorus reacts with sulfur, which leads to the formation of secondary phases such as $FePS_3$.

- *P*-type pyrite microcrystals can be synthesized by introducing a phosphorus-containing precursor mixture so that phosphorus corresponds to 5 atomic% of the sulfur content. Such a high nominal concentration is required because phosphorus distributes between the solid and liquid phases, and only a fraction ultimately incorporates into the growing pyrite crystals. Adding more than 5 atomic% of the phosphorus mixture results in the formation of secondary phases.

- The first monograin layer heterojunction devices using pyrite absorbers were fabricated with nickel oxide as the junction partner. Although the devices demonstrated diode-like behavior, both efficiency and photocurrent were low. Nevertheless, these initial results highlight the feasibility of this approach and suggest that further optimization could enable functional pyrite-based solar cells.

References

[1] Gas, Coal and Power Markets Division of the International Energy Agency (IEA), "Electricity mid-year update 2025," tech. rep., International Energy Agency, 2025.

[2] Renewable Energy Division of the International Energy Agency (IEA), "Electricity 2025," tech. rep., International Energy Agency, 2025.

[3] Renewable Energy Division of the International Energy Agency (IEA), "Renewables 2025," tech. rep., International Energy Agency, 2025.

[4] S. L. Martinez, C. Connelly, M. Issokson, K. Fung, E. Pierce, A. Colombo, and J. Shangraw, "US solar: four things to look for in 2025," tech. rep., Wood Mackenzie, 2025.

[5] The IEA Photovoltaic Power Systems Programme, "Snapshot of Global PV Markets," tech. rep., International Energy Agency (IEA), 2025.

[6] S. Bhattacharya and S. John, "Beyond 30% conversion efficiency in silicon solar cells: A numerical demonstration," *Sci. Rep.*, vol. 9, p. 12482, Aug 2019.

[7] S. Fichtner, "Silicon prices surge as supply hits annual low," tech. rep., Solarbe Global, https://www.solarbeglobal.com/silicon-prices-surge-as-supply-hits-annual-low/, 2024.

[8] C. Wadia, A. P. Alivisatos, and D. M. Kammen, "Materials availability expands the opportunity for large-scale photovoltaics deployment," *Environmental Science Technology*, vol. 43, 3 2009.

[9] S. Gohri, J. Madan, M. K. A. Mohammed, and R. Pandey, "Inherent internal *p-n* junction assisted single layered *n*-type iron pyrite solar cell," *Materials Research Express*, vol. 10, p. 024001, 2 2023.

[10] M. Rahman, G. Boschloo, A. Hagfeldt, and T. Edvinsson, "On the mechanistic understanding of photovoltage loss in iron pyrite solar cells," *Advanced Materials*, vol. 32, 7 2020.

[11] European Space Agency, "Earth orbit, Moon, Mars: ESA's ambitious roadmap," 6 2022. https://www.esa.int/Science_Exploration/Human_and_Robotic_Exploration/ Earth_orbit_Moon_Mars_ESA_s_ambitious_roadmap.

[12] A. Ennaoui, S. Fiechter, C. Pettenkofer, N. Alonso-Vante, K. Büker, M. Bronold, C. Höpfner, and H. Tributsch, "Iron disulfide for solar energy conversion," *Solar Energy Materials and Solar Cells*, vol. 29, no. 4, pp. 289–370, 1993.

[13] A. Zaka, S. M. Alhassan, and A. Nayfeh, "Iron pyrite in photovoltaics: A review on recent trends and challenges," *ACS Applied Electronic Materials*, vol. 4, no. 9, pp. 4173–4211, 2022.

[14] B. Voigt, W. Moore, M. Manno, J. Walter, J. D. Jeremiason, E. S. Aydil, and C. Leighton, "Transport evidence for sulfur vacancies as the origin of unintentional *n*-type doping in pyrite FeS_2," *ACS Applied Materials Interfaces*, vol. 11, pp. 15552–15563, 5 2019.

[15] Y. N. Zhang, M. Law, and R. Q. Wu, "Atomistic modeling of sulfur vacancy diffusion near iron pyrite surfaces," *The Journal of Physical Chemistry C*, vol. 119, no. 44, pp. 24859–24864, 2015.

[16] D. Ray, B. Voigt, M. Manno, C. Leighton, E. S. Aydil, and L. Gagliardi, "Sulfur vacancy clustering and its impact on electronic properties in pyrite FeS_2," *Chemistry of Materials*, vol. 32, pp. 4820–4831, 6 2020.

[17] S. Fiechter, J. Mai, A. Ennaoui, and W. Szacki, "Chemical vapour transport of pyrite (FeS_2) with halogen (Cl, Br, I)," *Journal of Crystal Growth*, vol. 78, pp. 438–444, 12 1986.

[18] S. Khalid, M. A. Malik, D. J. Lewis, P. Kevin, E. Ahmed, Y. Khan, and P. O'Brien, "Transition metal doped pyrite (FeS_2) thin films: structural properties and evaluation of optical band gap energies," *Journal of Materials Chemistry C*, vol. 3, pp. 12068–12076, 2015.

[19] Z. Shi and A. H. Jayatissa, "Preparation and characterization of cobalt-doped iron pyrite (FeS_2) thin films," *Progress in Natural Science: Materials International*, vol. 30, pp. 352–359, 6 2020.

[20] Y. qiong Li, J. hua Chen, Y. Chen, and J. Guo, "Density functional theory study of influence of impurity on electronic properties and reactivity of pyrite," *Transactions of Nonferrous Metals Society of China*, vol. 21, pp. 1887–1895, 8 2011.

[21] B. Voigt, L. S. Valor, W. Moore, J. Jeremiason, J. Kakalios, E. S. Aydil, and C. Leighton, "Controlled *p*-type doping of pyrite FeS_2," *ACS Applied Materials Interfaces*, vol. 15, pp. 28258–28266, 6 2023.

[22] L. LONGi Green Energy Technology Co., "Longi claims world's highest efficiency for silicon solar cells," *pv-magazine.com*, Apr 2025.

[23] NREL, "Best research-cell efficiencies," tech. rep., National Renewable Energy Laboratory, 2025.

[24] K. Machkih, R. Oubaki, and M. Makha, "A Review of CIGS Thin Film Semiconductor Deposition via Sputtering and Thermal Evaporation for Solar Cell Applications," *Coatings*, vol. 14, no. 9, 2024.

[25] M. Barbato, E. Artegiani, M. Bertoncello, M. Meneghini, N. Trivellin, E. Mantoan, A. Romeo, G. Mura, L. Ortolani, E. Zanoni, and G. Meneghesso, "Cdte solar cells: technology, operation and reliability," *Journal of Physics D: Applied Physics*, vol. 54, p. 333002, jun 2021.

[26] J. Hardy, H. Fiedler, and J. Kennedy, "A review on the current status and chemistry of tin halide perovskite films for photovoltaics," *Progress in Materials Science*, vol. 151, p. 101446, 2025.

[27] A. Aierken, M. Li, S. Hamzawy, J. Bi, S. Zhang, T. Wang, X. Liu, and T. Ma, "A study on the radiation effects on flexible GaInP/GaAs/InGaAs triple-junction solar cells using photoluminescence measurements," *Phys. Scr.*, vol. 100, no. 4, p. 045908, 2025.

[28] Q. Meng, "The pathway to >15

[29] K. Li, R. Tang, C. Zhu, and T. Chen, "Critical review on crystal orientation engineering of antimony chalcogenide thin film for solar cell applications," *Advanced Science*, vol. 11, no. 2, p. 2304963, 2024.

[30] X. Chen, B. Che, Y. Zhao, S. Wang, H. Li, J. Gong, G. Chen, T. Chen, X. Xiao, and J. Li, "Solvent-assisted hydrothermal deposition approach for highly-efficient sb2(s,se)3 thin-film solar cells," *Advanced Energy Materials*, vol. 13, no. 21, p. 2300391, 2023.

[31] H. Hu, Z. Jin, J. Ge, C. Shen, L. Xie, W. Song, Q. Ye, P. Ding, J. Li, C. Han, X. Yu, Q. Liu, and Z. Ge, "17.68% efficiency nonhalogenated solvent-processed organic solar cell modules driven by seed crystal strategy," *Advanced Materials*, vol. 37, no. 14, p. 2420308, 2025.

[32] Q. Wu, R. Gao, Q. Wang, C. Yuan, C. Lin, Q. Yang, H. Tang, J. Yao, X. Zuo, and G. Li, "High-efficiency dye-sensitized solar cell based on carbon nanotubes-modified molybdenum nitride nanoparticles counter electrode," *Solar Energy*, vol. 291, p. 113394, 2025.

[33] M. Z. Rahman and T. Edvinsson, "What is limiting pyrite solar cell performance?," *Joule*, vol. 3, pp. 2290–2293, 10 2019.

[34] S. Lehner, K. Savage, and J. Ayers, "Vapor growth and characterization of pyrite (FeS_2) doped with Co, Ni, and As: Variations in semiconducting properties," *Journal of Crystal Growth*, vol. 286, 1 2006.

[35] A. Zaka, S. Alhassan, and A. Nayfeh, "Understanding the phase changes and optical properties in the solvothermal synthesis of iron pyrite," *Sci. Rep.*, vol. 15, p. 18763, may 2025.

[36] H. Qin, J. Jia, L. Lin, H. Ni, M. Wang, and L. Meng, "Pyrite FeS_2 nanostructures: Synthesis, properties and applications," *Materials Science and Engineering: B*, vol. 236-237, pp. 104–124, 2018.

[37] ASM International Alloy Phase Diagram and Handbook Committees, *Alloy phase Diagrams*, p. 854. The Materials Information Society, 1992.

[38] M. S. Schmøkel, L. Bjerg, S. Cenedese, M. R. V. Jørgensen, Y.-S. Chen, J. Overgaard, and B. B. Iversen, "Atomic properties and chemical bonding in the pyrite and marcasite polymorphs of FeS_2: a combined experimental and theoretical electron density study," *Chem. Sci.*, vol. 5, pp. 1408–1421, 2014.

[39] Data retrieved from the Materials Project for FeS_2 (mp-226) from database version v2025.09.25. https://next-gen.materialsproject.org/materials/mp-226, Accessed: 11.11.2025.

[40] M. Cabán-Acevedo, N. S. Kaiser, C. R. English, D. Liang, B. J. Thompson, H.-E. Chen, K. J. Czech, J. C. Wright, R. J. Hamers, and S. Jin, "Ionization of high-density deep donor defect states explains the low photovoltage of iron pyrite single crystals," *Journal of the American Chemical Society*, vol. 136, pp. 17163–17179, 12 2014.

[41] B. Voigt, W. Moore, M. Maiti, J. Walter, B. Das, M. Manno, C. Leighton, and E. S. Aydil, "Observation of an internal *p–n* junction in pyrite FeS_2 single crystals: Potential origin of the low open circuit voltage in pyrite solar cells," *ACS Materials Letters*, vol. 2, pp. 861–868, 7 2020.

[42] M. Limpinsel, N. Farhi, N. Berry, J. Lindemuth, C. L. Perkins, Q. Lin, and M. Law, "An inversion layer at the surface of *n*-type iron pyrite," *Energy Environmental Science*, vol. 7, 2014.

[43] S. Uchiyama, Y. Ishikawa, and Y. Uraoka, "Effect of inversion layer at iron pyrite surface on photovoltaic device," *Japanese Journal of Applied Physics*, vol. 57, p. 032301, 3 2018.

[44] D. Liang, M. Cabán-Acevedo, N. S. Kaiser, and S. Jin, "Gated hall effect of nanoplate devices reveals surface-state-induced surface inversion in iron pyrite semiconductor," *Nano Letters*, vol. 14, no. 12, pp. 6754–6760, 2014.

[45] F. Herbert, A. Krishnamoorthy, K. V. Vliet, and B. Yildiz, "Quantification of electronic band gap and surface states on FeS_2 (100)," *Surface Science*, vol. 618, pp. 53–61, 12 2013.

[46] H. W. Nesbitt, G. M. Bancroft, A. R. Pratt, and M. J. Scaini, "Sulfur and iron surface states on fractured pyrite surfaces," *American Mineralogist*, vol. 83, pp. 1067–1076, 10 1998.

[47] E. Zuñiga-Puelles, R. Cardoso-Gil, M. Bobnar, I. Veremchuk, G. Heide, and R. Gumeniuk, "Electrical and thermal transport properties of natural and synthetic $FeAs_xS_{2-x}$ ($x \leq 0.01$)," *Journal of Physics and Chemistry of Solids*, vol. 150, p. 109809, 2021.

[48] T.-L. Liu and J.-M. Zhang, "Feasibility of band gap engineering of iron pyrite (FeS_2) by codoping Os, Ru or Zn together with O," *Materials Chemistry and Physics*, vol. 244, p. 122742, 2020.

[49] J.-Y. Zhao and J.-M. Zhang, "Modulating the Band Gap of the FeS_2 by O and Se Doping," *The Journal of Physical Chemistry C*, vol. 121, no. 35, pp. 19334–19340, 2017.

[50] S. W. Lehner, N. Newman, M. van Schilfgaarde, S. Bandyopadhyay, K. Savage, and P. R. Buseck, "Defect energy levels and electronic behavior of Ni-, Co-, and As-doped synthetic pyrite (FeS_2)," *Journal of Applied Physics*, vol. 111, 4 2012.

[51] T. Salk, "The Effect of Co, Ni, and Cr Impurities on the Electronic Properties of Iron Pyrite," Master's thesis, University of California, 2019.

[52] B. Voigt, B. Das, D. M. Carr, D. Ray, M. Maiti, W. Moore, M. Manno, J. Walter, E. S. Aydil, and C. Leighton, "Mitigation of the internal *p-n* junction in CoS_2-contacted FeS_2 single crystals: Accessing bulk semiconducting transport," *Physical Review Materials*, vol. 5, p. 025405, 2 2021.

[53] X. Zhang, M. Li, J. Walter, L. O'Brien, M. A. Manno, B. Voigt, F. Mork, S. V. Baryshev, J. Kakalios, E. S. Aydil, and C. Leighton, "Potential resolution to the doping puzzle in iron pyrite: Carrier type determination by hall effect and thermopower," *Physical Review Materials*, vol. 1, 6 2017.

[54] R. P. Srivastava, A. P. Saxena, and S. Ingole, "*N*-type iron pyrite (FeS_2) thin-films obtained at different sulfur vapor pressures," *Chalcogenide Letters*, vol. 14, pp. 227–237, 2017.

[55] P. Prabukanthan, S. Thamaraiselvi, and G. Harichandran, "Single step electrochemical deposition of p-type undoped and Co^{2+} doped FeS_2 thin films and performance in heterojunction solid solar cells," *Journal of The Electrochemical Society*, vol. 164, p. D581, jul 2017.

[56] M. Law, "Pyrite iron sulfide solar cells made from solution," tech. rep., University of California, 2017.

[57] M. Limpinsel, *Iron Pyrite Absorbers for Solar Photovoltaic Energy Conversion*. PhD thesis, University of California, 2015.

[58] J. Hu, Y. Zhang, M. Law, and R. Wu, "Increasing the band gap of iron pyrite by alloying with oxygen," *Journal of the American Chemical Society*, vol. 134, no. 32, pp. 13216–13219, 2012.

[59] L. Luo, W. Luan, B. Yuan, C. Zhang, and L. Jin, "High Efficient and Stable Solid Solar Cell: Based on FeS_2 Nanocrystals and P3HT: PCBM," *Energy Procedia*, vol. 75, 8 2015.

[60] Y.-Y. Lin, D.-Y. Wang, H.-C. Yen, H.-L. Chen, C.-C. Chen, C.-M. Chen, C.-Y. Tang, and C.-W. Chen, "Extended red light harvesting in a poly(3-hexylthiophene)/iron disulfide nanocrystal hybrid solar cell," *Nanotechnology*, vol. 20, p. 405207, sep 2009.

[61] A. Kirkeminde, R. Scott, and S. Ren, "All inorganic iron pyrite nano-heterojunction solar cells," *Nanoscale*, vol. 4, pp. 7649–7654, 2012.

[62] M. Alam Khan and Y.-M. Kang, "Synthesis and processing of strong light absorbent iron pyrite quantum dots in polymer matrix for efficiency enhancement of bulk-heterojunction solar cell," *Materials Letters*, vol. 132, pp. 273–276, 2014.

[63] S. Middya, A. Layek, A. Dey, and P. P. Ray, "Synthesis of nanocrystalline FeS_2 with increased band gap for solar energy harvesting," *Journal of Materials Science Technology*, vol. 30, no. 8, pp. 770–775, 2014.

[64] B. J. Richardson, L. Zhu, and Q. Yu, "Inverted hybrid solar cells based on pyrite FeS_2 nanocrystals in P3HT:PCBM with enhanced photocurrent and air-stability," *Solar Energy Materials and Solar Cells*, vol. 116, pp. 252–261, 2013.

[65] M. Kauk-Kuusik, K. Timmo, M. Pilvet, K. Muska, M. Danilson, J. Krustok, R. Josepson, V. Mikli, and M. Grossberg-Kuusk, "Cu_2ZnSnS_4 monograin layer solar cells for flexible photovoltaic applications," *J. Mater. Chem. A*, vol. 11, pp. 23640–23652, 2023.

[66] D. Meissner, K. Ernits, S. Gahr, L. Kapitan, M. Vetter, C. Glatz, and R. Syed, "Kesterite based monograin photovoltaics: The ideal solution for sustainable power supply," *Solar Energy Materials and Solar Cells*, vol. 252, p. 112160, 2023.

[67] K. Timmo, M. D. Sadurni, M. Pilvet, K. Muska, M. Altosaar, V. Mikli, F. Atlan, M. Guc, V. Izquierdo-Roca, M. Grossberg-Kuusk, and M. Kauk-Kuusik, "Efficiency enhancement of Cu_2ZnSnS_4 monograin layer solar cells via absorber post-growth treatments," *Solar Energy Materials and Solar Cells*, vol. 250, p. 112090, 2023.

[68] K. Timmo, M. Pilvet, K. Muska, M. Altosaar, V. Mikli, R. Kaupmees, R. Josepson, J. Krustok, M. Grossberg-Kuusk, and M. Kauk-Kuusik, "Influence of alkali iodide fluxes on Cu_2ZnSnS_4 monograin powder properties and performance of solar cells," *Mater. Adv.*, vol. 4, pp. 4509–4519, 2023.

[69] P. W. Voorhees, "Ostwald ripening of two-phase mixtures," *Annual Review of Materials Research*, vol. 22, pp. 197–215, 1992.

[70] X. Li, K. Timmo, M. Grossberg, M. Pilvet, R. Kaupmees, J. Krustok, K. Muska, V. Mikli, and M. Kauk-Kuusik, "Study of the structure and optoelectronic properties of $Cu_2Ge(Se_xS_{1-x})_3$ microcrystalline powders," *Thin Solid Films*, vol. 742, p. 139053, 2022.

[71] F. Ghisani, K. Timmo, M. Altosaar, V. Mikli, M. Pilvet, R. Kaupmees, J. Krustok, M. Grossberg, and M. Kauk-Kuusik, "Characterization of tetrahedrite $Cu_{10}Cd_2Sb_4S_{13}$ monograin materials grown in molten CdI_2 and LiI," *Thin Solid Films*, vol. 739, p. 138980, 12 2021.

[72] M. Kauk-Kuusik, X. Li, M. Pilvet, K. Timmo, M. Grossberg, T. Raadik, M. Danilson, V. Mikli, M. Altosaar, J. Krustok, and J. Raudoja, "Study of $Cu_2CdGeSe_4$ monograin powders synthesized by molten salt method for photovoltaic applications," *Thin Solid Films*, vol. 666, pp. 15–19, 11 2018.

[73] E. Mellikov, D. Meissner, T. Varema, M. Altosaar, M. Kauk, O. Volobujeva, J. Raudoja, K. Timmo, and M. Danilson, "Monograin materials for solar cells," *Solar Energy Materials and Solar Cells*, vol. 93, 1 2009.

[74] T. Salk, *Iron Pyrite Single Crystal Studies*. PhD thesis, University of California, 2019.

[75] J. Sangster and A. D. Pelton, "The Na-S (sodium-sulfur) system equilibrium diagram," *Journal of Phase Equilibria*, vol. 18, p. 89, 1997.

[76] S. Uchiyama, R. Sato, R. Katsube, M. M. Islam, H. Adachi, T. Sakurai, Y. Nose, and Y. Ishikawa, "Optical and electrical transport evaluations of *n*-type iron pyrite single crystals," *ACS Omega*, vol. 6, pp. 31358–31365, 11 2021.

[77] A. Zavrazhnov, A. Naumov, A. Kosyakov, S. Berezin, V. Volkov, and A. Sergeeva, "The iron sulfides crystal growth from the halide melts," *Mater. Res.*, vol. 21, may 2018.

[78] M. Kauk, M. Altosaar, J. Raudoja, K. Timmo, M. Grossberg, T. Varema, and E. Mellikov, "Growth of $CuInSe_2$ monograin powders with different compositions," *MRS Proceedings*, vol. 865, p. F14.28, 2005.

[79] M. Kauk, M. Altosaar, J. Raudoja, K. Timmo, T. Varema, M. Danilson, M. Grossberg, and E. Mellikov, "The influence of doping with donor type impurities on the properties of $CuInSe_2$," *Phys. Status Solidi C*, vol. 5, pp. 609–611, Feb 2008.

[80] Y. Iwadate and T. Ohkubo, "Densities and refractive indices of molten alkali iodides: Estimation of electronic polarizability of an iodide ion," *Journal of Chemical Engineering Data*, vol. 65, pp. 5240–5248, 11 2020.

[81] NASA, "Artemis," 2024. https://www.nasa.gov/humans-in-space/artemis/.

[82] European Space Agency, Pierre Carril, "Artist impression of a moon base concept.," 2025. https://www.esa.int/Enabling_Support/Preparing_for_the_Future/Space_for_Earth/Supporting_Sustainable_Development.

[83] A. McEwen and M. Robinson, "Mapping of the Moon by Clementine," *Advances in Space Research*, vol. 19, pp. 1523–1533, 1 1997.

[84] S. Li, P. G. Lucey, R. E. Milliken, P. O. Hayne, E. Fisher, J.-P. Williams, D. M. Hurley, and R. C. Elphic, "Direct evidence of surface exposed water ice in the lunar polar regions," *Proceedings of the National Academy of Sciences*, vol. 115, no. 36, pp. 8907–8912, 2018.

[85] M. Azami, Z. Kazemi, S. Moazen, M. Dubé, M.-J. Potvin, and K. Skonieczny, "A comprehensive review of lunar-based manufacturing and construction," *Astrophysics > Instrumentation and Methods for Astrophysics*, 2024.

[86] D. E. Wilhelms, "Lunar stratigraphy and sedimentology," *Icarus*, vol. 32, pp. 471–472, 12 1977.

[87] J. M. Day, E. M. van Kooten, B. A. Hofmann, and F. Moynier, "Mare basalt meteorites, magnesian-suite rocks and kreep reveal loss of zinc during and after lunar formation," *Earth and Planetary Science Letters*, vol. 531, p. 115998, 2 2020.

[88] M. D. Sabatino, R. Hendawi, and A. S. Garcia, "Silicon Solar Cells: Trends, Manufacturing Challenges, and AI Perspectives," *Crystals*, vol. 14, p. 167, 2 2024.

[89] B. Liang, X. Chen, X. Wang, H. Yuan, A. Sun, Z. Wang, L. Hu, G. Hou, Y. Zhao, and X. Zhang, "Progress in crystalline silicon heterojunction solar cells," *J. Mater. Chem. A*, vol. 13, pp. 2441–2477, 2025.

[90] C.-Y. Tsai, "Absorption coefficients of silicon: A theoretical treatment," *Journal of Applied Physics*, vol. 123, p. 183103, 05 2018.

[91] P. G. Lucey, G. J. Taylor, and E. Malaret, "Abundance and distribution of iron on the moon," *Science*, vol. 268, no. 5214, pp. 1150–1153, 1995.

[92] C. Yang, X. Zhang, L. Bruzzone, B. Liu, D. Liu, X. Ren, J. A. Benediktsson, Y. Liang, B. Yang, M. Yin, H. Zhao, R. Guan, C. Li, and Z. Ouyang, "Comprehensive mapping of lunar surface chemistry by adding chang'e-5 samples with deep learning," *Nat. Commun.*, vol. 14, p. 7554, nov 2023.

[93] Z. Wang, Y. Li, W. Zhang, Q. He, F. Pan, Z. Hu, K. Zong, Y. Feng, H. Becker, J. M. Day, W. Song, H. Hui, F. Moynier, Y. Jiang, X. Zhang, Z. She, X. Wu, L. Xiao, and L. Wang, "Sulfide compositions of young chang'e-5 basalts and implications for sulfur isotopes in lunar basalt sources," *Geochimica et Cosmochimica Acta*, vol. 368, pp. 168–184, 2024.

[94] L. A. Taylor and K. L. Williams, "Cu-Fe-S Phases in Lunar Rocks," *American Mineralogist*, vol. 58, pp. 952–954, 1973.

[95] A. E. Saal and E. H. Hauri, "Large sulfur isotope fractionation in lunar volcanic glasses reveals the magmatic differentiation and degassing of the Moon," 2021.

[96] S. Kubitza, S. Schröder, E. Dietz, S. Frohmann, P. B. Hansen, K. Rammelkamp, D. S. Vogt, M. Gensch, and H.-W. Hübers, "Detecting sulfur on the moon: The potential of vacuum ultraviolet laser-induced breakdown spectroscopy," *Spectrochimica Acta Part B: Atomic Spectroscopy*, vol. 174, p. 105990, 2020.

[97] D. Vaniman, D. Pettit, and G. Heiken, "Uses of lunar sulfur," *2nd Conference on Lunar Bases and Space Activities*, pp. 429–435, 1992.

[98] D. C. Rubie, C. K. Gessmann, and D. J. Frost, "Partitioning of oxygen during core formation on the earth and mars," *Nature*, vol. 429, pp. 58–61, May 2004.

[99] A. Ennaoui and H. Tributsch, "Iron sulphide solar cells," *Solar Cells*, vol. 13, pp. 197–200, 1984.

[100] A. Ennaoui, S. Fiechter, W. Jaegermann, and H. Tributsch, "Photoelectrochemistry of highly quantum efficient single-crystalline n-FeS$_2$ (pyrite)," *Journal of The Electrochemical Society*, vol. 133, p. 97, jan 1986.

[101] ScholAR Chemistry, "Material safety data sheet potassium iodide," 2008.

[102] X. Yuan and H. Zheng, "*In-situ* Raman spectroscopic studies of FeS$_2$ pyrite up to 675 K and 2100 MPa using a hydrothermal diamond anvil cell," *Mineralogical Magazine*, vol. 79, 2 2015.

[103] A. N. Utyuzh, "Influence of temperature on raman spectra of the FeS$_2$ single crystal with pyrite structure," *Physics of the Solid State*, vol. 56, pp. 2050–2055, 10 2014.

[104] A. K. Kleppe and A. P. Jephcoat, "High-pressure raman spectroscopic studies of FeS$_2$ pyrite," *Mineralogical Magazine*, vol. 68, no. 3, p. 433–441, 2004.

[105] Z. Mutlu, B. Debnath, S. Su, C. Li, M. Ozkan, K. N. Bozhilov, R. K. Lake, and C. S. Ozkan, "Chemical vapor deposition and phase stability of pyrite on SiO$_2$," *Journal of Materials Chemistry C*, vol. 6, pp. 4753–4759, 2018.

[106] M. Grossberg, J. Krustok, J. Raudoja, K. Timmo, M. Altosaar, and T. Raadik, "Photoluminescence and Raman study of Cu$_2$ZnSn(Se$_x$S$_{1x}$)$_4$ monograins for photovoltaic applications," *Thin Solid Films*, vol. 519, no. 21, pp. 7403–7406, 2011.

[107] H. Ning, Z. Liu, Y. Xie, and H. Huang, "CoS$_2$ coatings for improving thermal stability and electrochemical performance of FeS$_2$ cathodes for thermal batteries," *Journal of The Electrochemical Society*, vol. 165, p. A1725, jun 2018.

[108] T. Sato, Y. Fukasawa, and M. Yamamura, "Viscosities of molten alkali-metal bromides and iodides," *International Journal of Thermophysics,*, vol. 18, 1997.

[109] R. Steudel, "Liquid sulfur," *Topics in Current Chemistry*, vol. 230, 2003.

[110] A. P. Grosvenor, B. A. Kobe, M. C. Biesinger, and N. S. McIntyre, "Investigation of multiplet splitting of Fe 2p XPS spectra and bonding in iron compounds," *Surf. Interface Anal.*, vol. 36, pp. 1564–1574, dec 2004.

[111] C. M. Eggleston, J.-J. Ehrhardt, and W. Stumm, "Surface structural controls on pyrite oxidation kinetics; an XPS-UPS, STM, and modeling study," *American Mineralogist*, vol. 81, pp. 1036–1056, 10 1996.

[112] M. Fantauzzi, B. Elsener, D. Atzei, A. Rigoldi, and A. Rossi, "Exploiting XPS for the identification of sulfides and polysulfides," *RSC Adv.*, vol. 5, pp. 75953–75963, 2015.

[113] P. Behra, P. Bonnissel-Gissinger, M. Alnot, R. Revel, and J. J. Ehrhardt, "XPS and XAS Study of the Sorption of Hg(II) onto Pyrite," *Langmuir*, vol. 17, no. 13, pp. 3970–3979, 2001.

[114] J. Kim, G. Y. Kim, H. Moon, S. Yoon, I. W. Seo, Y. Lee, D. G. Moon, S. Ahn, and W. Jo, "Identification of marcasite in pyrite fes2 thin films and the films' carrier transport characteristics," *RSC Adv.*, vol. 6, pp. 81394–81399, 2016.

[115] Y. Nie, Q. Wang, F. Zi, X. Hu, Y. Chen, L. Guo, and H. Yu, "The catalytic decomposition of thiosulfate by pyrite," *Applied Surface Science*, vol. 436, pp. 217–223, 2018.

[116] M. Berg, H. P. Hjalmarson, D. Scrymgeour, M. T. Brumbach, P. A. Schultz, P. G. Clem, M. M. Hopkins, C. H. Moore, T. Ohta, S. Smith, and E. Bussmann, "Work function of pt thin films with disorder," *APS March Meeting*, 2018.

[117] W. M. Sachtler, G. J. Dorgelo, and A. A. Holscher, "The work function of gold," *Surface Science*, vol. 5, pp. 221–229, 10 1966.

[118] Y. Akaltun and T. Çayır, "Fabrication and characterization of NiO thin films prepared by SILAR method," *Journal of Alloys and Compounds*, vol. 625, 3 2015.

[119] K. S. Savage, D. Stefan, and S. W. Lehner, "Impurities and heterogeneity in pyrite: Influences on electrical properties and oxidation products," *Applied Geochemistry*, vol. 23, pp. 103–120, 2 2008.

[120] G. Willeke, O. Blenk, C. Kloc, and E. Bucher, "Preparation and electrical transport properties of pyrite (FeS_2) single crystals," *Journal of Alloys and Compounds*, vol. 178, 2 1992.

[121] S. Ghosh, T. Avellini, A. Petrelli, I. Kriegel, R. Gaspari, G. Almeida, G. Bertoni, A. Cavalli, F. Scotognella, T. Pellegrino, and L. Manna, "Colloidal $CuFeS_2$ nanocrystals: Intermediate Fe d-band leads to high photothermal conversion efficiency," *Chemistry of Materials*, vol. 28, pp. 4848–4858, 7 2016.

[122] J. E. Whitten, "Ultraviolet photoelectron spectroscopy: Practical aspects and best practices," *Applied Surface Science Advances*, vol. 13, p. 100384, 2 2023.

[123] C. Tresca, G. Giovannetti, M. Capone, and G. Profeta, "Electronic properties of superconducting FeS," *Physical Review B*, vol. 95, p. 205117, 5 2017.

[124] J. D. Myers, J. A. Frantz, C. C. Baker, S. C. Erwin, S. N. Qadri, N. Bassim, S. B. Qadri, R. Y. Bekele, and J. S. Sanghera, "Reduction in surface state defects in iron pyrite by use of zinc sulfide passivation layers," *Optical Materials Express*, vol. 8, 12 2018.

[125] M. Grossberg, T. Raadik, J. Raudoja, and J. Krustok, "Photoluminescence study of defect clusters in Cu_2ZnSnS_4 polycrystals," *Current Applied Physics*, vol. 14, pp. 447–450, 3 2014.

[126] Y. Zhang, H. Li, H. Wang, R. Liu, S.-L. Zhang, and Z.-J. Qiu, "On valence-band splitting in layered MoS_2," *ACS Nano*, vol. 9, no. 8, pp. 8514–8519, 2015.

[127] C. C. Mayorga-Martinez, Z. Sofer, D. Sedmidubský, Huber, A. Y. S. Eng, and M. Pumera, "Layered metal thiophosphite materials: Magnetic, electrochemical, and electronic properties," *ACS Applied Materials & Interfaces*, vol. 9, no. 14, pp. 12563–12573, 2017.

[128] F. A. Kröger, *The Chemistry of Imperfect Crystals*. American Elsevier Publishing Company, 1964.

[129] H. Wang, R. Su, Y. Liu, Y. Kong, Z. Ren, and B. Jiang, "Iron-group metal compound electrocatalysts for efficient hydrogen production: Recent advances and future prospects," *ChemCatChem*, vol. 16, no. 8, p. e202301241, 2024.

[130] G. R. Gonçalves, M. A. Schettino, Jr, C. S. Schettino, V. Piccoli, H. C. de Jesus, M. A. Vieira, A. G. Cunha, and J. C. C. Freitas, "Synthesis of iron phosphide nanoparticles dispersed in activated carbon and their application in fenton processes," *J. Nanopart. Res.*, vol. 24, oct 2022.

[131] T. Rödl and A. Pfitzner, "The crystal and molecular structure of γ-P_4S_6," *Zeitschrift für anorganische und allgemeine Chemie*, vol. 637, no. 11, pp. 1507–1510, 2011.

[132] A. Zunger, "Practical doping principles," *Applied Physics Letters*, vol. 83, pp. 57–59, 07 2003.

[133] M. Sugitani, N. Kinomura, M. Koizumi, and S. Kume, "Preparation and properties of a new iron phosphide FeP_4," *Journal of Solid State Chemistry*, vol. 26, no. 2, pp. 195–201, 1978.

[134] PubChem, "Diiron monosulphide," tech. rep., National Library of Medicine, 2025.

[135] PubChem, "Iron monosulphide," tech. rep., National Library of Medicine, 2025.

Acknowledgements

I would like to express my sincere gratitude to my supervisors, Dr. Taavi Raadik, Dr. Mare Altosaar, and Dr. Advenit Makaya, for giving me the opportunity to embark on this journey. I have learned so much from you throughout the years, not only about research but also about leadership, empathy, and dedication.

I am thankful to all my co-authors for working with me, helping me carry out experiments, and reaching the finish line.

A sincere thank you to Prof. Maarja Grossberg-Kuusk, Head of the Department of Materials and Environmental Technology, for her encouragement and belief in me. Your example is a source of inspiration.

I am grateful to the entire Laboratory of Photovoltaic Materials Research. Special thank you to Prof. Marit Kauk-Kuusik for her leadership and to all the members of the lab for creating such a supportive and motivating environment.

Thank you to all the PhD students in our laboratory over the years. You have made this experience fun and so enjoyable.

Abstract

Synthesis and characterization of pyrite FeS_2 microcrystals for photovoltaic applications

Solar energy is the most abundant of all sustainable energy sources and remains a key technology in the global transition to renewable power. Silicon-based solar cells dominate the market of photovoltaic devices, but research has focused on identifying low-cost, non-toxic alternatives to conventional materials. One such material is pyrite FeS_2, which is considered due to its low cost, suitable optical band gap of 0.95 eV, a high absorption coefficient of $\alpha > 10^5$ cm^{-1} for h$\nu > 1.3$ eV, and a 100-1000 nm minority carrier diffusion length, suitable for photovoltaic applications. Despite a theoretical efficiency of 25%, practical devices have yet to prove it. Pyrite devices suffer from the inverse surface layer where the bulk of FeS_2 is typically *n*-type, as the surface forms a thin *p*-type layer, resulting in a narrow internal junction that complicates the formation of a *p/n* junction in pyrite devices. While most research has focused on thin film configurations, where the inverse surface dominates, an alternative and potentially more effective approach is to use pyrite in the form of crystals. In crystalline form, surface-related effects are less dominant, and the crystals may be used in the absorber of monograin layer (MGL) solar cells. This technology has not been explored for pyrite before.

Pyrite-based solar cells are also being considered for space applications, particularly in the context of lunar energy production. The low synthesis temperature of pyrite and the simplicity of the MGL technology make this system especially attractive for *in-situ* fabrication on the Moon. The permanent lunar settlements are currently being planned in collaboration with NASA and the European Space Agency.

In this study, pyrite microcrystals were synthesized using the molten salt synthesis-growth method. It was found that elemental sulfur is not an appropriate flux medium, as the post-synthesis removal of sulfur by sublimation and chemical etching negatively affects the crystal composition and surface quality, as confirmed by Raman spectroscopy and X-ray Photoelectron Spectroscopy (XPS). In contrast, using potassium iodide (KI) as the flux medium resulted in the formation of individually formed pyrite crystals with uniform composition. Raman spectroscopy identified characteristic peaks at 343, 350, 379, and 430 cm^{-1}, all corresponding to the pyrite phase. X-ray Diffraction (XRD) analysis confirmed phase purity; the calculated lattice parameter for the crystals was a = b = c = 5.4154 Å, consistent with the cubic symmetry of pyrite.

XPS analysis revealed the surface fracture of pyrite. The surface Fe^{2+} ions were found to be largely oxidized to Fe^{3+}, and the characteristic S_2^{2-} dimers had dissociated into individual S^{2-} ions. These surface defects introduce additional electronic states within the band gap, leading to *p*-type conductivity at the surface, in contrast to the *n*-type behavior of the bulk. Chemical etching with a $H_2SO_4 + H_2O_2$ mixture did not significantly mitigate these surface defects. Sublimation treatment, on the other hand, resulted in the complete removal of sulfur from the pyrite surface. Subsequent etching with a potassium cyanide solution restored sulfur signals in the XPS spectra, suggesting partial reconstitution of the surface composition.

To evaluate the effect of different flux media on crystal growth and impurity incorporation, a range of flux salts was tested. Pyrite microcrystals synthesized using KI, lithium iodide (LiI), and cesium iodide (CsI) exhibited similar morphology, while using sodium polysulfide (Na_2S_x) or no flux at all resulted in the formation of very small crystallites that had not yet formed as individual microcrystals. Surprisingly, Raman spectroscopy and XRD detected only the high-quality pyrite phase across all

samples. However, mass spectrometry revealed significant levels of elemental impurities, particularly transition metals such as Cr, Cu, Co, and Ni, with concentrations ranging from 10^{17} to 10^{18} atoms cm^{-3}. The highest lithium content was observed in pyrite synthesized with LiI, reaching 10^{19} atoms cm^{-3}. In the material synthesized in CsI, cesium levels also reached 10^{19} atoms cm^{-3}, and unexpectedly, elevated Cs concentrations (up to 5×10^{17} atoms cm^{-3}) were also found in crystals grown with LiI. This was traced back to cesium contamination in the LiI salt, indicating that LiI is not an ideal flux medium due to its impurity profile. It was further observed that recrystallizing pyrite in a larger volume of KI significantly reduced copper impurity levels, enabling the synthesis of higher-purity pyrite crystals.

Ultraviolet photoelectron spectroscopy (UPS) analysis revealed that the pyrite materials with different impurity profiles have strongly different electronic band structures. The UPS data also confirmed the *n*-type conductivity of the crystals, as the Fermi level was found to be positioned close to the expected conduction band minimum. It was also found that the samples synthesized in different flux media, containing varying levels and types of impurities, exhibited photoluminescence (PL) emission bands at different energies, indicating that impurity incorporation strongly influences the recombination pathways. A more detailed PL analysis is required to understand the defect composition in pyrite better.

Given that the flux growth process enables the incorporation of impurities, the next step was to explore intentional doping of pyrite to achieve uniform *p*-type conductivity. Phosphorus (P) was selected as the dopant. Successful doping was determined to require the incorporation of phosphorus during pyrite synthesis, as post-synthesis or recrystallization doping attempts were ineffective due to various limitations. Phosphorus was successfully introduced only as an anion. Therefore, it was first reacted with iron sulfide to form FeP_4, which was then added to the precursors of pyrite synthesis. Doping with 5 at% P per sulfur in FeS_2 resulted in *p*-type pyrite crystals with no changes in the morphology and high-quality pyrite phase composition, as confirmed by Raman spectroscopy and XRD.

For the first time, monograin layer solar cells were fabricated using pyrite microcrystals as the absorber material in combination with a nickel oxide buffer layer. While the initial devices exhibited negligible photocurrent, the observed diode-like behavior confirms the formation of a heterojunction. These results indicate that with further optimization, pyrite-based solar cells may become a viable alternative for low-cost, sustainable photovoltaic technologies on Earth and beyond.

Kokkuvõte

Püriitsete FeS$_2$ mikrokristallide süntees ja iseloomustamine päikesepatareides kasutamiseks

Päikeseenergia on kõigist jätkusuutlikest energiaallikatest kõige laialdasemalt saadaval ning on võtmetehnoloogia ülemaailmse taastuvenergiale ülemineku juures. Ränipõhised päikesepaneelid moodustavad suure enamuse päikesepaneelide turust, kuid teadusuuringud keskenduvad aina rohkem soodsate ja mittetoksiliste materjalide leidmisele, mida päikeseenergia rakendustes kasutada. Üks selline materjal on püriit FeS$_2$, mida iseloomustab väga soodne hind, sobiv optiline keelutsoon 0,95 eV, kõrge neeldumiskordaja ($\alpha > 10^5$ cm^{-1} kui hν > 1.3 eV) ning 100–1000 nm pikkune vähemuskandjate difusioonitee, mis sobib suurepäraselt päikeseenergia rakendusteks. Vaatamata teoreetilisele efektiivsusele kuni 25% ei ole püriidipõhised seadmed seda praktikas veel saavutanud. Püriidi kasutamist takistab nn. pöördpinna efekt: kuigi püriidi kristallid on sisemuses tavaliselt *n*-tüüpi, tekib pinna lähedale õhuke *p*-tüüpi kiht, mis moodustab kitsa sisemise ülemineku ja muudab toimiva *p-n*-siirde loomise keeruliseks. Enamik teadusrühmasid on keskendunud püriidi õhukestele kiledele, kus domineerib pöördpind, kuid alternatiivne ja potentsiaalselt tõhusam lähenemine on kasutada püriiti kristallidena. Kristalsetes materjalides on pinna mõju proportsionaalselt väiksem ning kristalle saab kasutada monoterakiht(MGL)-päikesepatareide valgust neelavas kihis. Seda tehnoloogiat pole püriidi puhul varem uuritud.

Püriidipõhiseid päikesepatareisid kaalutakse ka kosmoserakendustes, eriti Kuul energia tootmise kontekstis. Püriidi madal sünteesitemperatuur ja MGL-tehnoloogia lihtsus muudavad selle lähenemise eriti atraktiivseks päikesepaneelide koha peal tootmiseks Kuul. Püsiasustuste rajamist Kuul planeeritakse praegu koostöös NASA ja Euroopa Kosmoseagentuuriga.

Käesolevas doktoritöös süteesiti püriidi mikrokristalle sulasoola meetodi abil. Leiti, et väävel ei ole sobiv kasvukeskkond, kuna selle eemaldamine pärast sünteesi sublimatsiooni ja keemilise söövitusega kahjustab kristalli koostist ja pinda, mida kinnitasid Raman spektroskoopia ja röntgen-fotoelektronspektroskoopia (XPS). Vastupidiselt võimaldas kaaliumjodiidi (KI) sula faasi kasvukeskkonnana kasutamine süteesida individuaalselt vormunud püriidikristalle ühtlase koostise ja siledate pindadega. Raman spektroskoopia tuvastas iseloomulikud piigid 343, 350, 379 ja 430 cm^{-1} juures, mis kõik vastavad püriidi faasile. Röntgendifraktsiooni (XRD) analüüs kinnitas faasi puhtust; kristallide arvutatud võreparameeter oli a = b = c = 5,4154 Å, mis on kooskõlas püriidi kuupsümeetriaga.

XPS-analüüs kinnitas püriidi pöördpinna efekti. Pinnal olevad Fe^{2+} ioonid olid suures osas oksüdeerunud Fe^{3+} ioonideks ning S$_2^{2-}$ paarid olid lagunenud üksikuteks S^{2-} ioonideks. Need pinnadefektid tekitavad täiendavaid energiatasemeid keelutsoonis, põhjustades pinnal *p*-tüüpi juhtivust. Keemiline söövitus H$_2$SO$_4$+H$_2$O$_2$ seguga ei vähendanud oluliselt pinnadefekte. Sublimeerimine väävliärastuseks seevastu eemaldas täielikult väävli püriidi pinnalt. Järgnev söövitus kaaliumtsüaniidi lahusega taastas XPS-spektris väävli signaalid, viidates pinnakoostise osalisele taastumisele.

Võrreldi erinevaid kasvukeskkondi, et hinnata erinevate sulasoolade mõju kristallikasvule ja lisandite sisseviimisele. Püriidi kristallid, mis olid süteesitud KI, liitiumjodiidi (LiI) ja tseesiumjodiidi (CsI) keskkonnas, olid morfoloogialt sarnased, samas kui naatriumpolüsulfiidi (Na$_2$S$_x$) või ilma sulasoolata süteesitud materjalid olid kasvanud väikeste kristalliitidena, mis ei olnud veel kujunenud individuaalseteks mikrokristallideks. Raman- ja XRD-analüüsid tuvastasid kõigis proovides vaid püriidi faasi. Massispektromeetria näitas aga kõrgeid lisandite kontsentratsioone, eriti siirdemetallide

nagu Cr, Cu, Co ja Ni puhul. Siirdemetallide sisaldus oli 10^{17} ja 10^{18} aatomit cm^{-3} vahel. Kõrgeim Li sisaldus oli püriidis, mis sünteesiti LiI keskkonnas, ulatudes 10^{19} aatomit cm^{-3}-ni. CsI-s sünteesitud materjalides oli Cs sisaldus samuti 10^{19} aatomit cm^{-3}, kuid kõrge Cs-kontsentratsioon (kuni 5×10^{17} aatomit cm^{-3}) leiti ka kristallides, mis olid sünteesitud LiI-s. Leiti, et Cs lisand eksisteerib juba LiI soolas, mis viitab sellele, et LiI ei ole optimaalne sulasool sünteesis kasutamiseks. Leiti ka, et püriidi rekristallimine suurema mahu KI-ga vähendas oluliselt vase lisandi kogust, võimaldades sünteesida kõrgema puhtusega püriidi kristalle.

Ultraviolett-fotoelektronspektroskoopia (UPS) analüüs näitas, et erinevate lisandiprofiilidega püriidi kristallides on tugevalt erinev energiatasemete struktuur. UPS-andmed kinnitasid ka kristallide n-tüüpi juhtivuse, kuna leiti, et Fermi energiatase paiknes juhtivustsooni miinimumile väga lähedal. Leiti ka, et proovides, mis sünteesiti erinevates keskkondades ja mis sisaldasid erinevaid lisandeid, ilmusid fotoluminestsentsi (PL) spektrite kiirgusribad erinevate energiate juures. See näitab, et lisandite sisseviimine mõjutab tugevalt rekombinatsioonikanaleid. Täpsem PL-analüüs on vajalik, et paremini mõista püriidi defektkoostist.

Arvestades, et püriidikristallide süntees sulasoola keskkonnas võimaldab lisandite sisseviimist, oli järgmine samm uurida sihipärast legeerimist püriidis, et saavutada ühtlane p-tüüpi juhtivus. Legeerivaks elemendiks valiti fosfor (P). Selgus, et efektiivseks legeerimiseks tuleb fosforit sisse viia püriidi sünteesi käigus, kuna sünteesijärgsed töötlused ja rekristallimine legeerimise eesmärgil osutusid ebaefektiivseks. Leiti, et fosfor tuleb sisse viia anioonina; seetõttu viidi esmalt läbi süntees raudsulfiidiga, et moodustada FeP$_4$ faas, mida seejärel lisati püriidi sünteesi juurde. Kui lisada 5 at% fosforit püriidis sisalduva väävli kohta, oli tulemuseks p-tüüpi püriidi mikrokristallid, mida iseloomustasid säilinud morfoloogia ja faasikoostis, mida kinnitasid Raman spektroskoopia ja XRD.

Esimest korda valmistati monoterakiht-päikesepatareid, mille valgust neelavas kihis kasutati püriidi mikrokristalle koos nikkeloksiidi puhverkihiga. Kuigi esialgsetes seadmetes tekkis üliväike fotovool, kinnitab dioodilaadne käitumine heterosiirde moodustumist. Need tulemused viitavad, et edasise optimeerimise korral võivad püriidipõhised päikesepatareid leida kasutust nii Maal kui ka väljaspool.

Appendix

Pyrite as prospective absorber material for monograin layer solar cell

Katriin Kristmann [a], Mare Altosaar [a], Jaan Raudoja [a], Jüri Krustok [a,b], Maris Pilvet [a], Valdek Mikli [a], Maarja Grossberg [a], Mati Danilson [a], Taavi Raadik [a,*]

[a] *Department of Materials and Environmental Technology, Tallinn University of Technology, Ehitajate Tee 5, 19086, Tallinn, Estonia*
[b] *Division of Physics, Tallinn University of Technology, Ehitajate tee 5, 19086 Tallinn, Estonia*

A B S T R A C T

FeS_2 monograin powders as absorber materials in monograin layer solar cells were grown in the molten phase of two different flux materials - in liquid sulphur (S) and in potassium iodide (KI) at different temperatures - at 500 °C, 550 °C, 600 °C in S and at 740 °C in KI. The cooling temperature profiles were modified to preserve the pyrite phase of material until room temperature was reached. FeS_2 microcrystals, synthesized in sulphur and recrystallized in molten KI as flux, had cubic structure of pyrite phase with stoichiometric composition, confirmed by X-ray diffraction, Raman, and energy dispersive X-ray analyses, respectively. The grown FeS_2 crystals exhibited *n-type* conductivity determined by hot probe measurements. The powder crystals were fixed in monograin membranes for making heterostructures with *p-type* nickel oxide (NiO) buffer layer. Charge carrier concentrations 6.2×10^{16} and 2.5×10^{17} cm^{-3}, were found from capacitance-voltage measurements using FeS_2/NiO heterostructures and FeS_2/Pt Schottky diodes, respectively.

1. Introduction

There is continuous search for cheap, earth abundant, environmentally friendly and nontoxic materials for solar cell absorber [1]. FeS_2 in the pyrite crystal structure is a promising candidate for solar cell absorber as it has suitable band gap of $Eg = 0.95$ eV, effective light absorption coefficient ($\alpha > 10^5$ cm^{-1} for $h\nu > 1.3$ eV), an adequate minority carrier diffusion length (100–1000 nm) and high electron mobility up to 360 cm^2 V^{-1} s^{-1} at room temperature[2–5]. FeS_2 offers possibilities for electricity production at the lowest price compared with the other known solar cell materials. In a comparative study published in 2009 by Wadia et al. [6] involving different absorber materials, it was suggested that FeS_2 could be the cheapest material with the highest potential for electricity production, outweighing Si in every aspect. Some key topics that favour FeS_2 over Si were given in the ref. [6] as: extraction cost ($1.70 per kg for Si vs $0.03 per kg for Fe), the energy input for extraction (24 kWh kg^{-1} for Si vs 2 kWh kg^{-1} for Fe), and a low cost of the raw material per peak watt (0.039 ¢ per W for Si vs <0.000002 ¢ per W for FeS_2). Taking the earth abundance and extraction cost into consideration, it was speculated that a 4% efficient FeS_2 solar cell could produce the electricity at the same price that of a 19% efficient Si solar cell [6] . The theoretical calculated efficiency limit (the Shockley–Queisser limit) for pyrite solar cells is 25% [3]. FeS_2 has been explored for thin film solar cells, but after little progress the research has lately impeded. Since the first report of FeS_2 solar cells by A. Ennaoui

and H. Tributsch in 1984 [7] the FeS_2 solar cells have never shown power conversion efficiency (PCE) greater than 3% [3], despite high interest of scientists over three decades. Low PCE values are mainly the result of poor photovoltage, that never exceeds 0.3 V. Low PCE of FeS_2 is attributed to a high concentration of defects on the top surface of FeS_2 crystals, turning the crystals' surface *p-type*. FeS_2 thin films are commonly *p-type*, and they exhibit no photoelectrochemical response while single crystals are commonly *n-type* [2]. The origin of the unintentional *n-type* doping of pyrite FeS_2 is attributed to sulphur vacancies. In the review paper of K. Ellmer and C. Höffner [8] the authors concluded that FeS_2 is a stoichiometric compound having only slight deviations from the nominal sulphur-to-iron ratio of 2.0. The S deficiency on the surface of FeS_2 crystals is argued to be from 1 at% up to 13 at%, that may turn the bandgap of pyrite surface to zero and therefore highly conductive [2] . Volatile sulphur can easily leave from formed FeS_2 crystals' surfaces in these synthesis technologies where the escaping of sulfur is not held back, resulting in sulphur-poor composition of crystals' surface. M. Limpinsel et al. [9] showed that a hole-rich *p-type* surface layer was formed on the top of single crystals of FeS_2 and suggested that this *p-type* surface layer could possibly be eliminated by passivating surface states and subsurface defects. They showed that chemical surface treatments can substantially reduce the conductivity of the inversion layer.

This hole-rich inversion layer at the surface of pyrite crystals results in a leaky or small potential energy barrier [3,9]. Nesbitt et al. [10]
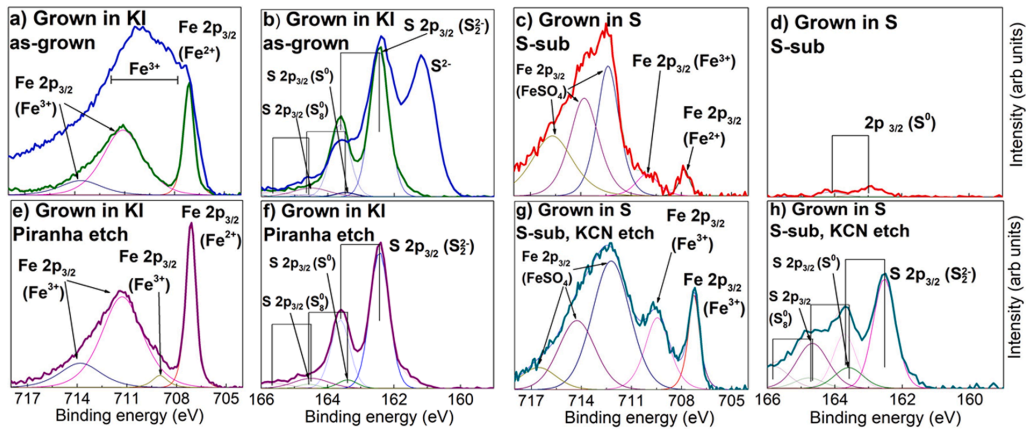
Fig. 5. High-resolution XPS core level spectra based on fitting results of Fe 2p and S 2p obtained from the surface of FeS$_2$ crystals grown in molten KI (Fig. 5a, b, e, f) and molten sulphur (Fig. 5c,d, g,h). XPS spectra were measured after dissolution of KI by water (Fig. 5a, b) marked as green line and after following etching with "Piranha" solution (Fig. 5e, f). Spectra of as-grown powders released from KI and sputtered with Ar$^+$ ions for 60 s are also presented as blue lines in graphs Fig. 5.a and Fig. 5.b. XPS spectra from crystals grown in molten sulphur were recorded after removal of sulphur by vacuum sublimation (Fig. 5c, d) and after following chemical etching with KCN solution (Fig. 5c,d). Sulphur spectra on Fig. 5b,d,f,h exhibit 2p$_{3/2}$ and 2p$_{1/2}$ doublet signals with interval 1,2 eV, the doublets on graphs are marked by rectangular brackets, only the higher intensity component S 2p$_{3/2}$ is shown for each doublet.

avoid the formation of unwanted iron sulphide phases if to proceed at higher temperatures, provide the conditions for phase transformation and quench the material quickly [15]. Synthesis route for phase pure pyrite was determined based on the Raman analysis. It is important to proceed at higher temperatures during the synthesis, provide the conditions for phase transformation into pyrite phase, and quench the material quickly for cooling to room temperature [15].

According to the EDX results, crystals grown at 500 °C have an iron rich composition of 39.21 at.% iron and 60.79 at.% sulphur. The composition shifts to more stoichiometric side with increasing growth temperature: crystals synthesized at 550 °C and 600 °C are closer to the stoichiometric composition of pyrite as 33.06 at.% Fe and 66.94 at.% S for 550 °C; 33.42 at.% Fe and 66.58 at.% S for 600 °C, respectively. Crystals recrystallized at 740 °C had composition of 33.77 at.% iron and 66.23 at.% sulphur. Even though EDX analyses showed almost stoichiometric compositions to the materials grown at 550 °C and 600 °C, there were still some additional phases and elemental sulphur that was confirmed by Raman.

The microcrystals were also analysed by XRD, the pattern can be seen in Fig. 3 and Fig. 4. XRD pattern of crystals that were synthesized in sulphur flux at 600 °C are seen on Fig. 3. These crystals had been etched with KCN solution to remove the S flux. Crystals that were recrystallized in liquid KI flux at 740 °C, where the flux had been removed by rinsing with water are seen on Fig. 4. It is evident from Fig. 3 that the powders include several additional crystalline phases such as marcasite and pyrrhotite in addition to pyrite. A possible haematite Fe$_2$O$_3$ peak was also observed in the XRD pattern. The quantity of different crystalline compositions can be related to the etching with KCN solution, which removed some of the sulphur, leaving a variable Fe$_{1-x}$S composition. It has been published by Chen et al. [17] that the iron-sulphur system has a multitude of phases in lower sulphur supply at different temperatures, that change the conditions for phase transition into pyrite and from pyrite into pyrrhotite. The XRD pattern of powders after recrystallization in KI at 740->575 °C shows that the additional phases are removed and transformed into pyrite phase. The resulting pure pyrite phase has lattice parameters $a = b = c = 5.4154$ Å, which confirms the cubic structure and agrees with the values reported in the literature [30–32]. Additionally, XRD supports Raman results that there are no secondary phases in the crystals recrystallized at 740 °C in KI flux.

As it is reported also in literature [11], all synthesized FeS$_2$ crystals

(at 500, 550, 600 and 740 ºC) exhibited n-type conductivity according to the hot probe measurements.

3.4. XPS study of microcrystals

The XPS analysis was used to study the changes in the binding energies of constituent elements of FeS$_2$ crystals depending on different synthesis conditions and flux removal methods. XPS spectra of crystals grown in sulphur were recorded after removal of sulphur by vacuum sublimation and after additional chemical etching with KCN solution. FeS$_2$ crystals grown in molten KI flux were measured after dissolution of KI by water and after following etching with so called "Piranha" solution (H$_2$O$_2$+ H$_2$SO$_4$). Fig. 5a and Fig. 5b presents the XPS core level spectra of Fe 2p and S 2p before and after sputtering of the crystals surface for 60 s with Ar$^+$ ions with the aim to remove the surface contamination seen in the XPS survey spectrum (not presented in this paper). But it can be noticed that Fe 2p and S 2p XPS spectra are strongly influenced by sputtering. After sputtering, all spectra in the iron region show a strong increase in signal in the area of Fe^{3+} species (shown as a horizontal line in Fig. 5a) while the signal of Fe^{2+} near 707 eV that belongs to pyrite [10] is much less intensive. In the energy region of sulphur XPS signals, the effect of sputtering is even stronger. In addition to the doublet signal of S 2p$_{3/2}$ and S 2p$_{1/2}$ (at 162.4 and 163.6 eV with the distance of 1.2 eV) that represents the emission of bulk S$_2^{2-}$ [10,33,34] there emerges a peak at 161.3 eV characteristic to monosulfide S^{2-} surface state [10]. These afore described effects were present in all spectra of sputtered samples after each synthesis and treatment regime. The appearance of Fe^{3+} ionic states and S^{2-} monosulphide signals are similar to the phenomena characteristic to the pyrite surface mechanical fracturing described by Nesbitt et al. [10]. Due to the before described changes in XPS spectra accompanied with sputtering (surface damage of FeS$_2$ crystals) that disfigure the XPS spectra, only spectra of unsputtered pyrite samples were used for fitting the spectra to the spectral components.

The Fe 2p XPS spectra (in Fig. 5a, c, e, g) include contributions from bulk Fe^{2+} 2p$_{3/2}$ emission near 707 eV [10,35], which is the most characteristic to the pyrite phase. The peak at 707 eV is more obvious for samples that were crystallized in KI flux and weaker for powders synthesized in sulphur flux. All Fe 2p spectra exhibit emissions from energies between 708 and 713.8 eV, that are attributed to the Fe^{3+} ionic
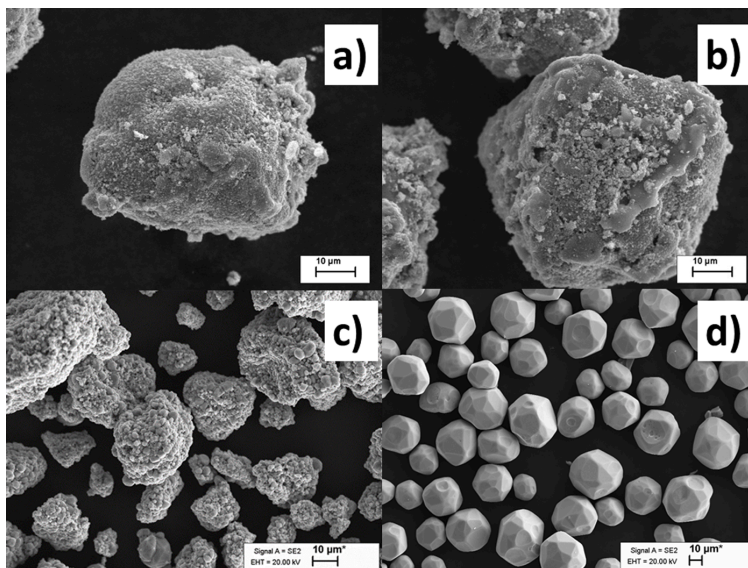
Fig. 1. SEM images of FeS$_2$ synthesized at a) 500 °C in S flux b) 550 °C in S flux c) 600 °C in S flux and d) FeS$_2$ crystals recrystallized at 740 °C in KI flux.
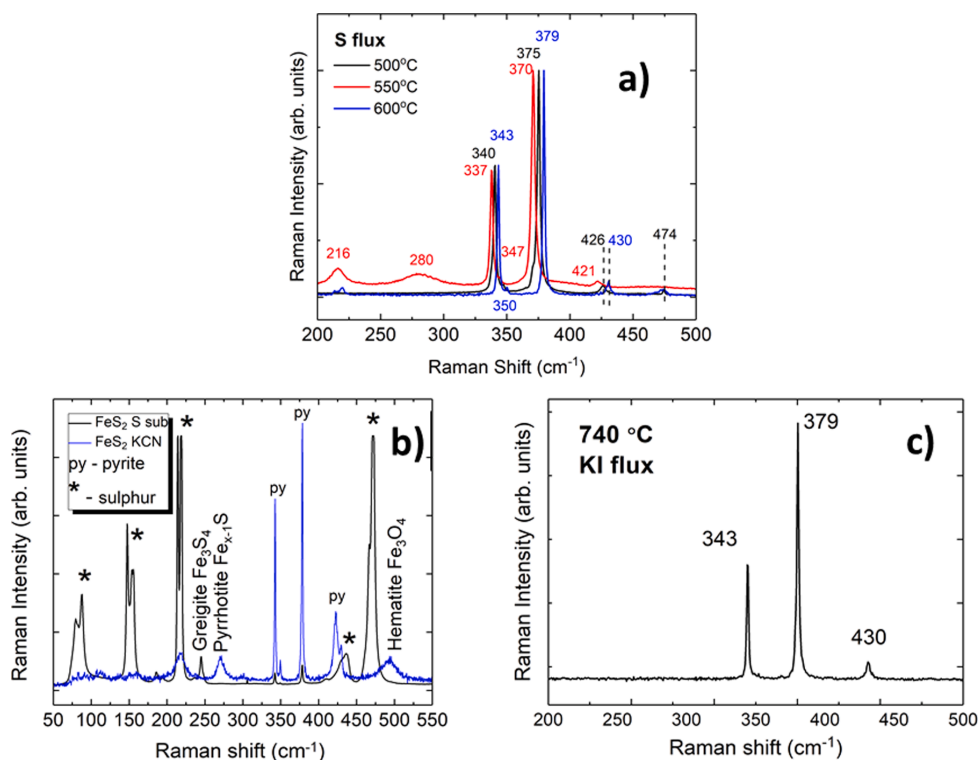

Fig. 2. a) Raman spectra of FeS$_2$ crystals synthesized at 500 °C, 550 °C and 600 °C in S flux. S was removed by vacuum sublimation and etching. b) Raman spectra of FeS$_2$ crystals synthesized at 550 °C in S flux. After vacuum sublimation (black line) and after sublimation and KCN etching (blue line). c) Raman spectrum of FeS$_2$ crystals recrystallized at 740 °C in KI flux.

cubic structure of pyrite phase with stoichiometric composition, as confirmed by XRD, Raman and EDX analyses, respectively. Based on XPS analysis it was concluded that a) vacuum sublimation results in sulphur-poor FeS_2 surface that can be restored by following KCN etching; b) the "Piranha" treatment in the used conditions (concentration, temperature and time) did not help to avoid the phenomenon of surface Fe^{2+} oxidation to Fe^{3+}; c) the crystals synthesized in KI flux exhibited stronger indication of the pyrite phase and less secondary compounds such as $FeSO_4$. Grown crystals exhibited *n-type* conductivity determined by hot probe measurements. Therefore, *p-type* NiO was deposited by the SILAR method on the top of the crystals in order to form FeS_2/NiO heterostructure. Additionally, FeS_2 Schottky diodes were fabricated with Pt and Au contacts. Via the *C-V* measurements, the charge carriers' concentrations of 6.2×10^{16} and 2.5×10^{17} cm^{-3} were found using FeS_2/NiO heterostructures andFeS_2/Pt Schottky diodes, respectively.

CRediT authorship contribution statement

Katriin Kristmann: Writing – original draft, Writing – review & editing, Investigation, Formal analysis. **Mare Altosaar:** Writing – review & editing, Formal analysis. **Jaan Raudoja:** Resources. **Jüri Krustok:** Writing – original draft, Investigation. **Maris Pilvet:** Resources. **Valdek Mikli:** Investigation, Formal analysis. **Maarja Grossberg:** Writing – original draft, Supervision, Funding acquisition, Project administration. **Mati Danilson:** Investigation, Writing – review & editing, Formal analysis. **Taavi Raadik:** Writing – original draft, Writing – review & editing, Investigation, Funding acquisition, Project administration.

Declaration of Competing Interest

The authors declare the following financial interests/personal relationships which may be considered as potential competing interests

References

[1] A. Le Donne, V. Trifiletti, S. Binetti, New earth-abundant thin film solar cells based on chalcogenides, Front. Chem. 7 (2019), https://doi.org/10.3389/fchem.2019.00297.

[2] L. Yu, S. Lany, R. Kykyneshi, V. Jieratum, R. Ravichandran, B. Pelatt, E. Altschul, H.A.S. Platt, J.F. Wager, D.A. Keszler, A. Zunger, Iron chalcogenide photovoltaic absorbers, Adv. Energy Mater. (2011), https://doi.org/10.1002/aenm.201100351.

[3] M. Rahman, G. Boschloo, A. Hagfeldt, T. Edvinsson, On the mechanistic understanding of photovoltage loss in iron pyrite solar cells, Adv. Mater. (2020), https://doi.org/10.1002/adma.201905653.

[4] C. Steinhagen, T.B. Harvey, C.J. Stolle, J. Harris, B.A. Korgel, Pyrite nanocrystal solar cells: promising, or fool's gold? J. Phys. Chem. Lett. (2012) https://doi.org/10.1021/jz301023c.

[5] R.P. Srivastava, A.P. Saxena, S. Ingole, n-Type iron pyrite (FeS₂) thin-films obtained at different sulfur vapor pressures, Chalcogenide Lett. (2017).

[6] C. Wadia, A.P. Alivisatos, D.M. Kammen, Materials availability expands the opportunity for large-scale photovoltaics deployment, Environ. Sci. Technol. (2009), https://doi.org/10.1021/es8019534.

[7] A. Ennaoui, H. Tributsch, Iron sulphide solar cells, Sol. Cells. (1984), https://doi.org/10.1016/0379-6787(84)90009-7.

[8] K. Ellmer, C. Höpfner, On the stoichiometry of the semiconductor pyrite (FeS₂), Philos. Mag. A Phys. Condens. Matter, Struct. Defects Mech. Prop. (1997), https://doi.org/10.1080/01418619708214015.

[9] M. Limpinsel, N. Farhi, N. Berry, J. Lindemuth, C.L. Perkins, Q. Lin, M. Law, An inversion layer at the surface of n-type iron pyrite, Energy Environ. Sci. (2014), https://doi.org/10.1039/c3ee43169j.

[10] H.W. Nesbitt, Sulfur and iron surface states on fractured pyrite surfaces, Am. Mineral. (1998), https://doi.org/10.2138/am-1998-9-1015.

[11] J. Walter, X. Zhang, B. Voigt, R. Hool, M. Manno, F. Mork, E.S. Aydil, C. Leighton, Surface conduction in n -type pyrite FeS₂ single crystals, Phys. Rev. Mater. (2017), https://doi.org/10.1103/PhysRevMaterials.1.065403.

[12] M. Altosaar, A. Jagomägi, M. Kauk, M. Krunks, J. Krustok, E. Mellikov, J. Raudoja, T. Varema, Monograin layer solar cells, Thin Solid Films (2003), https://doi.org/10.1016/S0040-6090(03)00167-6.

[13] K. Timmo, M. Kauk-Kuusik, M. Pilvet, M. Altosaar, M. Grossberg, M. Danilson, R. Kaupmees, V. Mikli, J. Raudoja, T. Varema, Cu(In,Ga)Se₂ monograin powders with different Ga content for solar cells, Sol. Energy. 176 (2018) 648–655, https://doi.org/10.1016/J.SOLENER.2018.10.078.

[14] O. Kubaschewski von Goldbeck, Iron—sulphur Fe—S. IRON—Binary Phase Diagrams, Springer-Verlag, 1982, pp. 125–128, https://doi.org/10.1007/978-3-662-08024-5.

[15] D. Shishin, E. Jak, S.A. Decterov, Critical assessment and thermodynamic modeling of the Fe-O-S system, J. Phase Equilibria Diffus. (2015), https://doi.org/10.1007/s11669-015-0376-4.

[16] M. Altosaar, E. Mellikov, CuInSe 2 monograin growth in CuSe-Se liquid phase, Jpn. J. Appl. Phys. (2000), https://doi.org/10.7567/jjaps.39s1.65.

[17] Y.-.H. Chen, Y.-.H. Chen, W.-.D. Hsu, Y.-.C. Chang, H.-.S. Sheu, J.-.J. Lee, S.-.K. Lin, Using the high-temperature phase transition of iron sulfide minerals as an indicator of fault slip temperature, Sci. Rep. 9 (2019), https://doi.org/10.1038/s41598-019-44319-8.

[18] W.M. H.aynes, CRC Handbook of Chemistry and Physics, Internet Version, 95th Edition, CRC Press/Taylor and Francis, Boca Raton, FL, 2015.

[19] Y. Akaltun, T. Çayır, Fabrication and characterization of NiO thin films prepared by SILAR method, J. Alloys Compd. (2015) 625, https://doi.org/10.1016/j.jallcom.2014.10.194.

[20] I. Leinemann, K. Timmo, M. Grossberg, T. Kaljuvee, K. Tõnsuaadu, R. Traksmaa, M. Altosaar, D. Meissner, Reaction enthalpies of Cu2ZnSnSe4 synthesis in KI, J. Therm. Anal. Calorim. (2015), https://doi.org/10.1007/s10973-014-4339-5.

[21] K. Timmo, M. Kauk-Kuusik, M. Pilvet, M. Altosaar, M. Grossberg, M. Danilson, R. Kaupmees, V. Mikli, J. Raudoja, T. Varema, Cu(In,Ga)Se2 monograin powders with different Ga content for solar cells, Sol. Energy. (2018), https://doi.org/10.1016/j.solener.2018.10.078.

[22] M. Altosaar, J. Raudoja, K. Timmo, M. Danilson, M. Grossberg, M. Krunks, T. Varema, E. Mellikov, Cu2ZnSnSe4 monograin powders for solar cell application, in: Conf. Rec. 2006 IEEE 4th World Conf. Photovolt, Energy Conversion, WCPEC-4, 2006, https://doi.org/10.1109/WCPEC.2006.279492.

[23] K. Timmo, M. Kauk-Kuusik, M. Pilvet, V. Mikli, E. Kärber, T. Raadik, I. Leinemann, M. Altosaar, J. Raudoja, Comparative study of SnS recrystallization in molten CdI2, SnCl2and KI, Phys. Status Solidi Curr. Top. Solid State Phys. (2016), https://doi.org/10.1002/pssc.201510082.

[24] H. Vogt, T. Chattopadhyay, H.J. Stolz, Complete first-order Raman spectra of the pyrite structure compounds FeS2, MnS2 AND SiP2, J. Phys. Chem. Solids. (1983), https://doi.org/10.1016/0022-3697(83)90124-5.

[25] A.N. Utyuzh, Influence of temperature on raman spectra of the FeS2 single crystal with pyrite structure, Phys. Solid State. (2014), https://doi.org/10.1134/S1063783414100321.

[26] D.L.A. De Faria, S. Venâncio Silva, M.T. De Oliveira, Raman microspectroscopy of some iron oxides and oxyhydroxides, J. Raman Spectrosc. 28 (1997) 876–878, https://doi.org/10.1002/(sici)1097-4555(199711)28:11<873::aid-jrs177>3.0.co;2-b.

[27] A.T. Ward, Raman spectroscopy of sulfur, sulfur-selenium, and sulfur-arsenic mixtures, J. Phys. Chem. (1968), https://doi.org/10.1021/j100858a031.

[28] Y. El Mendili, A. Abdelouas, H. El Hajj, J.-.F. Bardeau, Phase transitions of iron sulphides formed by steel microbial corrosion, RSC Adv 3 (2013) 26343–26351, https://doi.org/10.1039/c3ra45259j.

[29] M. Grossberg, J. Krustok, J. Raudoja, K. Timmo, M. Altosaar, T. Raadik, Photoluminescence and Raman study of Cu2ZnSn(Se xS1 - X)4 monograins for photovoltaic applications, Thin Solid Films (2011), https://doi.org/10.1016/j.tsf.2010.12.099.

[30] A. Zavrazhnov, A. Naumov, A. Kosyakov, S. Berezin, V. Volkov, A. Sergeeva, The Iron Sulfides Crystal Growth from the Halide Melts, Mater. Res. (2018), https://doi.org/10.1590/1980-5373-mr-2017-0648.

[31] P. Prabukanthan, S. Thamaraiselvi, G. Harichandran, Single step electrochemical deposition of p-Type Undoped and Co 2+ doped FeS2 thin films and performance in heterojunction solid solar cells, J. Electrochem. Soc. (2017), https://doi.org/10.1149/2.0991709jes.

[32] H. Ning, Z. Liu, Y. Xie, H. Huang, CoS2 coatings for improving thermal stability and electrochemical performance of FeS2 cathodes for thermal batteries, J. Electrochem. Soc. (2018), https://doi.org/10.1149/2.0321809jes.

[33] C.M. Eggleston, J.-.J. Ehrhardt, W. Stumm, Surface structural controls on pyrite oxidation kinetics; an XPS-UPS, STM, and modeling study, Am. Mineral. (1996) 81, https://doi.org/10.2138/am-1996-9-1002.

[34] M. Fantauzzi, B. Elsener, D. Atzei, A. Rigoldi, A. Rossi, Exploiting XPS for the identification of sulfides and polysulfides, RSC Adv 5 (2015), https://doi.org/10.1039/C5RA14915K.

[35] P. Behra, P. Bonnissel-Gissinger, M. Alnot, R. Revel, J.J. Ehrhardt, XPS and XAS Study of the Sorption of Hg(II) onto Pyrite, Langmuir (2001) 17, https://doi.org/10.1021/la0014510.

[36] A.P. Grosvenor, B.A. Kobe, M.C. Biesinger, N.S. McIntyre, Investigation of multiplet splitting of Fe 2p XPS spectra and bonding in iron compounds, Surf. Interface Anal. 36 (2004), https://doi.org/10.1002/sia.1984.

[37] G. Senanayake, The cyanidation of silver metal: review of kinetics and reaction mechanism, Hydrometallurgy (2006) 81, https://doi.org/10.1016/j.hydromet.2005.12.001.

[38] Z. Mutlu, B. Debnath, S. Su, C. Li, M. Ozkan, K.N. Bozhilov, R.K. Lake, C.S. Ozkan, Chemical vapor deposition and phase stability of pyrite on SiO2, J. Mater. Chem. C. (2018) 6, https://doi.org/10.1039/C8TC00584B.

[39] R. Steudel, Liquid sulfur, in: R. Steudel (Ed.), Elemental Sulfur and Sulfur-Rich Compounds I, Springer-Verlag, 2003, pp. xx–yy, https://doi.org/10.1007/b12115.

[40] Y. Sato, M. Fukasawa, T. Yamamura, Viscosities of molten alkali-metal bromides and iodides, Int. J. Thermophys. (1997), https://doi.org/10.1007/BF02575253.

[41] M. Limpinsel, Ph.D. Thesis, University of California, Irvine, 2015.

[42] P.P. Altermatt, T. Kiesewetter, K. Ellmer, H. Tributsch, Specifying targets of future research in photovoltaic devices containing pyrite (FeS2) by numerical modelling, Sol. Energy Mater. Sol. Cells. (2002), https://doi.org/10.1016/S0927-0248(01)00053-8.

[43] W.M.H. Sachtler, G.J.H. Dorgelo, A.A. Holscher, The work function of gold, Surf. Sci. (1966), https://doi.org/10.1016/0039-6028(66)90083-5.

[44] G.N. Derry, Z. Ji-Zhong, Work function of Pt(111), Phys. Rev. B. (1989), https://doi.org/10.1103/PhysRevB.39.1940.

[45] G. Willeke, O. Blenk, C. Kloc, E. Bucher, Preparation and electrical transport properties of pyrite (FeS2) single crystals, J. Alloys Compd. (1992), https://doi.org/10.1016/0925-8388(92)90260-G.
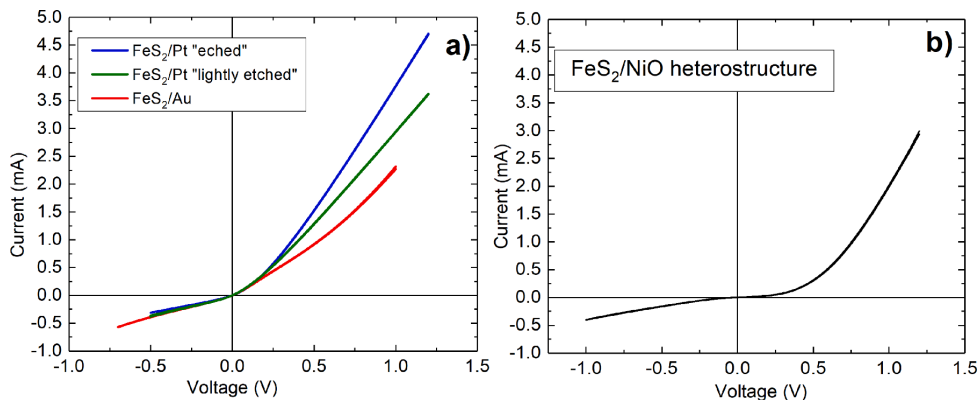
Fig. 6. *I-V* curves of FeS$_2$/NiO heterostructure (left) and Schottky diodes with Pt and Au contacts. Membranes with Pt electrodes were etched preliminary with "Piranha" solution (H$_2$SO$_4$: H$_2$O$_2$ = 3: 1), for 10 s in the case of "light" etching and for 60 s in the case of "etched" FeS$_2$ sample.

states [10,33,36]. Spectra of powders synthesized in sulphur flux have multiplet spectral contributions from FeSO$_4$ states at binding energies 712.2–716.6 eV [36]. Inclusion of oxygen in the samples comes likely from the impure synthesis precursors, such as elemental sulphur powder. Applied KCN etching of powders synthesized in sulphur flux did not remove any signal from SO$_4{}^{2-}$ component but brought out signals of the pyrite phase (compare the Fig. 5d and Fig. 5h) by removing the intermediate (damaged by sublimation) surface layer. After the etching procedure, the Fe 2p spectre exhibits a stronger Fe^{2+} signal and clear disulphide and sulphide signals in the S 2p region. The removal of FeS and FeS$_x$ can be described by the following reaction [37]:

$$FeS + 6KCN \rightarrow K_4\left[Fe(CN)_6\right] + K_2S \qquad (1)$$

The Fe 2p$_{3/2}$ signal that appeared at 709 eV after etching the crystals with "Piranha" solution (compare Fig. 5a and Fig. 5e) is an evidence of Fe$_2$O$_3$ formation on the surface [33,38]. It indicates that some of the Fe^{2+} had been oxidized to Fe^{3+}. It seems that the treatment with "Piranha" solution in the used conditions (concentration, temperature and time) did not help to avoid the phenomenon of surface Fe^{2+} oxidation to Fe^{3+} upon surface fracture (disruption of S-S bond) that was described by Nesbitt et al. [10].

The S 2p XPS spectra (in Fig. 5b, d, f, h) include bulk disulfide S$_2{}^{2-}$ contributions with a doublet signal at 162.6 eV. Separation of the S 2p$_{3/2}$ and S 2p$_{1/2}$ doublet is 1.2 eV [10,34,38]. The S part of XPS spectrum of the powder synthesized in sulphur and sublimed (see Fig. 5d), exhibits only a very weak doublet of peaks at energies 162.9 and 164 eV attributed to elemental sulphur in the Ref. [34]. This is a suggestion that the used vacuum sublimation removed almost all of the sulphur from the utmost surface of FeS$_2$ crystals. The XPS spectrum recorded after following KCN etching (Fig. 5h) revealed again the disulfide S$_2{}^{2-}$ contributions that belong to the pyrite phase. This fact suggests that applying KCN etching to the sublimed powder reveals the pyrite surface (compare Fig. 5d and Fig. 5h) by dissolving and removing surface FeS$_x$ into etching solution via complexing Fe into hexacyanoferrate complex ions (reaction 1). Doublet peaks of elemental sulphur S^0 and polysulphide S$_8{}^\circ$ at 163.5 and 164.7 eV and at 164.6 and 165.8 eV, respectively, are apparent in Fig. 5h. In Ref. [10,34] these doublets were attributed to the unreacted elemental sulphur.

Based on XPS analysis it was concluded that a) vacuum sublimation results in sulphur-poor FeS$_2$ surface that can be restored by following KCN etching; b) the "Piranha" treatment in the used conditions (concentration, temperature and time) did not help to avoid the phenomenon of surface Fe^{2+} oxidation to Fe^{3+}; c) the crystals synthesized in KI flux exhibited stronger indication of the pyrite phase and less secondary compounds such as FeSO$_4$. One reason for the formation and growth of

more developed crystals in molten KI is its lower viscosity. The diffusion dynamics for the growth of pyrite crystals is different in liquid S and KI. Sulphur has higher viscosity – 0.1 Pa$\cdot$s at its boiling point, 445 °C [39], which is below the growth temperature of 500 °C; viscosity of KI is 0.0012 Pa$\cdot$s at 740 °C [40]. The lower viscosity helps to dissolve and diffuse the material through liquid flux, therefore the larger crystals grow.

3.5. Schottky diodes and FeS$_2$/NiO hetero structure

The FeS$_2$ powder recrystallized in KI was sieved into narrow size fractions and the unisize crystals were used for the monograin membrane formation in order to prepare Schottky diodes and FeS$_2$/NiO heterostructure. Prior to device fabrication, the pyrite crystals surface was passivated. The surface was removed by etching with "Piranha" solution (H$_2$SO$_4$: H$_2$O$_2$ = 3:1), which is an oxidizing etchant that has been used by researchers [11,41] for improving pyrite surface parameters. Etching time was 10 s in the case of "light etching", which was done for the pyrite membranes on epoxy. 60 s etching regime was done for pyrite microcrystals prior to MGL fabrication. After etching procedures, the powders and membranes were cleaned with water and used for device fabrication.

It was detected by hot probe measurements, that pyrite microcrystals exhibited *n*-type conductivity. Thus, the finding of a suitable metal with higher work function than that of pyrite was needed. FeS$_2$ has work function of 3.9 eV [42], meaning that the work function of a partnering metal should be higher. Pt and Au with work functions of 6.1 eV and 5.45 eV, respectively [43,44], were deposited on pyrite monolayer membranes as *p/n* junction partners for pyrite/Pt and Pyrite/Au Schottky diodes. The current-voltage (I-V) curve of the formed diodes can be seen in Fig. 6a.

P-type NiO was deposited by SILAR method to form heterostructure with the pyrite membrane. I-V curve of heterostructure can be seen on Fig. 6b, unfortunately it didn't generate current and indicated the existence of pinholes in the structure. Charge carriers' concentrations 6.2 × 10^{16} and 2.5 × 10^{17} cm^{-3} were found from *C-V* measurements using FeS$_2$/NiO heterostructures and FeS$_2$/Pt Schottky diodes, respectively. These values are in good agreement with the results reported in literature [45].

4. Conclusion

In the current work we developed a procedure for growth of pyrite microcrystals to be used in monograin layer solar cell. FeS$_2$ microcrystals synthesized in sulphur and recrystallized in molten KI as flux, had

cubic structure of pyrite phase with stoichiometric composition, as confirmed by XRD, Raman and EDX analyses, respectively. Based on XPS analysis it was concluded that a) vacuum sublimation results in sulphur-poor FeS_2 surface that can be restored by following KCN etching; b) the "Piranha" treatment in the used conditions (concentration, temperature and time) did not help to avoid the phenomenon of surface Fe^{2+} oxidation to Fe^{3+}; c) the crystals synthesized in KI flux exhibited stronger indication of the pyrite phase and less secondary compounds such as $FeSO_4$. Grown crystals exhibited *n*-type conductivity determined by hot probe measurements. Therefore, *p*-type NiO was deposited by the SILAR method on the top of the crystals in order to form FeS_2/NiO heterostructure. Additionally, FeS_2 Schottky diodes were fabricated with Pt and Au contacts. Via the *C-V* measurements, the charge carriers' concentrations of 6.2×10^{16} and 2.5×10^{17} cm^{-3} were found using FeS_2/NiO heterostructures andFeS_2/Pt Schottky diodes, respectively.

CRediT authorship contribution statement

Katriin Kristmann: Writing – original draft, Writing – review & editing, Investigation, Formal analysis. **Mare Altosaar:** Writing – review & editing, Formal analysis. **Jaan Raudoja:** Resources. **Jüri Krustok:** Writing – original draft, Investigation. **Maris Pilvet:** Resources. **Valdek Mikli:** Investigation, Formal analysis. **Maarja Grossberg:** Writing – original draft, Supervision, Funding acquisition, Project administration. **Mati Danilson:** Investigation, Writing – review & editing, Formal analysis. **Taavi Raadik:** Writing – original draft, Writing – review & editing, Investigation, Funding acquisition, Project administration.

Declaration of Competing Interest

The authors declare the following financial interests/personal relationships which may be considered as potential competing interests
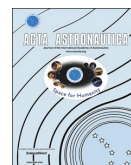
Acknowledgement

References

[1] A. Le Donne, V. Trifiletti, S. Binetti, New earth-abundant thin film solar cells based on chalcogenides, Front. Chem. 7 (2019), https://doi.org/10.3389/fchem.2019.00297.

[2] L. Yu, S. Lany, R. Kykyneshi, V. Jieratum, R. Ravichandran, B. Pelatt, E. Altschul, H.A.S. Platt, J.F. Wager, D.A. Keszler, A. Zunger, Iron chalcogenide photovoltaic absorbers, Adv. Energy Mater. (2011), https://doi.org/10.1002/aenm.201100351.

[3] M. Rahman, G. Boschloo, A. Hagfeldt, T. Edvinsson, On the mechanistic understanding of photovoltage loss in iron pyrite solar cells, Adv. Mater. (2020), https://doi.org/10.1002/adma.201905653.

[4] C. Steinhagen, T.B. Harvey, C.J. Stolle, J. Harris, B.A. Korgel, Pyrite nanocrystal solar cells: promising, or fool's gold? J. Phys. Chem. Lett. (2012) https://doi.org/10.1021/jz301023c.

[5] R.P. Srivastava, A.P. Saxena, S. Ingole, n-Type iron pyrite (FeS₂) thin-films obtained at different sulfur vapor pressures, Chalcogenide Lett. (2017).

[6] C. Wadia, A.P. Alivisatos, D.M. Kammen, Materials availability expands the opportunity for large-scale photovoltaics deployment, Environ. Sci. Technol. (2009), https://doi.org/10.1021/es8019534.

[7] A. Ennaoui, H. Tributsch, Iron sulphide solar cells, Sol. Cells. (1984), https://doi.org/10.1016/0379-6787(84)90009-7.

[8] K. Ellmer, C. Hopfner, On the stoichiometry of the semiconductor pyrite (FeS₂), Philos. Mag. A Phys. Condens. Matter, Struct. Defects Mech. Prop. (1997), https://doi.org/10.1080/01418619708214015.

[9] M. Limpinsel, N. Farhi, N. Berry, J. Lindemuth, C.L. Perkins, Q. Lin, M. Law, An inversion layer at the surface of n-type iron pyrite, Energy Environ. Sci. (2014), https://doi.org/10.1039/c3ee43169j.

[10] H.W. Nesbitt, Sulfur and iron surface states on fractured pyrite surfaces, Am. Mineral. (1998), https://doi.org/10.2138/am-1998-9-1015.

[11] J. Walter, X. Zhang, B. Voigt, R. Hool, M. Manno, F. Mork, E.S. Aydil, C. Leighton, Surface conduction in n -type pyrite FeS₂ single crystals, Phys. Rev. Mater. (2017), https://doi.org/10.1103/PhysRevMaterials.1.065403.

[12] M. Altosaar, A. Jagomägi, M. Kauk, M. Krunks, J. Krustok, E. Mellikov, J. Raudoja, T. Varema, Monograin layer solar cells, Thin Solid Films (2003), https://doi.org/10.1016/S0040-6090(03)00167-6.

[13] K. Timmo, M. Kauk-Kuusik, M. Pilvet, M. Altosaar, M. Grossberg, M. Danilson, R. Kaupmees, V. Mikli, J. Raudoja, T. Varema, Cu(In,Ga)Se2 monograin powders with different Ga content for solar cells, Sol. Energy. 176 (2018) 648–655, https://doi.org/10.1016/J.SOLENER.2018.10.078.

[14] O. Kubaschewski von Goldbeck, Iron—sulphur Fe—S. IRON—Binary Phase Diagrams, Springer-Verlag, 1982, pp. 125–128, https://doi.org/10.1007/978-3-662-08024-5.

[15] D. Shishin, E. Jak, S.A. Decterov, Critical assessment and thermodynamic modeling of the Fe-O-S system, J. Phase Equilibria Diffus. (2015), https://doi.org/10.1007/s11669-015-0376-4.

[16] M. Altosaar, E. Mellikov, CuInSe 2 monograin growth in CuSe-Se liquid phase, Jpn. J. Appl. Phys. (2000), https://doi.org/10.7567/jjaps.39s1.65.

[17] Y.-.H. Chen, Y.-.H. Chen, W.-.D. Hsu, Y.-.C. Chang, H.-.S. Sheu, J.-.J. Lee, S.-.K. Lin, Using the high-temperature phase transition of iron sulfide minerals as an indicator of fault slip temperature, Sci. Rep. 9 (2019), https://doi.org/10.1038/s41598-019-44319-8.

[18] W.M. H.aynes, CRC Handbook of Chemistry and Physics, Internet Version, 95th Edition, CRC Press/Taylor and Francis, Boca Raton, FL, 2015.

[19] Y. Akaltun, T. Çayır, Fabrication and characterization of NiO thin films prepared by SILAR method, J. Alloys Compd. (2015) 625, https://doi.org/10.1016/j.jallcom.2014.10.194.

[20] I. Leinemann, K. Timmo, M. Grossberg, T. Kaljuvee, K. Tõnsuaadu, R. Traksmaa, M. Altosaar, D. Meissner, Reaction enthalpies of Cu2ZnSnSe4 synthesis in KI, J. Therm. Anal. Calorim. (2015), https://doi.org/10.1007/s10973-014-4339-5.

[21] K. Timmo, M. Kauk-Kuusik, M. Pilvet, M. Altosaar, M. Grossberg, M. Danilson, R. Kaupmees, V. Mikli, J. Raudoja, T. Varema, Cu(In,Ga)Se2 monograin powders with different Ga content for solar cells, Sol. Energy. (2018), https://doi.org/10.1016/j.solener.2018.10.078.

[22] M. Altosaar, J. Raudoja, K. Timmo, M. Danilson, M. Grossberg, M. Krunks, T. Varema, E. Mellikov, Cu2ZnSnSe4 monograin powders for solar cell application, in: Conf. Rec. 2006 IEEE 4th World Conf. Photovolt, Energy Conversion, WCPEC-4, 2006, https://doi.org/10.1109/WCPEC.2006.279492.

[23] K. Timmo, M. Kauk-Kuusik, M. Pilvet, V. Mikli, E. Kärber, T. Raadik, I. Leinemann, M. Altosaar, J. Raudoja, Comparative study of SnS recrystallization in molten CdI2, SnCl2and KI, Phys. Status Solidi Curr. Top. Solid State Phys. (2016), https://doi.org/10.1002/pssc.201510082.

[24] H. Vogt, T. Chattopadhyay, H.J. Stolz, Complete first-order Raman spectra of the pyrite structure compounds FeS2, MnS2 AND SiP2, J. Phys. Chem. Solids. (1983), https://doi.org/10.1016/0022-3697(83)90124-5.

[25] A.N. Utyuzh, Influence of temperature on raman spectra of the FeS2 single crystal with pyrite structure, Phys. Solid State. (2014), https://doi.org/10.1134/S1063783414100321.

[26] D.L.A. De Faria, S. Venâncio Silva, M.T. De Oliveira, Raman microspectroscopy of some iron oxides and oxyhydroxides, J. Raman Spectrosc. 28 (1997) 876–878, https://doi.org/10.1002/(sici)1097-4555(199711)28:11<873::aid-jrs177>3.0.co;2-b.

[27] A.T. Ward, Raman spectroscopy of sulfur, sulfur-selenium, and sulfur-arsenic mixtures, J. Phys. Chem. (1968), https://doi.org/10.1021/j100858a031.

[28] Y. El Mendili, A. Abdelouas, H. El Hajj, J.-.F. Bardeau, Phase transitions of iron sulphides formed by steel microbial corrosion, RSC Adv 3 (2013) 26343–26351, https://doi.org/10.1039/c3ra45259j.

[29] M. Grossberg, J. Krustok, J. Raudoja, K. Timmo, M. Altosaar, T. Raadik, Photoluminescence and Raman study of Cu2ZnSn(Se xS1 - X)4 monograins for photovoltaic applications, Thin Solid Films (2011), https://doi.org/10.1016/j.tsf.2010.12.099.

[30] A. Zavrazhnov, A. Naumov, A. Kosyakov, S. Berezin, V. Volkov, A. Sergeeva, The Iron Sulfides Crystal Growth from the Halide Melts, Mater. Res. (2018), https://doi.org/10.1590/1980-5373-mr-2017-0648.

[31] P. Prabukanthan, S. Thamaraiselvi, G. Harichandran, Single step electrochemical deposition of p-Type Undoped and Co 2+ doped FeS2 thin films and performance in heterojunction solid solar cells, J. Electrochem. Soc. (2017), https://doi.org/10.1149/2.0991709jes.

[32] H. Ning, Z. Liu, Y. Xie, H. Huang, CoS2 coatings for improving thermal stability and electrochemical performance of FeS2 cathodes for thermal batteries, J. Electrochem. Soc. (2018), https://doi.org/10.1149/2.0321809jes.

[33] C.M. Eggleston, J.-.J. Ehrhardt, W. Stumm, Surface structural controls on pyrite oxidation kinetics; an XPS-UPS, STM, and modeling study, Am. Mineral. (1996) 81, https://doi.org/10.2138/am-1996-9-1002.

[34] M. Fantauzzi, B. Elsener, D. Atzei, A. Rigoldi, A. Rossi, Exploiting XPS for the identification of sulfides and polysulfides, RSC Adv 5 (2015), https://doi.org/10.1039/C5RA14915K.

[35] P. Behra, P. Bonnissel-Gissinger, M. Alnot, R. Revel, J.J. Ehrhardt, XPS and XAS Study of the Sorption of Hg(II) onto Pyrite, Langmuir (2001) 17, https://doi.org/10.1021/la0014510.

[36] A.P. Grosvenor, B.A. Kobe, M.C. Biesinger, N.S. McIntyre, Investigation of multiplet splitting of Fe 2p XPS spectra and bonding in iron compounds, Surf. Interface Anal. 36 (2004), https://doi.org/10.1002/sia.1984.

[37] G. Senanayake, The cyanidation of silver metal: review of kinetics and reaction mechanism, Hydrometallurgy (2006) 81, https://doi.org/10.1016/j.hydromet.2005.12.001.

[38] Z. Mutlu, B. Debnath, S. Su, C. Li, M. Ozkan, K.N. Bozhilov, R.K. Lake, C.S. Ozkan, Chemical vapor deposition and phase stability of pyrite on SiO$_2$, J. Mater. Chem. C. (2018) 6, https://doi.org/10.1039/C8TC00584B.

[39] R. Steudel, Liquid sulfur, in: R. Steudel (Ed.), Elemental Sulfur and Sulfur-Rich Compounds I, Springer-Verlag, 2003, pp. xx–yy, https://doi.org/10.1007/b12115.

[40] Y. Sato, M. Fukasawa, T. Yamamura, Viscosities of molten alkali-metal bromides and iodides, Int. J. Thermophys. (1997), https://doi.org/10.1007/BF02575253.

[41] M. Limpinsel, Ph.D. Thesis, University of California, Irvine, 2015.

[42] P.P. Altermatt, T. Kiesewetter, K. Ellmer, H. Tributsch, Specifying targets of future research in photovoltaic devices containing pyrite (FeS2) by numerical modelling, Sol. Energy Mater. Sol. Cells. (2002), https://doi.org/10.1016/S0927-0248(01)00053-8.

[43] W.M.H. Sachtler, G.J.H. Dorgelo, A.A. Holscher, The work function of gold, Surf. Sci. (1966), https://doi.org/10.1016/0039-6028(66)90083-5.

[44] G.N. Derry, Z. Ji-Zhong, Work function of Pt(111), Phys. Rev. B. (1989), https://doi.org/10.1103/PhysRevB.39.1940.

[45] G. Willeke, O. Blenk, C. Kloc, E. Bucher, Preparation and electrical transport properties of pyrite (FeS2) single crystals, J. Alloys Compd. (1992), https://doi.org/10.1016/0925-8388(92)90260-G.

ELSEVIER

Check for updates

Pyrite as promising monograin layer solar cell absorber material for *in-situ* solar cell fabrication on the Moon

Katriin Kristmann [a],[*], Taavi Raadik [a], Mare Altosaar [a], Maarja Grossberg-Kuusk [a], Jüri Krustok [a],[b], Maris Pilvet [a], Valdek Mikli [a], Marit Kauk-Kuusik [a], Advenit Makaya [c]

[a] *Department of Materials and Environmental Technology, Tallinn University of Technology, Ehitajate Tee 5, 19086, Tallinn, Estonia*
[b] *Division of Physics, Tallinn University of Technology, Ehitajate Tee 5, 19086 Tallinn, Estonia*
[c] *European Space Research and Technology Centre (ESTEC), Keplerlaan 1, 2201 AZ, Noordwijk, the Netherlands*

ABSTRACT

Reliable energy sources are needed in order to keep a Lunar Base on the run, and solar energy is one of the most attractive options. There are two ways to achieve it – to bring necessary solar panels from the Earth or find a way to produce them *in-situ* on the Moon from local resources. We propose the monograin layer (MGL) solar cell technology, that could be used for the *in-situ* production of solar panels on the Moon. One of the most promising compounds, that can be used as an absorber material in a monograin layer solar cell is pyrite FeS_2. There are considerable amounts of iron and sulphur in the lunar regolith. Conditions for the synthesis-growth of FeS_2 monograin powders were found and are presented in this study. The synthesis-growth of FeS_2 powder at 740 °C in potassium iodide for one week followed by slow cooling to 575 °C and rapid cooling to the room temperature, resulted in single phase pyrite monograin powder. Powder crystals had round shape and the median size of about 50 μm was appropriate for making monograin layers. The produced FeS_2 MGLs were used as absorber layers in MGL solar cells with structure as graphite/FeS_2/NiO/TCO and in FeS_2/Pt Schottky diodes. Charge carrier concentration of 6.2×10^{16} cm^{-3} was determined from capacitance-voltage measurements of FeS_2/NiO heterostructure and 2.5×10^{17} cm^{-3} from FeS_2/Pt Schottky diode.

1. Introduction

Securing a permanent lunar outpost is among the goals for future interplanetary space flights and the exploration of Mars and further celestial objects [1,2]. Therein, establishing reliable energy supply on the Moon will define the feasibility of the mission. It is extremely practical to manage with resources that are available in the lunar soil (or regolith) to lower the price of the lunar village mission.

It is especially important to establish a reliable energy supply. Continuous photovoltaic solar energy production is possible on the Moon because some areas around the lunar south pole are constantly illuminated by the Sun [3]. Producing solar cell materials and panels *in situ* from elements of lunar regolith would be the best way to use the available resources, as the cost of sending them from Earth is extremely high [4]. This study was aimed to the *in-situ* resource utilization (ISRU) approach to produce solar energy on the Moon. One promising possibility is to use the monograin layer (MGL) solar cell technology [5–7]. MGL solar cell has a superstrate solar cell structure: *back contact/absorber/buffer/transparent conductive oxide*. The structure is glued on a supportive substrate (glass or polymer film). The MGL solar cell absorber is a monolayer of nearly unisize semiconductor powder crystals fixed in a thinner-than-crystal-size layer of epoxy (or some other polymer) (Fig. 1.) [8]. The powder crystals' surfaces are coated with a thin layer of a buffer material (ordinarily via solution deposition under continuous stirring) for creating the semiconductor *p/n* junction. After the buffer layer deposition (followed by soft heat-treatment) each covered crystal is a tiny photovoltaic cell. Therefore, the MGL technology has an advantage compared to other thin film solar cell technologies - it allows to separate (geographically) processes of absorber (powder) production from solar cell module formation. The MGL solar cell structure enables to manufacture flexible, lightweight, and cost-efficient solar panels. The technology combines advantages of high-efficiency single-crystalline material and of low-cost roll-to-roll panel production [8]. Thus, it enables to cover vast areas with minimum cost [8]. All the MGL solar cell production processes are well performable in the low pressure or vacuum environment. When the synthesis ampoules have been degassed under dynamic vacuum and sealed, then they are inserted

* Corresponding author.
E-mail address: katriin.kristmann@taltech.ee (K. Kristmann).

Declaration of competing interest

The authors declare that they have no known competing financial interests or personal relationships that could have appeared to influence the work reported in this paper.

Acknowledgements

References

[1] M. Braun, N.G. Veronica Trivino, S. Hosseini, R. Schonenborg, M. Landgraf, Human lunar return: an analysis of human lunar exploration scenarios within the upcoming decade, Acta Astronaut. (2020), https://doi.org/10.1016/j.actaastro.2020.03.037.

[2] J.N. Rasera, J.J. Cilliers, J.A. Lamamy, K. Hadler, The beneficiation of lunar regolith for space resource utilisation: a review, Planet. Space Sci. (2020), https://doi.org/10.1016/j.pss.2020.104879.

[3] M. Braun, N.G. Veronica Trivino, S. Hosseini, R. Schonenborg, M. Landgraf, Human lunar return: an analysis of human lunar exploration scenarios within the upcoming decade, Acta Astronaut. (2020), https://doi.org/10.1016/j.actaastro.2020.03.037.

[4] N.J. Bennett, D. Ellender, A.G. Dempster, Commercial viability of lunar in-situ resource utilization (ISRU), Planet. Space Sci. (2020), https://doi.org/10.1016/j.pss.2020.104842.

[5] M. Altosaar, et al., Monograin Layer Solar Cells, 2003, https://doi.org/10.1016/S0040-6090(03)00167-6.

[6] E. Mellikov, et al., Monograin materials for solar cells, Sol. Energy Mater. Sol. Cell. (2009), https://doi.org/10.1016/j.solmat.2008.04.018.

[7] E. Mellikov, et al., Growth of CZTS-based monograins and their application to membrane solar cells, in: Copper Zinc Tin Sulfide-Based Thin-Film Solar Cells, 2015, https://doi.org/10.1002/9781118437865.ch13.

[8] C. Leiner, C. Sommer, V. Satzinger, L. Plessing, G. Peharz, CPV Membranes Made by Roll-To-Roll Printing: A Feasible Approach?, 2016, https://doi.org/10.1063/1.4962100.

[9] T. Raadik, Adapting Crystalsol Product to a Moon Environment, ESA GSTP Small Studies, 2016. https://www.esa.int/Enabling_Support/Space_Engineering_Technology/Shaping_the_Future/Adapting_Crystalsol_product_to_a_moon_environment.

[10] D.E. Wilhelms, Lunar stratigraphy and sedimentology, Icarus (1977), https://doi.org/10.1016/0019-1035(77)90020-3.

[11] G.A. Landis, Materials refining on the Moon, Acta Astronaut. (2007), https://doi.org/10.1016/j.actaastro.2006.11.004.

[12] J.M.D. Day, E.M.M.E. van Kooten, B.A. Hofmann, F. Moynier, Mare basalt meteorites, magnesian-suite rocks and KREEP reveal loss of zinc during and after lunar formation, Earth Planet Sci. Lett. (2020), https://doi.org/10.1016/j.epsl.2019.115998.

[13] M. Rahman, G. Boschloo, A. Hagfeldt, T. Edvinsson, On the mechanistic understanding of photovoltage loss in iron pyrite solar cells, Adv. Mater. (2020), https://doi.org/10.1002/adma.201905653.

[14] C. Steinhagen, T.B. Harvey, C.J. Stolle, J. Harris, B.A. Korgel, Pyrite nanocrystal solar cells: promising, or fool's gold? J. Phys. Chem. Lett. (2012) https://doi.org/10.1021/jz301023c.

[15] M. Limpinsel, M. Limpinsel, Iron Pyrite Absorbers for Solar Photovoltaic Energy Conversion, Irvine, 2015, 2015.

[16] M. Rahman, G. Boschloo, A. Hagfeldt, T. Edvinsson, On the mechanistic understanding of photovoltage loss in iron pyrite solar cells, Adv. Mater. (2020), https://doi.org/10.1002/adma.201905653.

[17] M.Z. Rahman, T. Edvinsson, What is limiting pyrite solar cell performance? Joule 3 (10) (Oct. 16, 2019) 2290–2293, https://doi.org/10.1016/j.joule.2019.06.015. Cell Press.

[18] M. Law, Pyrite Iron Sulfide Solar Cells Made from Solution, 2017. Irvine.

[19] M. Limpinsel, Iron Pyrite Absorbers for Solar Photovoltaic Energy Conversion, 2015. IRVINE.

[20] X. Zhang, et al., Potential resolution to the doping puzzle in iron pyrite: carrier type determination by Hall effect and thermopower, Phy. Rev. Mat. 1 (1, Jun. 2017), https://doi.org/10.1103/PhysRevMaterials.1.015402.

[21] M. Limpinsel, et al., An inversion layer at the surface of n-type iron pyrite, Energy Environ. Sci. 7 (6) (2014), https://doi.org/10.1039/c3ee43169j.

[22] M. Rahman, G. Boschloo, A. Hagfeldt, T. Edvinsson, On the mechanistic understanding of photovoltage loss in iron pyrite solar cells, Adv. Mater. 32 (26, Jul. 2020), https://doi.org/10.1002/adma.201905653.

[23] L.A. Taylor, K.L. Williams, Cu-Fe-S Phases in Lunar Rocks, 1973. Stanford, California.

[24] A.E. Saal, E.H. Hauri, Large Sulfur Isotope Fractionation in Lunar Volcanic Glasses Reveals the Magmatic Differentiation and Degassing of the Moon, Providence, USA, 2021 [Online]. Available: https://www.science.org.

[25] A.S. McEwen, M.S. Robinson, Mapping of the Moon by clementine, Adv. Space Res. 19 (10) (Jan. 1997) 1523–1533, https://doi.org/10.1016/S0273-1177(97)00365-7.

[26] J. Ciążela, M. Ciążela, D. Marciniak, G. Pasławski, MIRORES) Multiplanetary Far-Infrared Spectrometer for Prospecting Deposit Minerals, Institute of Geological Sciences, Polish Academy of Sciences, 2017.

[27] R.V. Morris, Origins and size distribution of metallic iron particles in the lunar regolith, Geochem. Cosmochim. Acta 2 (1980) 1697–1712. Supplement.

[28] D. Vaniman, D. Pettit, G. Heiken, Uses of Lunar Sulfur, 1992.

[29] A. Colaprete, et al., Detection of water in the LCROSS ejecta plume, Science 330 (6003) (1979) 463–468, https://doi.org/10.1126/science.1186986. Oct. 2010.

[30] D. Vaniman, D. Pettit, G. Heiken, Uses of lunar sulfur, in: 2nd Conference on Lunar Bases and Space Activities, 1992, pp. 429–435.

[31] M. Altosaar, et al., Monograin Layer Solar Cells, 2003, https://doi.org/10.1016/S0040-6090(03)00167-6.

[32] D. Shishin, E. Jak, S.A. Decterov, Critical assessment and thermodynamic modeling of the Fe-O-S system, J. Phase Equilibria Diffus. (2015), https://doi.org/10.1007/s11669-015-0376-4.

[33] O.K. von Goldbeck, IRON—Binary Phase Diagrams (1982), https://doi.org/10.1007/978-3-662-08024-5.

[34] Y.-H. Chen, et al., Using the high-temperature phase transition of iron sulfide minerals as an indicator of fault slip temperature, Sci. Rep. 9 (1) (Dec. 2019) 7950, https://doi.org/10.1038/s41598-019-44319-8.

[35] Y. Akaltun, T. Çayır, Fabrication and characterization of NiO thin films prepared by SILAR method, J. Alloys Compd. 625 (Mar. 2015), https://doi.org/10.1016/j.jallcom.2014.10.194.

[36] P.P. Altermatt, T. Kiesewetter, K. Ellmer, H. Tributsch, Specifying targets of future research in photovoltaic devices containing pyrite (FeS2) by numerical modelling, Sol. Energy Mater. Sol. Cell. 71 (2) (Feb. 2002) 181–195, https://doi.org/10.1016/S0927-0248(01)00053-8.

[37] H. Xian, et al., Hydration induced bandgap shift at pyrite-water interface, Appl. Phys. Lett. 113 (12) (Sep. 2018) 123901, https://doi.org/10.1063/1.5048542.

[38] K.P. Bhandari, et al., Iron pyrite nanocrystal film serves as a copper-free back contact for polycrystalline CdTe thin film solar cells, Sol. Energy Mater. Sol. Cell. 140 (Sep. 2015) 108–114, https://doi.org/10.1016/j.solmat.2015.03.032.

[39] L. Wu, et al., Enhanced photoresponse of FeS2 films: the role of marcasite-pyrite phase junctions, Adv. Mater. 28 (43, Nov. 2016), https://doi.org/10.1002/adma.201602222.

[40] F. Gossenberger, T. Roman, K. Forster-Tonigold, A. Groß, Change of the work function of platinum electrodes induced by halide adsorption, Beilstein J. Nanotechnol. 5 (Feb. 2014) 152–161, https://doi.org/10.3762/bjnano.5.15.

[41] H. Vogt, T. Chattopadhyay, H.J. Stolz, Complete first-order Raman spectra of the pyrite structure compounds FeS2, MnS2 AND SiP2, J. Phys. Chem. Solid. (1983), https://doi.org/10.1016/0022-3697(83)90124-5.

[42] A.N. Utyuzh, Influence of temperature on Raman spectra of the FeS2 single crystal with pyrite structure, Phys. Solid State (2014), https://doi.org/10.1134/S1063783414100321.

[43] A. Zavrazhnov, A. Naumov, A. Kosyakov, S. Berezin, V. Volkov, A. Sergeeva, The iron sulfides crystal growth from the halide melts, Mater. Res. (2018), https://doi.org/10.1590/1980-5373-mr-2017-0648.

[44] P. Prabukanthan, S. Thamaraiselvi, G. Harichandran, Single step electrochemical deposition of p-type undoped and Co 2+ doped FeS 2 thin films and performance in heterojunction solid solar cells, J. Electrochem. Soc. (2017), https://doi.org/10.1149/2.0991709jes.

[45] H. Ning, Z. Liu, Y. Xie, H. Huang, CoS 2 coatings for improving thermal stability and electrochemical performance of FeS 2 cathodes for thermal batteries, J. Electrochem. Soc. (2018), https://doi.org/10.1149/2.0321809jes.

[46] K.K. Mishra, K. Osseo-Asare, Fermi Level Pinning at Pyrite (FeS2)/Electrolyte Junctions, 1992.

[47] Z. Shi, A.H. Jayatissa, Preparation and characterization of cobalt-doped iron pyrite (FeS2) thin films, Prog. Nat. Sci.: Mater. Int. 30 (3, Jun. 2020), https://doi.org/10.1016/j.pnsc.2020.03.002.

[31]. Precursors FeS and S were weighted considering the formation of stoichiometric FeS$_2$, mixed with KI, and loaded into a quartz ampoule. After degassing and heating up to approximately 80 °C, the ampoule was sealed and heated in a furnace up to 740 °C. It was kept at this temperature for one week. Then the furnace with ampoule was slowly cooled to 575 °C to ensure the pure FeS$_2$ pyrite phase in accordance with the published iron-sulphur phase diagrams [32,33]. This step is important, because iron and sulphur, in addition to pyrite, have an abundance of different compositions above sulphur melting temperature [34]. The furnace was kept at 575 °C for 24 h. After that the ampoule was cooled rapidly by quenching in water. As KI is water-soluble, leaching with DI water under ultrasonic agitation was used to release FeS$_2$ crystals from solid KI flux. Powders were rinsed multiple times until washing water remained clear and transparent. Reliability of the synthesis-growth process was confirmed by repeating it several times. The produced FeS$_2$ powder samples were very similar to each other and had a uniformly high quality.

2.2. Deposition and properties of NiO buffer layer

As synthesized pyrite FeS$_2$ microcrystals exhibited *n*-type conductivity detected by hot probe method, a *p*-type partner was needed for *p/n* junction formation. NiO was chosen as an option for the buffer layer, as it is a common *p*-type semiconductor material with a wide bandgap in the range of 3.6–4.0 eV [35] and utilizes abundant nontoxic elements that are readily available in the lunar soil [10]. NiO buffer layer was deposited by the successive ionic layer adsorption and reaction (SILAR) method from NiSO$_4$ solution at room temperature (RT). NiO deposition was based on the recipe proposed by Akaltun et al. [35] that utilized a 0.1 M Ni^{2+} solution and hot water (85 °C) for NiO formation. Ni^{2+} ions in this solution were in complex with NH$_4^+$ ions, while the ratio of [Ni^{2+}] to [NH$_4^+$] was equal to 1:10. The NiO deposition from 0.1 M Ni^{2+} solution was fast and the deposited layers had cracks. Therefore, the NiSO$_4$ solution was diluted to 0.02 M to achieve thinner films with better coherence. [Ni^{2+}]: [NH$_4^+$] equal to 1:10 was kept constant and different deposition cycles of SILAR (20, 40 and 60 cycles) were applied for depositing films of different thickness, having continuous coverage and high transmittance.

2.3. Production of FeS$_2$ Schottky diodes and solar cells

Schottky diodes were prepared to measure the current-voltage characteristics and determine the pyrite crystals' work function and Fermi level. Various experimental measurements on pyrite's work function have reported different values between 3.9 eV [36] and 4.8–5.4 eV [37–39]. The work function of platinum is reported in the range of 5.6 eV–6.1 eV [40] and thus considered as a suitable metal junction partner for pyrite.

The FeS$_2$ monograin membranes for Schottky diodes and FeS$_2$/NiO hetero-structures were made from sieved FeS$_2$. The size fraction of 45–56 μm was used. Powder crystals were halfway embedded into a thin layer of epoxy leaving upper half of the crystals nondetached with epoxy and then covered with a junction partner material – metal or semiconductor. Pt layer was deposited by sputtering, NiO was deposited by the SILAR method.

2.4. Characterization of FeS$_2$ microcrystals and NiO films

The phase composition of the synthesized FeS$_2$ powders was studied by X-ray diffraction (XRD) and by Raman spectroscopy. For Raman studies, the Horiba's LabRam HR800 spectrometer equipped with a multichannel CCD detection system in the backscattering configuration was used. 532 nm laser line with spot size of 5 mm was applied for excitation. XRD patterns were recorded on a Rigaku Ultima IV diffractometer with Cu K$_\alpha$ radiation (λ = 1.5406 Å) operated at 40 kV and 40 mA in the 2θ range from 20 to 70° with a step of 0.002° and scanning

rate of 5° per minute. PDXL 2 software was used for the derivation of crystal structure information from the recorded XRD data. The chemical composition of powders was determined by energy dispersive X-ray spectroscopy (EDX) using Bruker Esprit 1.8 system. EDX analysis was performed over the crystals' surface to investigate the elemental distribution and compositional uniformity of different microcrystals. Several crystals' surfaces and bulk compositions were measured by a highly focused probe, EDX mapping was performed over large area of several crystals, mapping concluded the same results as from the single grain measurements. The morphology of crystals was studied with the high-resolution scanning electron microscope (HR-SEM) Zeiss ULTRA 55 with an accelerating voltage of 20 kV using a Röntec EDX XFlash 3001 detector.

Conductivity type of the material was determined by the hot probe method, where a sample crystal is placed between two indium probes. One probe is heated while the other stays at room temperature. The thermally excited free charge carriers will move by diffusion from the hot probe to the cold probe. These majority carriers define the electrical potential sign in the multimeter. The hot probe measurements were carried out for only a single grain at a time and not for the MGL membrane, to measure the conductivity of the FeS$_2$ single microcrystal. We tested multiple grains and the result was similar for all measurements.

2.5. Characterization of Schottky diodes and solar cells

To evaluate the main electrical characteristics of our devices, the current-voltage characteristics were measured under dark conditions and under illumination AM 1.5 G (100 mW/cm2) using a Newport Class AAA solar simulator system. I–V characteristics were recorded by a Keithley 2400 source meter.

Charge carrier density of the pyrite in devices was determined from capacitance-voltage measurements using Wayne Kerr 6500B potentiostat at different frequencies between 0.01 MHz and 10 MHz.

3. Results and discussion

3.1. Synthesis-growth of FeS2 crystals in KI flux

The FeS$_2$ powder was synthesized from FeS and S (see the previous chapter) in KI as flux at 740 °C for one week. Formed crystals had a uniform round shape and smooth surfaces (see Fig. 2) – the morphology is suitable for monograin layer production. Roughly half of the gained powder material was in the desired size fraction of around 50 μm.

3.2. Raman, EDX and XRD results

Raman spectra of microcrystals synthesized in KI at 740 °C can be seen in Fig. 3. Raman peaks at 343, 379 and weak peaks at 350 and 430 cm^{-1} are characteristic to the pyrite phase as reported in the literature [41,42]. Based on Raman analysis (Fig. 3) it can be concluded that the synthesis-growth of FeS$_2$ powder at 740 °C in KI followed by slow cooling to 575 °C resulted in pure FeS$_2$ pyrite phase. The formation of the secondary unwanted iron sulphide phases can be avoided if to proceed at high temperatures, provide the conditions for phase transition,
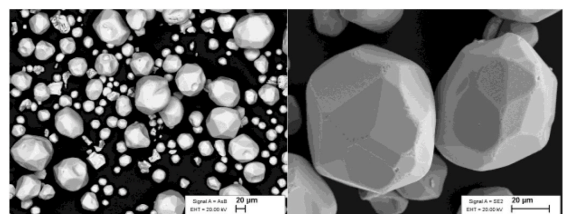

Fig. 2. SEM images of FeS$_2$ crystals synthesized in KI flux at 740 °C.
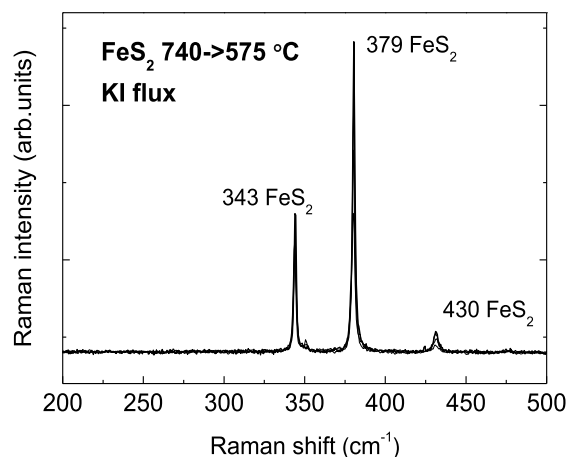
Fig. 3. Raman spectra of FeS$_2$ crystals synthesized at 740 °C in KI flux.

quench the material quickly and use a flux material that can be removed by leaching and rinsing with water.

According to the EDX results crystals synthesized at 740 °C had average composition of 33.71 at. % iron and 66.29 at. % sulphur.

The crystal structure of the microcrystals synthesized at 740 °C were analysed by XRD. The XRD pattern is presented in Fig. 4. The recorded lattice parameters a = b = c = 5.4154 Å confirm the cubic structure and are in good accordance with values reported in the literature [43–45]. Additionally, XRD and Raman results are in good correlation that there are no secondary phases in the synthesized crystals.

3.3. Electrical properties of the pyrite devices

Pyrite based Schottky diodes with Pt as junction partner were studied to assess the creation of a rectifying junction.

I–V curve of the structure of FeS$_2$/Pt is presented in Fig. 5 (blue line). It can be seen from the shape of I–V curve that a small rectifying junction is formed. However, the determination of the built-in voltage (V_{bi}) from these measurements was not possible. The performance of the pyrite-
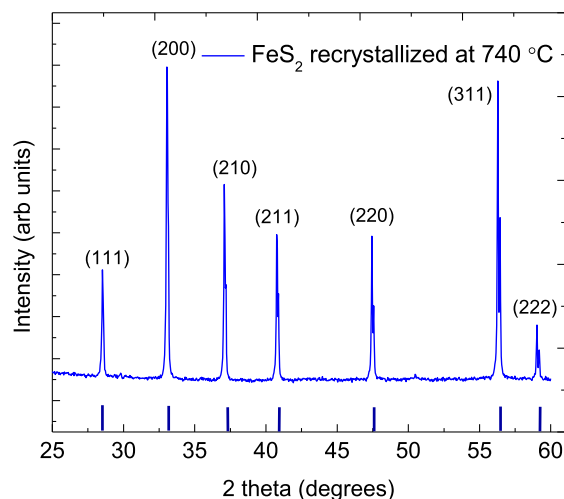

Fig. 4. XRD pattern of FeS$_2$ powders synthesized at 740 °C in KI flux.
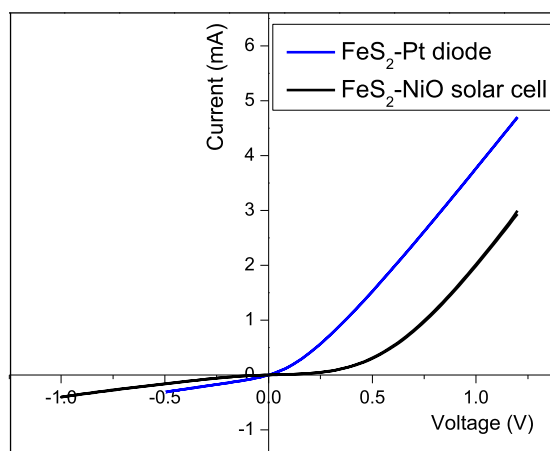

Fig. 5. I–V curves of pyrite Schottky diode with Pt as junction partner (blue) and FeS$_2$/NiO heterojunction solar cell (black). (For interpretation of the references to colour in this figure legend, the reader is referred to the Web version of this article.)

based diodes might have been limited due to Fermi level pinning, which has been attributed to the pyrite interface as a limiting factor for fabricating efficient pyrite-metal junctions [46].

I–V curve of pyrite-FeS$_2$/NiO hetero-structure is seen in Fig. 5 (black). It is obvious that a junction between the pyrite and NiO deposited by SILAR (20 cycles) has been formed but no photocurrent is generated in this solar cell structure. The existence of the pinholes or defects on pyrite crystals' surfaces could be responsible for the leakage current in reverse bias. Future studies are needed to improve the working ability of the pyrite MGL solar cell structure.

Charge carrier concentrations found from C–V measurements were 6.2×10^{16} cm^{-3} for FeS$_2$/NiO hetero-structures and 2.5×10^{17} cm^{-3} for FeS$_2$/Pt Schottky diodes. These results are in good accordance with the expected values based on literature data [47].

4. Conclusions

FeS$_2$ monograin powder was considered as an option for the absorber material in MGL solar cells for energy production in a future lunar habitat. In this work, the conditions for FeS$_2$ microcrystalline (monograin) powders by synthesis-growth method and a cooling procedure for retaining the pyrite phase of FeS$_2$ without formation of additional phases were found. Synthesis of FeS$_2$ from FeS and S was performed at 740 °C in molten KI for one week. Slow cooling to 575 °C and keeping the ampoule at this temperature for 24 h followed by rapid cooling to room temperature resulted in single phase pyrite monograin powder. Produced FeS$_2$ had cubic structure with lattice parameters a = b = c = 5.4154 Å characteristic to the pyrite phase of FeS$_2$. Raman analysis (supported by XRD data) confirmed the pure pyrite phase. Powder crystals had round shape and *n-type* conductivity. Nearly half of the gained powder material was in the crystal size fraction of around 50 μm. Schottky diodes with Pt as junction partner showed a rectifying junction. First solar cells based on pyrite monograin powder in monograin layer design were assembled with *p*-type NiO. The pyrite/NiO device showed a formation of rectifying junction between the materials, but no photocurrent was detected. These results may be improved by further work with surface treatments of the absorber crystals, different dopants, and pyrite junction partners.

Declaration of competing interest

The authors declare that they have no known competing financial interests or personal relationships that could have appeared to influence the work reported in this paper.

Acknowledgements

References

[1] M. Braun, N.G. Veronica Trivino, S. Hosseini, R. Schonenborg, M. Landgraf, Human lunar return: an analysis of human lunar exploration scenarios within the upcoming decade, Acta Astronaut. (2020), https://doi.org/10.1016/j.actaastro.2020.03.037.

[2] J.N. Rasera, J.J. Cilliers, J.A. Lamamy, K. Hadler, The beneficiation of lunar regolith for space resource utilisation: a review, Planet. Space Sci. (2020), https://doi.org/10.1016/j.pss.2020.104879.

[3] M. Braun, N.G. Veronica Trivino, S. Hosseini, R. Schonenborg, M. Landgraf, Human lunar return: an analysis of human lunar exploration scenarios within the upcoming decade, Acta Astronaut. (2020), https://doi.org/10.1016/j.actaastro.2020.03.037.

[4] N.J. Bennett, D. Ellender, A.G. Dempster, Commercial viability of lunar in-situ resource utilization (ISRU), Planet. Space Sci. (2020), https://doi.org/10.1016/j.pss.2020.104842.

[5] M. Altosaar, et al., Monograin Layer Solar Cells, 2003, https://doi.org/10.1016/S0040-6090(03)00167-6.

[6] E. Mellikov, et al., Monograin materials for solar cells, Sol. Energy Mater. Sol. Cell. (2009), https://doi.org/10.1016/j.solmat.2008.04.018.

[7] E. Mellikov, et al., Growth of CZTS-based monograins and their application to membrane solar cells, in: Copper Zinc Tin Sulfide-Based Thin-Film Solar Cells, 2015, https://doi.org/10.1002/9781118437865.ch13.

[8] C. Leiner, C. Sommer, V. Satzinger, L. Plessing, G. Peharz, CPV Membranes Made by Roll-To-Roll Printing: A Feasible Approach?, 2016, https://doi.org/10.1063/1.4962100.

[9] T. Raadik, Adapting Crystalsol Product to a Moon Environment, ESA GSTP Small Studies, 2016. https://www.esa.int/Enabling_Support/Space_Engineering_Technology/Shaping_the_Future/Adapting_Crystalsol_product_to_a_moon_environment.

[10] D.E. Wilhelms, Lunar stratigraphy and sedimentology, Icarus (1977), https://doi.org/10.1016/0019-1035(77)90020-3.

[11] G.A. Landis, Materials refining on the Moon, Acta Astronaut. (2007), https://doi.org/10.1016/j.actaastro.2006.11.004.

[12] J.M.D. Day, E.M.M.E. van Kooten, B.A. Hofmann, F. Moynier, Mare basalt meteorites, magnesian-suite rocks and KREEP reveal loss of zinc during and after lunar formation, Earth Planet Sci. Lett. (2020), https://doi.org/10.1016/j.epsl.2019.115998.

[13] M. Rahman, G. Boschloo, A. Hagfeldt, T. Edvinsson, On the mechanistic understanding of photovoltage loss in iron pyrite solar cells, Adv. Mater. (2020), https://doi.org/10.1002/adma.201905653.

[14] C. Steinhagen, T.B. Harvey, C.J. Stolle, J. Harris, B.A. Korgel, Pyrite nanocrystal solar cells: promising, or fool's gold? J. Phys. Chem. Lett. (2012) https://doi.org/10.1021/jz301023c.

[15] M. Limpinsel, M. Limpinsel, Iron Pyrite Absorbers for Solar Photovoltaic Energy Conversion, Irvine, 2015, 2015.

[16] M. Rahman, G. Boschloo, A. Hagfeldt, T. Edvinsson, On the mechanistic understanding of photovoltage loss in iron pyrite solar cells, Adv. Mater. (2020), https://doi.org/10.1002/adma.201905653.

[17] M.Z. Rahman, T. Edvinsson, What is limiting pyrite solar cell performance? Joule 3 (10) (Oct. 16, 2019) 2290–2293, https://doi.org/10.1016/j.joule.2019.06.015. Cell Press.

[18] M. Law, Pyrite Iron Sulfide Solar Cells Made from Solution, 2017. Irvine.

[19] M. Limpinsel, Iron Pyrite Absorbers for Solar Photovoltaic Energy Conversion, 2015. IRVINE.

[20] X. Zhang, et al., Potential resolution to the doping puzzle in iron pyrite: carrier type determination by Hall effect and thermopower, Phy. Rev. Mat. 1 (1, Jun. 2017), https://doi.org/10.1103/PhysRevMaterials.1.015402.

[21] M. Limpinsel, et al., An inversion layer at the surface of n-type iron pyrite, Energy Environ. Sci. 7 (6) (2014), https://doi.org/10.1039/c3ee43169j.

[22] M. Rahman, G. Boschloo, A. Hagfeldt, T. Edvinsson, On the mechanistic understanding of photovoltage loss in iron pyrite solar cells, Adv. Mater. 32 (26, Jul. 2020), https://doi.org/10.1002/adma.201905653.

[23] L.A. Taylor, K.L. Williams, Cu-Fe-S Phases in Lunar Rocks, 1973. Stanford, California.

[24] A.E. Saal, E.H. Hauri, Large Sulfur Isotope Fractionation in Lunar Volcanic Glasses Reveals the Magmatic Differentiation and Degassing of the Moon, Providence, USA, 2021 [Online]. Available: https://www.science.org.

[25] A.S. McEwen, M.S. Robinson, Mapping of the Moon by clementine, Adv. Space Res. 19 (10) (Jan. 1997) 1523–1533, https://doi.org/10.1016/S0273-1177(97)00365-7.

[26] J. Ciążela, M. Ciążela, D. Marciniak, G. Pasławski, MIRORES) Multiplanetary Far-Infrared Spectrometer for Prospecting Deposit Minerals, Institute of Geological Sciences, Polish Academy of Sciences, 2017.

[27] R.V. Morris, Origins and size distribution of metallic iron particles in the lunar regolith, Geochem. Cosmochim. Acta 2 (1980) 1697–1712. Supplement.

[28] D. Vaniman, D. Pettit, G. Heiken, Uses of Lunar Sulfur, 1992.

[29] A. Colaprete, et al., Detection of water in the LCROSS ejecta plume, Science 330 (6003) (1979) 463–468, https://doi.org/10.1126/science.1186986. Oct. 2010.

[30] D. Vaniman, D. Pettit, G. Heiken, Uses of lunar sulfur, in: 2nd Conference on Lunar Bases and Space Activities, 1992, pp. 429–435.

[31] M. Altosaar, et al., Monograin Layer Solar Cells, 2003, https://doi.org/10.1016/S0040-6090(03)00167-6.

[32] D. Shishin, E. Jak, S.A. Decterov, Critical assessment and thermodynamic modeling of the Fe-O-S system, J. Phase Equilibria Diffus. (2015), https://doi.org/10.1007/s11669-015-0376-4.

[33] O.K. von Goldbeck, IRON—Binary Phase Diagrams (1982), https://doi.org/10.1007/978-3-662-08024-5.

[34] Y.-H. Chen, et al., Using the high-temperature phase transition of iron sulfide minerals as an indicator of fault slip temperature, Sci. Rep. 9 (1) (Dec. 2019) 7950, https://doi.org/10.1038/s41598-019-44319-8.

[35] Y. Akaltun, T. Çayır, Fabrication and characterization of NiO thin films prepared by SILAR method, J. Alloys Compd. 625 (Mar. 2015), https://doi.org/10.1016/j.jallcom.2014.10.194.

[36] P.P. Altermatt, T. Kiesewetter, K. Ellmer, H. Tributsch, Specifying targets of future research in photovoltaic devices containing pyrite (FeS2) by numerical modelling, Sol. Energy Mater. Sol. Cell. 71 (2) (Feb. 2002) 181–195, https://doi.org/10.1016/S0927-0248(01)00053-8.

[37] H. Xian, et al., Hydration induced bandgap shift at pyrite-water interface, Appl. Phys. Lett. 113 (12) (Sep. 2018) 123901, https://doi.org/10.1063/1.5048542.

[38] K.P. Bhandari, et al., Iron pyrite nanocrystal film serves as a copper-free back contact for polycrystalline CdTe thin film solar cells, Sol. Energy Mater. Sol. Cell. 140 (Sep. 2015) 108–114, https://doi.org/10.1016/j.solmat.2015.03.032.

[39] L. Wu, et al., Enhanced photoresponse of FeS2 films: the role of marcasite-pyrite phase junctions, Adv. Mater. 28 (43, Nov. 2016), https://doi.org/10.1002/adma.201602222.

[40] F. Gossenberger, T. Roman, K. Forster-Tonigold, A. Groß, Change of the work function of platinum electrodes induced by halide adsorption, Beilstein J. Nanotechnol. 5 (Feb. 2014) 152–161, https://doi.org/10.3762/bjnano.5.15.

[41] H. Vogt, T. Chattopadhyay, H.J. Stolz, Complete first-order Raman spectra of the pyrite structure compounds FeS2, MnS2 AND SiP2, J. Phys. Chem. Solid. (1983), https://doi.org/10.1016/0022-3697(83)90124-5.

[42] A.N. Utyuzh, Influence of temperature on Raman spectra of the FeS2 single crystal with pyrite structure, Phys. Solid State (2014), https://doi.org/10.1134/S1063783414100321.

[43] A. Zavrazhnov, A. Naumov, A. Kosyakov, S. Berezin, V. Volkov, A. Sergeeva, The iron sulfides crystal growth from the halide melts, Mater. Res. (2018), https://doi.org/10.1590/1980-5373-mr-2017-0648.

[44] P. Prabukanthan, S. Thamaraiselvi, G. Harichandran, Single step electrochemical deposition of p-type undoped and Co 2+ doped FeS 2 thin films and performance in heterojunction solid solar cells, J. Electrochem. Soc. (2017), https://doi.org/10.1149/2.0991709jes.

[45] H. Ning, Z. Liu, Y. Xie, H. Huang, CoS 2 coatings for improving thermal stability and electrochemical performance of FeS 2 cathodes for thermal batteries, J. Electrochem. Soc. (2018), https://doi.org/10.1149/2.0321809jes.

[46] K.K. Mishra, K. Osseo-Asare, Fermi Level Pinning at Pyrite (FeS2)/Electrolyte Junctions, 1992.

[47] Z. Shi, A.H. Jayatissa, Preparation and characterization of cobalt-doped iron pyrite (FeS2) thin films, Prog. Nat. Sci.: Mater. Int. 30 (3, Jun. 2020), https://doi.org/10.1016/j.pnsc.2020.03.002.

Check for updates

Characterization of FeS_2 pyrite microcrystals synthesized in different flux media†

Katriin Kristmann, [ID] *[a] Taavi Raadik,[a] Mare Altosaar,[a] Mati Danilson, [ID] [a] Jüri Krustok,[a] Peeter Paaver[b] and Yuriy Butenko[c]

Pyrite FeS_2 has significant promise as a low-cost, earth-abundant photovoltaic material and has thus been the focus of solar energy researchers for years. Despite the effort, its efficiency has remained at around 3%, much lower than what is expected from the material properties. The inability to understand and control the effects of impurities in pyrite has increased difficulties in fabricating successful pyrite solar cells. Recent reports have shown evidence of phosphorus and cobalt as prospective dopants for improved optoelectronic properties and charge separation. Here, we demonstrate the optoelectric effects of alkali metal impurities in pyrite by synthesizing highly crystalline n-type pyrite microcrystals in different growth media. We find that the synthesis medium affects the impurity content of the final material. Alkali metals such as lithium, sodium, potassium, and cesium in pyrite are shown to create defect levels that cause the Fermi level to increase from −5.15 to −4.56 eV, depending on the amount of the impurity. Creation of solid solutions is suggested by the increased energy of the valence band maximum (E_{VBM}) from −6.17 to −5.52 eV. We show how much the concentration of these impurities can be reduced *via* recrystallization of FeS_2 crystals in molten salt to lower the energies of the E_{VBM} and Fermi levels. The effect of impurities on the photoluminescence emission of pyrite is well linked to the changes in the energy band diagram.

Introduction

Iron pyrite is the most abundant sulfide mineral. Synthetic single-crystalline and high-purity FeS_2 (iron disulfide of pyrite structure) is an n-type (S-vacancy-doped) semiconductor. Pyrite has many physical properties that are attractive for an absorber material in photovoltaic solar energy converters. Pyrite has a bandgap of 0.95 eV, a high light absorption coefficient ($>10^5$ cm^{-1}), and high carrier mobility.[1–3] These properties and the abundance of inexpensive, nontoxic constituent elements make pyrite a desirable solar energy absorber material for large-scale energy production.[4,5] It has been compared that a pyrite solar cell with only 4% efficiency could produce electricity for the same price as a 19% efficient silicon solar cell.[6] Pyrite absorbers have also been considered for extraterrestrial solar applications because of their low energy input for extraction and production, making them a great candidate for power production in the lunar base concept[7] and for the approach of space-based solar power satellites manufactured on the Moon.[8]

However, the solar energy conversion efficiencies of FeS_2-based devices have never exceeded 3%.[4,9] These low efficiencies are caused by low V_{OC} values in pyrite devices, attributed to the formation of a very thin p-type surface inversion layer on n-type pyrite crystals, which forms a leaky internal junction.[10,11] This phenomenon is more noticeable in thin films where the surface-to-bulk ratio is higher than in single crystals. There are a lot of studies in the literature that are focused on the reasons and mechanisms of this surface layer formation[11–13] and on the removal of the surface layer by chemical or electrochemical etchings.[14]

Recently, Voigt *et al.*[15] demonstrated a possibility to mitigate the internal p–n junction by fabricating metallic CoS_2 contacts *via* a process that simultaneously diffuses Co (a shallow donor) into the FeS_2 crystal, yielding direct Ohmic contact to the interior. A more recent study of the same research group[9] presents a perfect detailed overview of the research history of pyrite FeS_2 over more than 30 years and proposes to form homojunctions *via* p-type doping of single-crystalline FeS_2 with phosphorus (P). They found experimentally that the P-acceptor turns FeS_2 from n-type to p-type and allows it to form a

[a] Department of Materials and Environmental Technology, Tallinn University of Technology, Ehitajate Tee 5, 19086, Tallinn, Estonia.
E-mail: katriin.kristmann@taltech.ee

[b] Institute of Ecology and Earth Sciences, Tartu University, Ülikooli 18, 50090, Tartu, Estonia

[c] European Space Research and Technology Centre (ESTEC), Keplerlaan 1, 2201 AZ, Noordwijk, The Netherlands

† Electronic supplementary information (ESI) available. See DOI: https://doi.org/10.1039/d3ma00697b

homojunction. They determined the acceptor level at 175 ± 10 meV above the valence band maximum. This study opened the door to overcome the historical inability to understand and control the p-type doping in pyrite FeS₂ and provided new opportunities for solar cells based on this extraordinary semiconductor.[9]

In the present work, the synthesis-growth method in molten salts is used to produce FeS₂ monograin powder crystals. The individual powder particles formed in this process are mainly single crystals, as found in our previous study.[16] FeS₂ monograin powder crystals, grown in molten potassium iodide (KI), exhibited n-type conductivity, and had charge carrier concentrations around 10^{17} cm⁻³, as found from capacitance–voltage measurements of n-type FeS₂/p-type NiO heterostructures and FeS₂/Pt Schottky diodes.

For making the above-mentioned heterostructures, FeS₂ powder crystals of uniform size were fixed in a thin layer of epoxy, thus forming a monograin membrane (used also as the absorber layer in monograin membrane solar cells).[17,18] In the present study, we study the effect of different flux salts on the properties of pyrite FeS₂ crystals as the constituent elements of salts are incorporated into the FeS₂ crystals during the synthesis-growth process. The obtained different FeS₂ microcrystals fixed in the form of monograin membranes can be used as absorber layers in monograin layer (MGL) solar cells. MGL technology has not been used for pyrite solar cells before, and it has some unique advantages, such as the possibility to separate the production of absorber crystals from the preparation of the solar cell stack. The synthesis conditions (temperature and sulfur vapor pressure) of the absorber material can be accurately controlled and the process may proceed at higher temperatures than those possible in thin film technologies, thanks to monograin powder synthesis-growth in sealed quartz ampoules.[17–19]

During the synthesis of pyrite crystals in the liquid salt medium, the precursors (and their residual impurities) and the formed FeS₂ dissolve in the liquid phase up to their solubility limit at the synthesis temperature. After the formation reaction, the FeS₂ solid particles start to recrystallize and grow at the expense of the dissolved material, following the Ostwald ripening mechanism.[20] In the present study, we use different alkali metal salts in the synthesis process, and therefore there is a question about the doping of pyrite crystals with constituent elements of the used salts.

It is known that halogens in pyrite behave as donors.[21] The effects of doping with transition metals (originating in this work from FeS precursors of different purities) have also been studied previously. It was found that transition metals cause changes in the band gap energies at different doping levels.[22] Cobalt was found to increase the free electron concentration and therefore was termed as a n-type dopant,[23,24] while nickel and chrome did not affect the free electron concentration in pyrite so extensively.[23,24] It has been suggested that cobalt on an iron site (Co$_{Fe}$) is a very shallow donor and nickel on the iron site (Ni$_{Fe}$) is a very deep donor at a level around the middle of the band gap. Other metals are expected to incorporate into the

pyrite lattice *via* a substitution process.[25,26] At greater doping densities, Cr$_{Fe}$ is a deep but extremely poor donor that becomes increasingly compensated.[24] Since CrS₂ does not crystallize in the pyrite structure, it is also not beneficial to use it as a dopant. All the transition metal impurities were thought to increase the pyrite lattice constant.[22,26,27]

Group 5 and 6 nonmetal impurities have been found to occupy a vacant sulfur site. The arsenic impurity mainly affects the electronic structure at shallow and deep valence bands, while selenium and tellurium impurities were found to affect the electronic structures at deep valence bands of pyrite.[26] Based on the calculations, it was suggested that As-, Se-, and Te-substituted pyrites exhibit p-type conductivity. This agrees quite well with the experimental findings of Voigt *et al.*[9] Pyrite also has native defects and strong evidence shows that S-vacancy (V$_S$)-based native defects are present and are responsible for the unintentional bulk n-doping in pyrite crystals.[15,28] Experiments have identified an ∼225 meV deep donor and linked it to V$_S$. The doping effect of alkali metals (lithium, sodium, potassium, and cesium) in pyrite has not been sufficiently studied. However, the influence of doping with alkali metals in other semiconductor compounds has been intensively investigated. It was found that alkali doping is crucial for a wide range of chalcogenide materials used for photovoltaics (CdTe, Cu(In,Ga)Se₂, Cu₂ZnSn(S,Se)₄) and thermoelectricity (Pb(S,Se,Te)) up to superconductivity (KFeSe₂) and for two-dimensional materials (MoS₂ and WSe₂).[29] Alkali doping helped to increase the efficiency of Cu(In,Ga)Se₂ (CIGS)-based solar cells. It has been commonly agreed that doping with alkali elements passivates the defects at the p-type CIGS absorber surface or at grain boundaries. It does not change the acceptor concentration but decreases the compensating donors' concentration.[30] As the free carrier density is determined by the difference in acceptor and donor concentrations, the p-type carrier concentration increases, and as a result, the Fermi level (E_F) is lowered. Thus, an enlarged E_F difference will produce higher V_{OC} and FF values.[31]

In our previous work, we found the synthesis-growth conditions for pyrite monograin powders in molten potassium iodide (KI).[7,16] In the present work, using different flux salts, we study the effects of different alkali metal iodides on the morphology and physical properties of pyrite crystals. We determine the concentrations of flux salts' constituent elements grown into the formed pyrite crystals. We report the photoluminescence (PL) spectra of the materials and determine the Fermi levels and valence band maxima positions of FeS₂ grown in different molten alkali metal salts. We also discover a method to significantly decrease the content of Cu-impurity in the pyrite crystals, opening a discussion for the possibility to control the level of different impurities in pyrite by recrystallizing it in large amounts of a flux salt.

Experimental

Pyrite microcrystals in the monograin powder form were produced by the molten flux synthesis-growth method, and for

comparison, as a polycrystalline powder (without any added flux salt). FeS powder (3N) acquired from Thermo Scientific and S powder (5N) acquired from Alfa Aesar were used as precursors for FeS_2 synthesis. The precursors, FeS and S, were weighted in amounts necessary for the synthesis of stoichiometric FeS_2. Quartz ampoules were filled with these precursors and the respective flux materials. Different flux materials (KI, LiI, CsI and Na_2S_x, where $x > 2$) were added into individual separate ampoules to ensure the formation of liquid phase of flux during the high temperature synthesis-growth process. Flux salts were taken in amounts providing the volume of the formed liquid phase approximately equal to the volume of solid FeS_2. With this volume ratio, it is guaranteed that the solid FeS_2 powder particles, formed in the synthesis reaction, start to grow separately, which are pushed apart from each other by repulsive capillary forces.[20] For comparison, the synthesis of FeS_2 was performed without the presence of any flux material with the aim to produce FeS_2 polycrystalline powder. Later, the FeS_2 monograin powder material, originally synthesized in KI with equal volumes of liquid and solid phases ($V_{liquid KI} = V_{solid FeS_2}$), was recrystallized in four- and ten-times higher amounts of KI with the purpose of removing some impurities from pyrite by the effect of distribution of impurities between liquid and solid phases. For recrystallization, the portions of pyrite powder were loaded into quartz ampoules with 4 times ($V_{liquid KI} = 4\ V_{solid FeS_2}$) and 10 times bigger ($V_{liquid KI} = 10\ V_{solid FeS_2}$) amount of KI as the flux material. The ampoules were heated in the furnace for 10 days at 690 °C (see Table 1). To obtain even higher purity pyrite, a FeS precursor of 4N purity (instead of the previous 3N) was purchased from Apollo Scientific and used to synthesize pyrite in the KI flux ($V_{liquid KI} = V_{solid FeS_2}$). Synthesis temperatures were chosen so that the synthesis would proceed at a temperature higher than the melting point of the used flux material. The melting temperatures of KI, LiI, CsI, and Na_2S_x are 681 °C, 469 °C, 621 °C, and 400 °C, respectively.[32,33] Thus, the synthesis temperatures were set as 690 °C for the iodide salts and 475 °C for Na_2S_x flux (see Table 1, Results and discussion). All the ampoules were heated for 10 days. Fig. 1 shows the FeS_2 powder production steps and Table 1 shows the used flux salts, precursors, synthesis temperatures, and the compositions of obtained FeS_2 materials.

The materials' properties were studied using different analytical methods with the goal to use them as absorber layers in monograin layer solar cells. The chemical composition of FeS_2 powder crystals was determined via energy dispersive X-ray

spectroscopy (EDX) using a Bruker Esprit 1.8 system. The morphology of crystals was studied using the high-resolution scanning electron microscope (HR-SEM), Zeiss ULTRA 55. The phase composition of the synthesized FeS_2 powders was confirmed using X-ray diffraction (XRD) and Raman spectroscopy methods. Raman spectra were recorded using the Horiba LabRam HR800 spectrometer equipped with a multichannel CCD detection system in the backscattering configuration. The 532 nm laser line with a spot size of 5 μm was applied for excitation. XRD patterns were recorded on a Rigaku Ultima IV diffractometer undergoing Cu Kα radiation ($\lambda = 1.5406$ Å). PDXL 2 software was used for the derivation of crystal structure information from the recorded XRD data. Impurities in powder materials were determined by TOF-SIMS 5 using IONTOF. Oxygen etching at 2 keV was used for the negative mode measurement, while cesium etching at 0.5–1 keV was used for the positive mode. The measurements were carried out using vanadium primary ions with the ion gun working at 25 keV. Impurities' concentrations in the pyrite crystals were quantified via inductively coupled plasma mass spectroscopy (ICPMS). 0.1 g of sample material was dissolved using the Anton Paar Multiwave PRO microwave digestion system in NXF100 vessels (PTFE/TFM liner) using an acid mixture of 8 mL of HNO_3 (65%; Carl Roth, ROTIPURAN® Supra) and 2 mL of H_2O_2 (30%; Carl Roth, ROTIPURAN®). Samples were digested at 230 °C and at pressures between 45 and 50 bar. After dissolution, the samples were diluted with 2% HNO_3 solution. Elemental impurities were measured using Agilent 8800 ICPMS/MS. [7]Li, [127]I and [133]Cs were measured in NoGas mode and [23]Na, [39]K, [40]Ca, [59]Co using He collision gas on mass. [52]Cr, [60]Ni, and [63]Cu were measured in O_2 mode as $M^{16}O^+$ reaction products. Indium was used as an internal standard element added online by mixing T and NIST 1643f, which were used as references for quality control. The Fermi levels' and valence band maxima energies of materials were determined via ultraviolet photoelectron spectroscopy (UPS) using an Axis Ultra DLD photoelectron spectrometer (Kratos Analytical) fitted with a helium discharge lamp. The He discharge lamp with resonance line He(I) ($h\nu = 21.21$ eV) was used to obtain UPS spectra. For photoluminescence (PL) measurements, the FeS_2 crystals were fixed into an indium pad, placed in a closed cycle helium cryostat (Janis CCS-150) and cooled down to 8 K. The temperature was adjusted up to RT using a temperature controller (LakeShore Model 335). The beam of a semiconductor laser (532 nm) was used for PL excitation. The PL signal was focused into the computer controlled single grating monochromator Horiba Jobin Yvon FHR640 and detected using the Hamamatsu InGaAs photomultiplier tube. To prevent the pyrite surface from oxidation and thus to obtain the PL signal from pure FeS_2, the surface of FeS_2 crystals was covered with an ultrathin protective layer of ZnS[34] just after the removal of flux salt and before PL measurements. ZnS was deposited by the chemical solution deposition method. The solution for ZnS deposition contained Zn sulfate (0.1 M in solution) and thiourea (0.75 M) as precursors and sodium citrate (0.8 M) and ammonia (0.7 M) as complexing agents.[35]

Table 1 Chemical composition and synthesis conditions of FeS_2 crystals grown in different molten flux salts

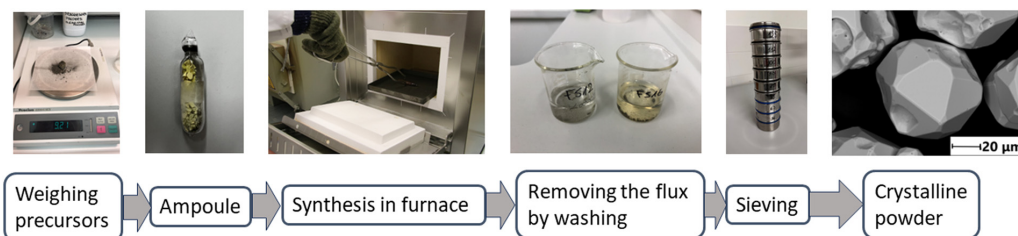| Fe/at%	S/at%	Material	Flux	Synth. T (°C)
33.5	66.5	FeS_2	KI	690
33.0	67.0	FeS_2	LiI	690
33.7	66.3	FeS_2	CsI	690
33.3	66.7	FeS_2	Na_2S_x	475
34.0	66.0	FeS_2	—	500
33.8	66.2	FeS_2	KI (4× volume)	690
33.9	66.1	FeS_2	KI (10× volume)	690
33.9	66.1	FeS_2, 4N FeS precursor	KI	690

Fig. 1 Flowchart of preparing the pyrite microcrystals in sealed ampoules.

Results and discussion

Morphology and composition

The morphology of powder crystals was studied *via* scanning electron microscopy (SEM). SEM images are shown in Fig. 2. FeS$_2$ crystals synthesized in KI, LiI and CsI have mostly round shape and smooth surfaces. All the materials that were synthesized or recrystallized in KI flux, regardless of the flux amount, were morphologically very similar to each other, and therefore not duplicated in Fig. 2. The crystal growth process can be described by the thermodynamic equilibrium formed in sealed synthesis ampoules corresponding to the synthesis conditions. In the monograin powder technology, the growth of crystals is affected not only by synthesis temperature and time but also by other different parameters such as the solubility of materials in

Fig. 2 SEM images of pyrite microcrystals synthesized in different flux media.

flux and the transport properties of components in the molten phase of the selected flux material.

When the FeS$_2$ formation reaction between S and FeS is finished, the preliminary crystallites of FeS$_2$ start to grow *via* diffusion at the expense of the dissolved material. The difference in surface energies of crystals of different sizes and at different areas of individual crystals is the only factor that drives the growth of crystals under the formed isothermal equilibrium conditions in closed ampoules; the surface energy of smaller crystals is greater than that of larger crystals, and the surface energy at grain edges and tips is higher than at plain surfaces. During the synthesis-growth process, the precursors and the formed compound dissolve in the molten liquid flux salt up to their solubility at the process temperature. If the solubility of the material in the liquid phase is high and the liquid phase is more saturated with dissolved materials, then crystal growth is faster, and crystals can grow larger during the same time period. Similarly, more roundly shaped crystals will grow if the solubility of components in the liquid phase is high.[19,20] The forming equilibrium between liquid and solid phases in the FeS$_2$ synthesis-growth process is not studied yet.

Some irregularly shaped agglomerates, which were sintered to each other, were also detected among the individual crystals. Before the melting of the flux salt, the sintering of precursors' particles can occur if some substances with melting temperatures lower than that of flux exist in the initial mixture. Sintering is caused by contracting capillary forces that arise in the solid–liquid phase boundaries due to the insufficient amount of the liquid phase.[36] Sintering of precursor particles can also occur because the liquid phase of sulfur forms already at $T_{M,sulfur}$ = 112.8 °C.[37] The FeS$_2$ formation reaction consumes liquid S, its volume diminishes and allows sintering.

FeS$_2$ crystals synthesized in the presence of Na$_2$S$_x$ have an appearance similar to the polycrystalline powder particles synthesized without any flux. Both materials have tiny crystallites without any geometrical shape. The synthesis temperature (475 °C), used to synthesize pyrite in the liquid phase of Na$_2$S$_x$ flux, was lower compared to the other materials. The lower synthesis temperature might be one of the reasons why the pyrite crystals obtained from this synthesis batch were quite small, as low synthesis temperature is linked to a slower crystal growth rate. Sintering was likely the main factor that drove the growth process in the two latter materials (synthesized in Na$_2$S$_x$ and without flux).
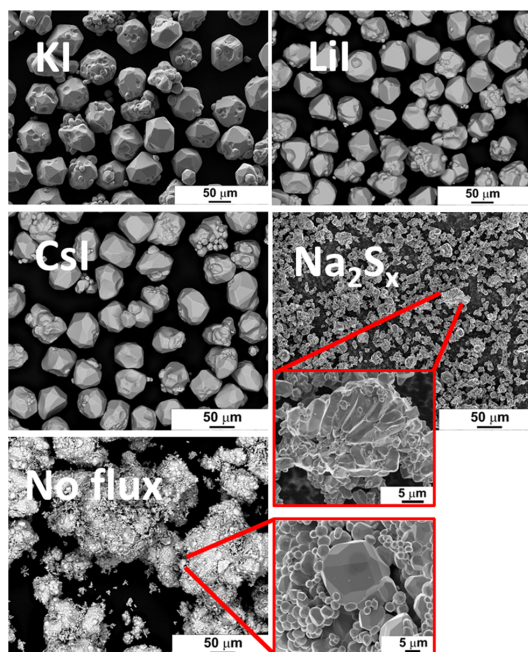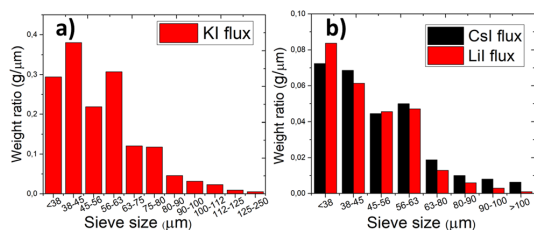
Fig. 3 Particle size distribution of FeS$_2$ materials grown in (a) KI and (b) LiI and CsI.

The particle size distribution of powders was characterized by sieving analysis. Only the materials that were obtained as monograin crystals (the ones that were synthesized in iodide salts) were analyzed and compared because the irregular shape and high agglomeration rate of materials synthesized in Na$_2$S$_x$ or without flux ruled out the possibility to characterize them by sieving analysis. The materials synthesized in KI, LiI and CsI were sieved into narrow granulometric fractions between 38 μm and 250 μm. When only one growth mechanism (Ostwald ripening) prevails, the Gaussian size distribution is predicted.[38–40] The results of sieving analysis show no significant differences in the crystals' size distribution (Fig. 3).

The elemental composition of microcrystals' bulk was determined via EDX from polished flat surfaces of powder particles fixed in epoxy because geometrical factors can interfere with the EDX results. The average atomic percentages of eight different individual crystals for each material are shown in Table 1. All materials have compositions close to the stoichiometric composition of FeS$_2$ with the Fe/S ratio of ∼0.5.

EDX spectra of all the FeS$_2$ materials are shown in the ESI.†

Phase composition and lattice parameters

X-ray diffraction (XRD) and Raman spectroscopy were used to study the phase composition of the synthesized powder crystals to evaluate the effect of different flux media. Raman spectra are presented in Fig. 4. All samples show Raman spectra with peaks belonging to the pyrite crystalline phase. Sharp peaks with narrow halfwidths indicate high crystalline quality, regardless of the used synthesis temperatures or flux salts. The Raman mode at 343 cm^{-1} belongs to the E_g symmetry with the S–S pair in liberational mode.[41] The signal at 380 cm^{-1} is the most significant Raman peak of pyrite and belongs to the A_g symmetry in-phase stretching mode of the S–S pair. A smaller peak at 430 cm^{-1} belongs to the T_g liberational and stretching mode, as does the very small peak at 350 cm^{-1}.[41,42]

The XRD diffractograms are presented in Fig. 5. Lattice parameters of the synthesized powder materials were calculated from the XRD measurements as $a = b = c = 5.4154$ Å, confirming the cubic crystal structure of all pyrite samples. As the lattice constants of all the materials (including polycrystalline FeS$_2$) fully coincide, we can conclude that the incorporation of constituent elements of the used flux salts into pyrite FeS$_2$ crystals is too low to affect the lattice parameter. These results indicate

Fig. 4 Comparison of Raman spectra of materials synthesized in different fluxes.

Fig. 5 Comparison of X-ray diffractograms of materials synthesized in different fluxes.

that it is possible to rely on the flux growth process and to use different fluxes for the synthesis of highly crystalline pyrite materials.

Concentration of impurities

In the monograin synthesis-growth process, the liquid phase of flux salt is an inexhaustible source of its constituent elements. Therefore, the concentration of a flux salt element grown into pyrite crystals as impurities is affected by the process conditions (temperature and mainly the sulfur vapor pressure in the ampoule) and is limited by the solubility of the incorporated element. On the other side, the impurities introduced by precursor materials distribute between solid and liquid phases according to their distribution coefficient. This effect is widely used in purification processes like recrystallization of

chemicals and molten zone refining of metals. Thus, iodine from iodide salts and different alkali metals (K, Na, Li and Cs) may be present in the FeS_2 crystals as doping impurities. By using the same precursors (FeS and S) in different syntheses, we can compare the concentrations of impurities originating from the different alkali metal salts. It is important to study the impact of impurities on the FeS_2 properties because the elements incorporated in the pyrite lattice affect its optoelectronic properties by introducing new energy levels for recombination.[43,44] For instance, it has been shown that chemical vapor growth in different halogens can affect even the conductivity type of pyrite crystals,[21] when they occupy the sulfur lattice sites. Metals, however, may increase carrier concentration or even induce metallic behavior.[24] The inductively coupled plasma mass spectrometry (ICPMS) analysis was used to determine the concentrations of nine different elements present in the synthesized FeS_2 materials. It was found that all materials contained transition metals, such as Cr, Co and Ni, at the level of $\sim 10^{18}$ at cm^{-3}. These concentrations are significant considering that there are 2.5×10^{22} lattice sites in 1 cm^3 of FeS_2. The contents of transition metal impurities are close to each other, indicating that they originate from the same source – the FeS precursor. The ICPMS analysis of the FeS precursors indicated that the iron mono-sulfides used in the syntheses indeed contained transition metal impurities in the range of 10^{18} at cm^{-3}, along with lithium and iodine impurities as well (the full analysis of impurities in the used precursors and flux salts is described in the ESI†). Our own experience (unpublished results) with increased Cu content in pyrite showed that a weak PL signal disappeared completely after a series of doping with Cu. Thus, copper must be a strong suppressor (killer) of photoluminescence in pyrite, which is highly undesirably.

The most significant data from the ICPMS measurements are presented in Fig. 6, while complete data are provided in the ESI.† Potassium and sodium concentrations were below their detection limit and therefore not determined, however KI and Na_2S_x salts, as K and Na sources respectively, were used in syntheses. The iodine concentration in the materials that were synthesized in metal iodide salts was quite high at around $1–4 \times 10^{19}$ cm^{-3}. The highest Li content 4×10^{19} cm^{-3} was determined in the FeS_2 material grown in LiI. Such concentration may suggest the formation of a solid solution, although the FeS_2 crystal lattice parameter was not affected, as found by

the XRD analysis of pyrite crystals. Li may also be present as a separate phase, such as LiI or Li_2S but cannot be confirmed at this point. As expected, the highest Cs concentration was determined in the material synthesized in CsI, but Cs concentration was relatively high also for another material synthesized in LiI. To understand the origin of the Cs impurity, we studied the flux salts used by ICPMS. It was found that the LiI salt contained 4.4×10^{16} cm^{-3} of Cs. This concentration is two orders of magnitude higher than it was in KI and in Na_2S_x (exact concentrations in ESI†).

It is remarkable that we could not synthesize a higher purity pyrite from a higher purity FeS (4N) precursor than from 3N purity FeS. However, we recognized that the concentrations of transition metals in the synthesized FeS_2 powder crystals were decreased, if compared with their concentrations in the precursors. Copper is one of the most problematic impurities in pyrite, and it was found that the copper content can be significantly lowered by recrystallizing pyrite in higher amounts of KI flux salt. To demonstrate the purification effect, we recrystallized the FeS_2 monograin powder (synthesized from 3N FeS in KI with volume ratio ($V_{liquid\ KI} = V_{solid\ FeS_2}$)) in 4 times and 10 times the amounts of KI flux. The concentration of different impurities was compared by ICPMS analysis and is presented in Table 2. The purification effect is strongest in the case of the Cu impurity – copper concentration decreased from 7.3×10^{17} to 3.2×10^{16} at cm^{-3} by recrystallization in KI. Chromium and lithium concentrations were somewhat lowered during the recrystallizations in higher amounts of flux, while cobalt and nickel concentrations were not decreased at all. The amount of impurity that remains in the material after recrystallization depends on the solubility of that element in the given environment. Thus, it may be easy to remove copper from pyrite using this method, but it may not be possible to remove cobalt.

The ICPMS results were confirmed qualitatively by the time-of-flight secondary ion mass spectroscopy (ToF-SIMS) measurements, shown in Fig. 7. Although the ToF-SIMS results do not provide the exact concentrations of impurities, it is still valuable to confirm the presence of the impurities detected by ICPMS measurements.

It can be seen that Cu content is at a similar level in all the measured materials. Potassium and sodium as impurities were both detected by ToF-SIMS. However, due to the sensitivity of the ToF-SIMS technique, and as the detection limit depends on the matrix as well, we expect the Na and K concentrations to be very low. Lithium as an impurity was detected in the material synthesized in LiI, as could be expected. Cesium was detected in all the materials synthesized in iodide salts, likely because all the salts included low amounts of cesium as an impurity, as confirmed by the ICPMS analysis of the flux salts.

The analysis data confirm that the constituent elements of the flux salts are incorporated into the formed pyrite crystals. Moreover, the purity of the used precursors and the flux materials affects the purity of FeS_2 crystals as well. In the next chapters, we compare the optoelectronic properties of pyrite materials synthesized in different alkali metal salts.
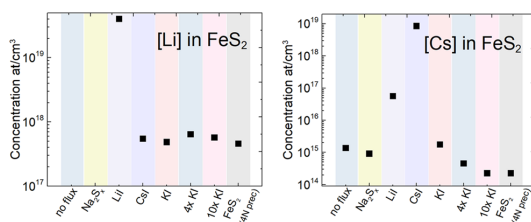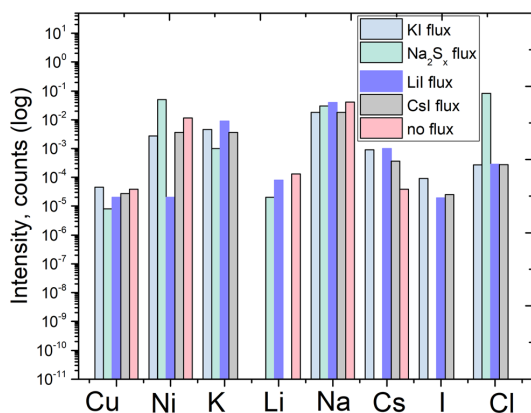

Fig. 6 Comparison of lithium and cesium concentrations found in the pyrite crystals synthesized in different alkali metal salts.

Table 2 Determined concentrations of impurities in FeS$_2$ synthesized and recrystallized in various amounts of KI flux salt

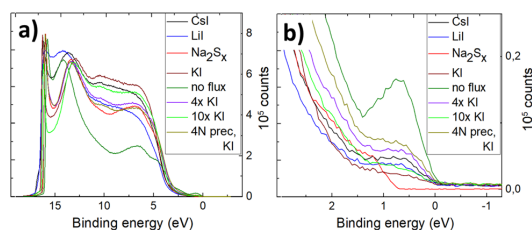| Material	Li, at cm^{-3}	Cr, at cm^{-3}	Cu, at cm^{-3}	Co, at cm^{-3}	Ni, at cm^{-3}
FeS$_2$ synthesized from the 3N FeS precursor	4.9×10^{17}	4.8×10^{18}	7.3×10^{17}	3.1×10^{18}	6.6×10^{18}
Same material recrystallized with 4× bigger amount of KI as flux	5.7×10^{17}	1.8×10^{18}	2.3×10^{17}	4.8×10^{18}	9.3×10^{18}
Same material recrystallized with 10× bigger amount of KI as flux	4.6×10^{17}	4×10^{18}	3.2×10^{16}	4.7×10^{18}	8.3×10^{18}

Fig. 7 ToF-SIMS qualitative results of pyrite synthesized in different fluxes, and qualitative comparison of elemental impurities' concentration.

Fig. 8 (a) Full He(I) UPS spectra of FeS$_2$ synthesized in different fluxes, (b) all spectra zoomed in near 0 eV binding energy.

Photoelectron spectroscopy results

It is known that the Fermi level position and electronic structure of various semiconductors can be controlled by doping.[24,43,45–48] In pyrite, Co and Ni impurities substitute for Fe and introduce bulk defect states that are deep and/or induced near the band gap edge, generated by the 2d and 3d orbitals of the metals.[47,48] In addition, halogens (F, Cl, and Br at the position of S) in the pyrite lattice cause very localized gap states close to the Fermi level in the minority spin channel, modifying pyrite electrochemical performance.[47] On the other hand, Se as an impurity in pyrite does not introduce changes in the electronic structure.[48] The results of ICPMS and ToF-SIMS measurements of pyrite samples show that all materials contain halogens, alkali metals and transition metals as impurities. The electronic structure of FeS$_2$ materials was studied by ultraviolet photoelectron spectroscopy (UPS) to determine the valence band maxima and to see the impact of impurities to our materials, also to find out if iodine has the same effect as reported for other halogens, because it is one of the primary impurities in our materials.

Surface valence band energies were obtained from the UPS measurements. A bias of −9.124 V was used to separate the analyser and the secondary edges of the sample. The bias was optimized to shift the Ag spectrum into the linear region of the analyser (kinetic energy of 0–10 eV). A spectrometer with a pass energy of 5 eV and a large area aperture of 300 μm × 700 μm was used. Under these conditions, the energy resolution of the spectra was measured at the Fermi edge of the clean Ag foil at room temperature.[49] The FeS$_2$ work function (Φ) was determined using eqn (1).[49,50]

$$\Phi = h\nu - E_{\text{cutoff}} \tag{1}$$

where $h\nu$ in eqn (1) is the He(I) line = 21.21 eV, and E_{cutoff} is the secondary electron edge of FeS$_2$ UPS spectra in the binding energy scale.

Fig. 8 shows the full He(I) UPS spectra of the pyrite microcrystals synthesized in different salt media. The UPS spectrum of the material synthesized without flux shows a low-intensity peak below the Fermi level (E_F) which is used to determine the position of the valence band maximum or E_{VBM}. The photoelectron counts (intensity on the y-axis) are proportional to the density of states at this region,[51] so the small peak may represent a very low but noteworthy density of states above the E_{VBM}. The other materials measured in this study (see Fig. 8b) show a much smaller but still visible peak near the E_F. This phenomenon in UPS measurements of pyrite was reported by Cabán-Acevedo et al.[52] but not thoroughly explained. UPS measurements of semiconductors can exhibit some ambiguity in assigning values near the E_F and at the E_{cutoff}.[51] The small peak near the 0 eV binding energy in Fig. 8b (0 eV represents the E_F) can be due to a lack of sulfur on the pyrite surface. Lack of sulfur at the outermost surface may lead to the pyrite surface turning metallic and closer to a FeS chemistry, which is too thin or "patchy" of a layer to be detected by EDX. FeS has a very narrow band gap and p-type conductivity[53] and therefore could explain the density of states above pyrite's E_{VBM}. The material with the most visible low binding energy peak was synthesized without any flux salt, showing at the same time the lowest E_{VBM} position (see Fig. 9). Variations near the E_{cutoff} which are seen at the left-hand side in Fig. 8 can be due to inhomogeneities and position of the sample surface.[51] Helander et al.[54] have proposed an origin for such effect, as arising due to electric field artifacts that can be increased when the sample plane is not perpendicular to the entrance of the energy analyzer. Our materials are in the form of microcrystalline powder, so the sample surface can be at an unpredictable angle compared to the energy analyzer. Another reason for multiple apparent E_{cutoff} values is inhomogeneities

and defects in the sample surface, which are formed due to surface roughness or a different surface chemistry.[54]

The valence band maxima were determined from pyrite spectra, leaving out the low-energy peak because it extended into the negative binding energies and did not represent the properties of pyrite. The values of E_{VBM} from the vacuum level were determined between 5.52 and 6.17 eV and are plotted in Fig. 9.

It is clearly seen that all pyrite crystals either synthesized in KI or recrystallized in the KI flux, have similar energy band structures with valence band maxima around −6.0 eV from the vacuum level, and the Fermi level energy values are also quite close to each other. The energy band diagrams are different if LiI, CsI and Na_2S_x fluxes were used in FeS_2 syntheses. The higher values of E_{VBM} in the latter cases indicate the possible formation of solid solutions at the surface with changes in the bandgap energies. The ICPMS analysis revealed the Li impurity level at 4×10^{19} and Cs at 8×10^{18} cm^{-3} in the pyrite crystals grown in LiI and CsI flux, respectively. These levels are nearly high enough to form solid solutions, however not detected yet by a change in the lattice parameters in the XRD analysis. Therefore, we suppose that solid solutions could be formed on the very top of the pyrite crystals' surfaces, detectable only by using a very surface sensitive technique like UPS, while XRD measurements reveal the bulk of the material.

The work function (Φ) values of our materials were derived from the E_{cutoff} values as shown in Fig. 8b by applying eqn (1). The Φ values varied between 4.58 and 5.11 eV for different materials. These values correlate well with the literature data, reporting pyrite work function values between 3.9 eV and 4.8–5.4 eV.[52,55–57] The energy band diagrams of the materials derived from the UPS data are plotted in Fig. 9.

According to different reports,[1,3,58] the band gap energy of pyrite is around 1 eV. Thus, there is strong indication that the measured crystals have n-type conductivity. As seen from the diagrams in Fig. 9, the measured Fermi levels are very close to the expected energy of the conduction band minimum. Pyrite crystals are well known to have n-type conductivity, while pyrite thin films often have p-type conductivity – a phenomenon known as the surface inversion of pyrite.[11,12] The energy band diagram of the polycrystalline material synthesized without flux should be closest to pure pyrite, because this material has the lowest content of impurities. The band diagram of the material recrystallized and purified in the liquid phase of potassium iodide is closest to the polycrystalline material's band diagram. This may be due to a similarly low level of Cs doping in the latter material. However, the effects of Cs doping in pyrite have not been thoroughly studied. The analysis reveals that copper impurities do not affect the band gap or E_{VBM} of pyrite, as the electronic structure is very similar for a material with a significant amount of Cu impurities (no-flux material) and a purified material that was recrystallized in $10\times$ the amount of KI flux.

Photoluminescence results

Photoluminescence spectroscopy is a proven tool to study the recombination processes in semiconductors and changes in the optoelectronic properties. The available literature offers limited insights into the photoluminescence emission characteristics and dominant recombination mechanisms of pyrite FeS_2. It is known from the literature that the pyrite surface tends to oxidize very quickly in an atmosphere that contains oxygen.[59] Our group has experienced that oxidation could diminish or even quench the PL signal of FeS_2. Therefore, we encapsulated the pyrite crystals' surfaces from the external influences by covering the synthesized crystals with a ZnS protective layer.[60] A chemical solution deposition of ZnS resulted in a layer thickness of approximately 10 nm. ZnS does not have PL emission bands between 0.8 and 1.3 eV[61] so it should not affect the pyrite PL spectra. The results of low temperature photoluminescence measurements can be seen in Fig. 10. It is seen that the PL spectra of pyrite crystals grown in different molten fluxes show very different shapes and positions for each peak, which indicates the different recombination mechanisms and the possible change in the bandgap energy. A similar effect has been shown by Ghisani et al.[40] where they studied tetrahedrite microcrystals grown in different fluxes. All the measured pyrite samples have a broad asymmetric PL peak shape that is typical for semiconductors with high defect concentrations.[62] The PL spectra were fitted using the empirical asymmetric double sigmoid function[63] to find the position of each peak. The pyrite polycrystals, synthesized without any flux, had a main peak at the lowest energy with the center at 0.83 eV. The microcrystals synthesized in KI also have a weak peak close to the polycrystalline material with an energy value of 0.85 eV. These peaks are likely to have the same origin, probably related to some deep defects. As we have already seen from the UPS measurements, the formation of a solid solution is likely in the case of Li and Cs containing pyrite crystals. The shift in the PL peak position indicates the change in the bandgap energy, while some PL bands, for example near 1.3 eV, are at notably higher energies compared to the pyrite
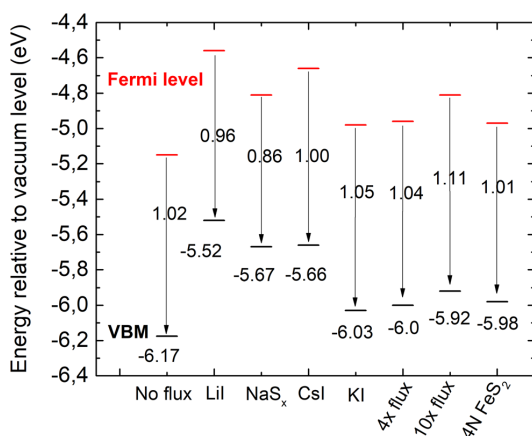

Fig. 9 Energy band diagrams of pyrite FeS_2 synthesized in different fluxes. E_{VBM} is marked in black and Fermi level energies in red.
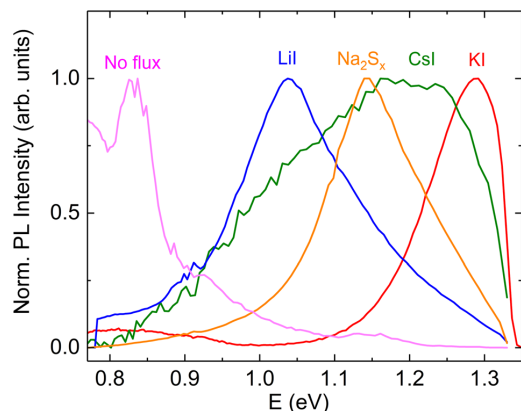
Fig. 10 Low temperature (8 K) PL spectra of pyrite crystals grown in different molten salt media.

band gap. This could be due to a quantum confinement effect[64,65] where there are some nanocrystals on the pyrite surface, which have a larger band gap compared to the bulk material. The nanocrystals on the pyrite surface might also have a different chemistry than FeS_2. The solubility of copper impurity compounds in KI is quite high.[66] Thus, there is a possibility that copper that is dissolved at synthesis temperature may precipitate onto the pyrite crystals during cooling and form chalcopyrite ($CuFeS_2$) which has a band gap larger than the pyrite bulk material.[46] The fact that we did not observe a photoluminescence signal from the materials with lowered Cu concentration may be a proof to that effect. This intriguing question will be investigated further in our future studies. In conclusion, we can say that the shift in peak positions and the change of the PL peak shape suggest an important role of the different flux materials and impurities that are introduced using the flux growth method. A thorough analysis of the origin of the PL emission in pyrite is underway by our group.

Conclusions

FeS_2 pyrite microcrystals were successfully synthesized in the molten phase of different alkali metal salts (KI, LiI, CsI, and Na_2S_x) and without the presence of any molten flux. All the materials had a highly crystalline pyrite structure with no change in the lattice parameter, as determined by XRD and Raman analyses. The synthesized materials were analyzed by ICPMS to compare the concentrations of different alkali metal impurities and iodine incorporated during the growth process. The lithium and cesium concentrations varied the most, while sodium and potassium contents were below the determination limit. The highest Li content of 4×10^{19} cm^{-3} and Cs content around 10^{19} cm^{-3} were determined in the FeS_2 materials grown in LiI and CsI, respectively. The other used alkali metal salts contained Li and Cs as residual impurities. These residual impurities also incorporated into the formed FeS_2 but at much

lower levels than from LiI and CsI. Iodine concentrations in the FeS_2 materials obtained from the used iodide salts were determined to be 1–4×10^{19} cm^{-3}. It was found that transition metal impurities at high levels originated from the FeS precursor. The different alkali metals from the used flux salts affected the energy band diagrams of pyrite FeS_2, as the materials synthesized in KI had significantly lower E_{VBM} values, while pyrite that was synthesized in LiI, CsI or Na_2S_x had all higher energies of valence band maxima. It was suggested that solid solutions might have been formed on the pyrite crystals' surfaces, which are detectable only by using the very surface sensitive UPS method.

The present study revealed a method to remove copper and lower the concentrations of other impurities from pyrite by recrystallization or its synthesis in increased amounts of flux salts by the different distribution of impurity elements between liquid and solid phases. Copper is one of the most harmful impurities in pyrite, and decreasing the contamination of copper was confirmed using the ICPMS technique.

The results of low-temperature photoluminescence measurements show a strong shift in peak positions and peak shapes of the PL spectra of materials synthesized in different fluxes, likely due to a change in the band gap values of the different materials.

Author contributions

Katriin Kristmann: conceptualization, data curation, formal analysis, investigation, visualization, writing – original draft, and writing – review & editing. Taavi Raadik: formal analysis, funding acquisition, investigation, project administration, resources, supervision, and writing – review & editing. Mare Altosaar: methodology, supervision, validation, and writing – review & editing. Mati Danilson: investigation, validation, and writing – review & editing. Jüri Krustok: methodology, validation, and writing – review & editing. Peeter Paaver: investigation. Yuriy Butenko: investigation.

Conflicts of interest

There are no conflicts to declare.

Acknowledgements

Notes and references

1 A. Ennaoui and H. Tributsch, *Sol. Cells*, 1984, **13**, 197–200.
2 M. Law, *Pyrite Iron Sulfide Solar Cells Made from Solution*, Irvine, 2017.

3 C. Steinhagen, T. B. Harvey, C. J. Stolle, J. Harris and B. A. Korgel, *J. Phys. Chem. Lett.*, 2012, **3**(17), 2352–2356.

4 S. Gohri, J. Madan, M. K. A. Mohammed and R. Pandey, *Mater. Res. Express*, 2023, **10**, 024001.

5 M. Limpinsel, PhD thesis, University of California, 2015.

6 C. Wadia, A. P. Alivisatos and D. M. Kammen, *Environ. Sci. Technol.*, 2009, **43**(6), 2072–2077.

7 K. Kristmann, T. Raadik, M. Altosaar, M. Grossberg-Kuusk, J. Krustok, M. Pilvet, V. Mikli, M. Kauk-Kuusik and A. Makaya, *Acta Astronaut.*, 2022, **199**, 420–424.

8 T. Raadik, K. Kristmann, J. Ciazela, M. Jozefowicz, M. Kowalinski, A. Sniadkowski, J. Bakala, M. Steslicki, N. Zalewska, B. Pieterek, M. Ciazela, D. Marciniak, G. Paslawski, Z. Szaforz, A. Woods and A. Makaya, *Proceedings of the International Astronautical Congress in Baku*.

9 B. Voigt, L. S. Valor, W. Moore, J. Jeremiason, J. Kakalios, E. S. Aydil and C. Leighton, *ACS Appl. Mater. Interfaces*, 2023, **15**, 28258–28266.

10 B. Voigt, W. Moore, M. Maiti, J. Walter, B. Das, M. Manno, C. Leighton and E. S. Aydil, *ACS Mater. Lett.*, 2020, **2**, 861–868.

11 M. Limpinsel, N. Farhi, N. Berry, J. Lindemuth, C. L. Perkins, Q. Lin and M. Law, *Energy Environ. Sci.*, 2014, **7**, 1974–1989.

12 S. Uchiyama, Y. Ishikawa and Y. Uraoka, *Jpn. J. Appl. Phys.*, 2018, **57**, 032301.

13 D. Ray, B. Voigt, M. Manno, C. Leighton, E. S. Aydil and L. Gagliardi, *Chem. Mater.*, 2020, **32**, 4820–4831.

14 K. Büker, N. Alonso-Vante, R. Scheer and H. Tributsch, *Ber. Bunsen-Ges.*, 1994, **98**, 674–682.

15 B. Voigt, B. Das, D. M. Carr, D. Ray, M. Maiti, W. Moore, M. Manno, J. Walter, E. S. Aydil and C. Leighton, *Phys. Rev. Mater.*, 2021, **5**, 025405.

16 K. Kristmann, M. Altosaar, J. Raudoja, J. Krustok, M. Pilvet, V. Mikli, M. Grossberg, M. Danilson and T. Raadik, *Thin Solid Films*, 2022, **743**, 139068.

17 M. Kauk-Kuusik, X. Li, M. Pilvet, K. Timmo, M. Grossberg, T. Raadik, M. Danilson, V. Mikli, M. Altosaar, J. Krustok and J. Raudoja, *Thin Solid Films*, 2018, **666**, 15–19.

18 F. Ghisani, K. Timmo, M. Altosaar, J. Raudoja, V. Mikli, M. Pilvet, M. Kauk-Kuusik and M. Grossberg, *Mater. Sci. Semicond. Process.*, 2020, **110**, 104973.

19 E. Mellikov, J. Hiie and M. Altosaar, *Int. J. Mater. Prod. Technol.*, 2007, **28**, 291–311.

20 P. W. Voorhees, Ostwald ripening of two-phase mixtures, *Annu. Rev. Mater. Sci.*, 1992, **22**, 197–215.

21 S. Fiechter, J. Mai, A. Ennaoui and W. Szacki, *J. Cryst. Growth*, 1986, **78**, 438–444.

22 S. Khalid, M. A. Malik, D. J. Lewis, P. Kevin, E. Ahmed, Y. Khan and P. O'Brien, *J. Mater. Chem. C*, 2015, **3**, 12068–12076.

23 S. W. Lehner, K. S. Savage and J. C. Ayers, *J. Cryst. Growth*, 2006, **286**, 306–317.

24 T. Salk, *Master's thesis*, University of California, 2019.

25 R. N. Chandler and R. W. Bené, *Phys. Rev. B: Solid State*, 1973, **8**, 4979–4988.

26 Y. Li, J. Chen, Y. Chen and J. Guo, *Trans. Nonferrous Met. Soc. China*, 2011, **21**, 1887–1895.

27 I. J. Ferrer, C. de la Heras and C. Sanchez, *J. Phys.: Condens. Matter*, 1995, **7**, 2115–2121.

28 X. Zhang, M. Li, J. Walter, L. O'Brien, M. A. Manno, B. Voigt, F. Mork, S. V. Baryshev, J. Kakalios, E. S. Aydil and C. Leighton, *Phys. Rev. Mater.*, 2017, **1**, 015402.

29 D. Colombara, U. Berner, A. Ciccioli, J. C. Malaquias, T. Bertram, A. Crossay, M. Schöneich, H. J. Meadows, D. Regesch, S. Delsante, G. Gigli, N. Valle, J. Guillot, B. El Adib, P. Grysan and P. J. Dale, *Sci. Rep.*, 2017, **7**, 43266.

30 F. Pianezzi, P. Reinhard, A. Chirilă, B. Bissig, S. Nishiwaki, S. Buecheler and A. N. Tiwari, *Phys. Chem. Chem. Phys.*, 2014, **16**, 8843.

31 Y. Sun, S. Lin, W. Li, S. Cheng, Y. Zhang, Y. Liu and W. Liu, *Engineering*, 2017, **3**, 452–459.

32 Y. Iwadate and T. Ohkubo, *J. Chem. Eng. Data*, 2020, **65**, 5240–5248.

33 J. Sangster and A. D. Pelton, *The Na-S (Sodium-Sulfur) System Equilibrium Diagram*, 1997, vol. 18.

34 J. D. Myers, J. A. Frantz, C. C. Baker, S. C. Erwin, S. N. Qadri, N. Bassim, S. B. Qadri, R. Y. Bekele and J. S. Sanghera, *Opt. Mater. Express*, 2018, **8**, 3835.

35 J. Liu, A. Wei and Y. Zhao, *J. Alloys Compd.*, 2014, **588**, 228–234.

36 E. Mellikov, D. Meissner, T. Varema, M. Altosaar, M. Kauk, O. Volobujeva, J. Raudoja, K. Timmo and M. Danilson, *Sol. Energy Mater. Sol. Cells*, 2009, **93**(1), 65–68.

37 R. Steudel, *Top. Curr. Chem.*, 2003, **230**, 81–116.

38 M. Kauk-Kuusik, X. Li, M. Pilvet, K. Timmo, M. Grossberg, T. Raadik, M. Danilson, V. Mikli, M. Altosaar, J. Krustok and J. Raudoja, *Thin Solid Films*, 2018, **666**, 15–19.

39 T. Bergfors, *J. Struct. Biol.*, 2003, **142**, 66–76.

40 F. Ghisani, K. Timmo, M. Altosaar, V. Mikli, M. Pilvet, R. Kaupmees, J. Krustok, M. Grossberg and M. Kauk-Kuusik, *Thin Solid Films*, 2021, **739**, 138980.

41 A. N. Utyuzh, *Phys. Solid State*, 2014, **56**, 2050–2055.

42 Z. Mutlu, B. Debnath, S. Su, C. Li, M. Ozkan, K. N. Bozhilov, R. K. Lake and C. S. Ozkan, *J. Mater. Chem. C*, 2018, **6**, 4753–4759.

43 Y. Li, J. Chen, Y. Chen and J. Guo, *Trans. Nonferrous Met. Soc. China*, 2011, **21**, 1887–1895.

44 S. W. Lehner, N. Newman, M. van Schilfgaarde, S. Bandyopadhyay, K. Savage and P. R. Buseck, *J. Appl. Phys.*, 2012, **111**(8), 083717.

45 J. Jia, A. Takasaki, N. Oka and Y. Shigesato, *J. Appl. Phys.*, 2012, **112**(1), 013718.

46 S. Ghosh, T. Avellini, A. Petrelli, I. Kriegel, R. Gaspari, G. Almeida, G. Bertoni, A. Cavalli, F. Scotognella, T. Pellegrino and L. Manna, *Chem. Mater.*, 2016, **28**, 4848–4858.

47 S. Li, Y. Zhang and X. Niu, *Phys. Chem. Chem. Phys.*, 2018, **20**, 11649–11655.

48 K. S. Savage, D. Stefan and S. W. Lehner, *Appl. Geochem.*, 2008, **23**, 103–120.

49 C. Maheu, L. Cardenas, E. Puzenat, P. Afanasiev and C. Geantet, *Phys. Chem. Chem. Phys.*, 2018, **20**, 25629–25637.

50 V. R. Koppolu, M. C. Gupta and L. Scudiero, *Sol. Energy Mater. Sol. Cells*, 2011, **95**, 1111–1118.

51 J. E. Whitten, *Appl. Surf. Sci. Adv.*, 2023, **13**, 100384.

52 M. Cabán-Acevedo, N. S. Kaiser, C. R. English, D. Liang, B. J. Thompson, H.-E. Chen, K. J. Czech, J. C. Wright, R. J. Hamers and S. Jin, *J. Am. Chem. Soc.*, 2014, **136**, 17163–17179.

53 C. Tresca, G. Giovannetti, M. Capone and G. Profeta, *Phys. Rev. B*, 2017, **95**, 205117.

54 M. G. Helander, M. T. Greiner, Z. B. Wang and Z. H. Lu, *Appl. Surf. Sci.*, 2010, **256**, 2602–2605.

55 H. Xian, R. Du, J. Zhu, M. Chen, W. Tan, R. Zhu, J. Wei and H. He, *Appl. Phys. Lett.*, 2018, **113**, 123901.

56 L. Wu, N. Y. Dzade, L. Gao, D. O. Scanlon, Z. Öztürk, N. Hollingsworth, B. M. Weckhuysen, E. J. M. Hensen, N. H. de Leeuw and J. P. Hofmann, *Adv. Mater.*, 2016, **28**(43), 9602–9607.

57 K. P. Bhandari, P. Koirala, N. R. Paudel, R. R. Khanal, A. B. Phillips, Y. Yan, R. W. Collins, M. J. Heben and R. J. Ellingson, *Sol. Energy Mater. Sol. Cells*, 2015, **140**, 108–114.

58 M. Rahman, G. Boschloo, A. Hagfeldt and T. Edvinsson, *Adv. Mater.*, 2020, **32**(26), 1905653.

59 H. W. Nesbitt, G. M. Bancroft, A. R. Pratt and M. J. Scaini, *Am. Mineral.*, 1998, **83**, 1067–1076.

60 J. D. Myers, J. A. Frantz, C. C. Baker, S. C. Erwin, S. N. Qadri, N. Bassim, S. B. Qadri, R. Y. Bekele and J. S. Sanghera, *Opt. Mater. Express*, 2018, **8**, 3835.

61 A. I. Inamdar, S. Cho, Y. Jo, J. Kim, J. Han, S. M. Pawar, H. Woo, R. S. Kalubarme, C. Park, H. Kim and H. Im, *Mater. Lett.*, 2016, **163**, 126–129.

62 M. Grossberg, T. Raadik, J. Raudoja and J. Krustok, *Curr. Appl. Phys.*, 2014, **14**, 447–450.

63 J. Krustok, H. Collan, M. Yakushev and K. Hjelt, *Phys. Scr.*, 1999, **T79**, 179.

64 G. Ramalingam, P. Kathirgamanathan, G. Ravi, T. Elangovan, B. Arjun Kumar, N. Manivannan and K. Kaviyarasu, *Quantum Confinement*, 2020.

65 M. K. Sahoo and P. Kale, *Superlattices Microstruct.*, 2021, **156**, 106949.

66 I. Leinemann, K. Timmo, M. Grossberg, T. Kaljuvee, K. Tõnsuaadu, R. Traksmaa, M. Altosaar and D. Meissner, *J. Therm. Anal. Calorim.*, 2015, **119**, 1555–1564.
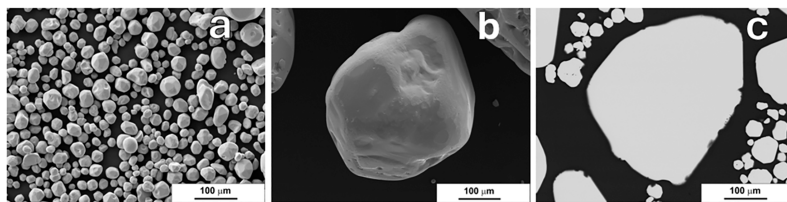
Figure 3. SEM images of FeS_2 microcrystals recrystallized with 1000 ppm phosphorus: (a, b) surface morphology and (c) cross-section of a single crystal.

portion of the pyrite crystals exhibited cracking or fragmentation, as shown in Figure 2a−d, where the different phases are evident in the SEM backscattered electron images. Energy-dispersive X-ray spectroscopy (EDX) indicated a high phosphorus composition, 20−25 atom % P, within the fragmented phase; the EDX spectra are shown in Supporting Information 1. Raman spectroscopy results are shown in Figure 2a−d. The phosphorus-rich, fragmented material showed characteristic peaks of cubic FeS_2 at 343, 350, 379, and 431 cm^{-1},[22,23] along with additional peaks at 247 and 279 cm^{-1} corresponding to iron thiophosphide phases such as $Fe_2P_2S_6$ or $FePS_3$.[24] The Raman peak at 343 cm^{-1} corresponds to the E_g Raman mode, where the sulfur atoms are displaced perpendicular to the axis of the sulfur−sulfur bond. A weak Raman peak at 350 cm^{-1} reflects the T_g phonon mode, which reflects the in-phase and out-of-phase stretching vibrations of the sulfur dimer S_2. The strong Raman peak at 379 cm^{-1} belongs to the A_g mode, which corresponds to the same stretching vibrations as the T_g mode. The Raman peak at 430 cm^{-1} is also attributed to the T_g phonon mode.[25,26]

The leafy, needle-like structure of $FePS_3$ is also seen inside the cracks of the fragmented crystals. The reason for the cracking and fragmentation is likely due to the layered structure of the $FePS_3$ phase and its different density compared to pyrite.

All the performed hot probe measurements on different crystals confirmed *n*-type conductivity as the majority carrier type. Thus, it was concluded that phosphorus vapor treatment was not suitable for doping FeS_2 crystals with P.

3.2. Recrystallization by Heat-Treatment of FeS_2 Crystals in a Mixture of KI and P. In the second series, increasing amounts of red phosphorus (10 to 1000 ppm P relative to presynthesized FeS_2, on molar basis) were mixed with the flux salt (KI) to perform phosphorus treatments on presynthesized pyrite crystals. Unlike the prior series, these treatments were conducted in a molten KI flux medium at elevated temperatures, facilitating recrystallization of the pyrite microcrystals and enabling phosphorus incorporation into the FeS_2 lattice in the recrystallization-growth process. Post-recrystallization, SEM analysis revealed no cracks or secondary phases, even for the highest P concentration, as shown in Figure 3. Raman spectra with sharp and narrow peaks at 343, 380, and 431 cm^{-1} confirm the single pyrite phase,[22,23] as shown in Figure 4.

However, phosphorus was not detected by the EDX analysis, even in samples treated with 1000 ppm P. This fact suggests that phosphorus was present either below the EDX detection limit or that elemental phosphorus was preferentially dissolved in KI, thereby limiting diffusion into the pyrite lattice. As derived from the hot probe measurements, the recrystallized
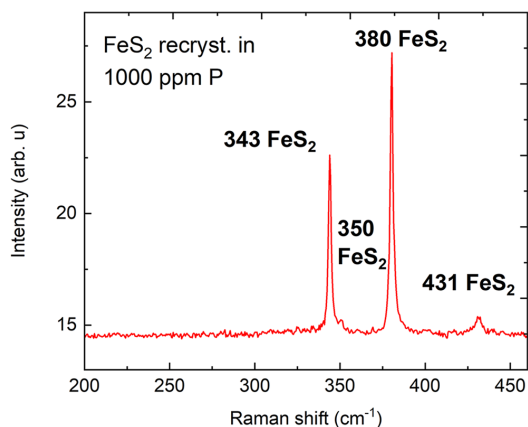

Figure 4. Raman spectrum of the FeS_2 material recrystallized in the presence of phosphorus at a 1000 ppm level.

material's conductivity remained *n*-type and was not changed after the treatment.

ICPMS analysis data of pyrite microcrystals recrystallized in KI with added phosphorus are presented in Table 1. The

Table 1. ICPMS Analysis Data of Pyrite Microcrystals Recrystallized in Ki with Added Phosphorus

intended P level in FeS_2		analyzed P content in FeS_2/ppm (molar basis)	measurement error ±
0.004 atom %	40 ppm	27[a]	0.22
0.01 atom %	100 ppm	29[a]	0.40
0.03 atom %	300 ppm	30[a]	0.08
0.06 atom %	600 ppm	32[a]	0.22
0.1 atom %	1000 ppm	39	0.72
undoped, not treated		59	2.27

[a]Below detection accuracy.

determined P levels in pyrite crystals remained below the specific detection accuracy of the ICPMS instrument. Notably, the undoped pyrite exhibited nearly twice the phosphorus concentration (59 ppm) compared to the doped samples. This suggests that phosphorus is predominantly extracted from solid crystals during recrystallization in the liquid flux, due to the distribution of P between solid and liquid phases. The purification phenomenon in the molten salt was also reported in one of our previous works.[15]

The reason for the lack of phosphorus incorporation may be the oxidation state of phosphorus in the used dopant. In Chapter 3.1, we saw that sulfur, as a strong oxidizer, oxidized
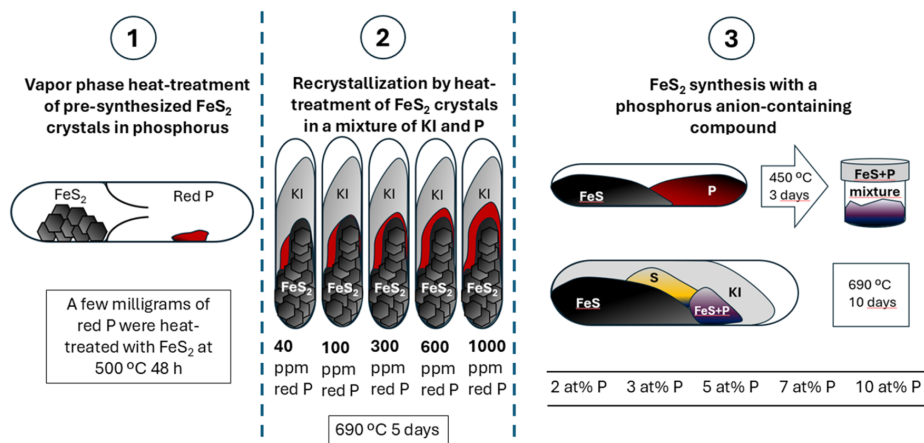
Figure 1. Schematic drawing of the three adopted doping treatments: (1) in the vapor phase, (2) during recrystallization, and (3) during synthesis of pyrite crystals.

integration using simple roll-to-roll manufacturing techniques.[16]

An additional benefit of the molten salt synthesis approach is its ability to distribute all the precursors and any impurities uniformly during crystal growth. Our previous findings[15] revealed that pyrite crystals synthesized by this method exhibited reduced copper impurity concentrations relative to the precursor materials. This purification is driven by thermodynamic equilibrium, which promotes the distribution of impurities between the molten salt and the solid crystal phase. Variations in Fermi level positions and valence band maxima observed with different flux compositions suggest a significant influence of unintentional doping originating from flux-derived impurities.[15] These observations imply that intentional dopants, such as phosphorus, can also be incorporated into pyrite crystals through the molten salt synthesis-growth process.

In the present work, we develop a novel and scalable technique for producing large volumes of p-type FeS$_2$ crystals. We explored three different strategies for incorporating phosphorus into pyrite microcrystals and investigated the underlying chemical mechanism. This study is building upon the experimental findings of Voigt et al.[13] which is the only published study concerning phosphorus-doped p-type FeS$_2$ single crystals. They report[13] using the chemical vapor transport (CVT) method for the synthesis of p-type material. A key limitation of the CVT approach is its low throughput, typically yielding only a small number of crystals per run. In contrast, by utilizing a molten salt medium containing phosphorus-based dopants, we demonstrate the potential to synthesize and dope thousands of FeS$_2$ crystals simultaneously. This liquid-phase growth technique represents a promising route for the scalable production of doped FeS$_2$ crystals and may facilitate future mass manufacturing of pyrite-based photovoltaic materials.

2. EXPERIMENTAL SECTION

2.1. Materials and Methods. Undoped and doped pyrite crystals were synthesized in sealed quartz ampules using the liquid flux growth method, which is described thoroughly in our previous publications.[14,15] Iron monosulfide (FeS, 99.9%,

Thermo Fischer Scientific) and elemental sulfur (S, 99.999%, Alfa Aesar) were used as precursors for pyrite. Red phosphorus (P, 99.5%, Reahim) was used for doping. The precursors for the synthesis of pyrite were weighed in stoichiometric ratios. Potassium iodide (KI, 99.995%, Acros Organics) was added to the precursor mixture to form a liquid flux phase at the synthesis temperature. The presence of this liquid phase facilitates the growth of individual FeS$_2$ microcrystals. To achieve optimal conditions, KI was added in an amount such that the volume of the molten KI approximately matched the volume of the solid FeS$_2$ precursors. This ensures that the liquid phase fills the voids between solid particles, promoting uniform crystal growth and enabling repulsive interactions between forming FeS$_2$ crystals, which helps prevent agglomeration. The precursors (FeS and S) and KI were mixed and inserted into quartz ampules. The ampules were degassed in a dynamic vacuum, sealed in flame, and placed into a chamber furnace. The ampules were heated to 690 °C, a little bit over the melting point of KI (681 °C)[19] and kept at 690 °C for 10 days. Pyrite crystals grow in these conditions by the Ostwald ripening mechanism.[20] The synthesis-growth lasted for 10 days, to give enough time to form FeS$_2$ microcrystals that are sufficiently large for our application. For the fabrication of monograin membranes, each microcrystal should fall in the diameter range of 40−150 μm. The crystals are then sieved into narrow granulometric fractions. Under our synthesis conditions, it typically[7,14,15] takes about 10 days to produce a batch in which a significant fraction of the FeS$_2$ crystals meet this size requirement. During the high-temperature synthesis, the pressure inside the ampules is primarily generated by sulfur that has not yet reacted with FeS. The vapor pressure of sulfur at 690 °C is high, at around 5000 Torr. After the synthesis, KI is removed from the FeS$_2$ crystals by leaching in deionized water.

Several strategies were applied to dope pyrite microcrystals with phosphorus. The only previously published study on phosphorus doping of pyrite[13] served as the basis for the first experiment. In that study, FeS$_2$ crystals were synthesized via chemical vapor transport using FeS$_2$ powder and red phosphorus. Building on this approach, we designed a two-chamber quartz ampule system, drawn in Figure 1(1). The
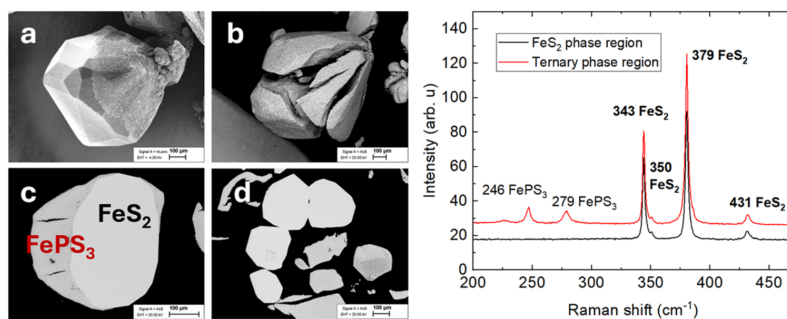
Figure 2. Left: SEM images of the FeS$_2$ microcrystals after heat treatment in P vapor atmosphere. (a, b) images of the surface, (c, d) images of the cross-section. Right: Raman spectra of the pyrite crystals' cross-section after treatment in the phosphorus vapor atmosphere.

chambers were connected by a narrow neck that allowed the transfer of phosphorus vapor. FeS$_2$ crystals presynthesized as described before were placed in one chamber, while a few milligrams of red phosphorus were placed in the other. The ampules were evacuated, sealed, and heated in a furnace at 500 °C for 48 h. The vapor pressure profiles of sulfur and phosphorus are similar, and the vapor pressure of phosphorus at 500 °C is approximately 3000 Torr, assuring effective material transport under these conditions.

Next, red phosphorus was mixed with potassium iodide and employed as a flux during the molten-phase recrystallization of presynthesized pyrite microcrystals. For the recrystallization, previously synthesized FeS$_2$ material was placed in quartz ampules. A potassium iodide and phosphorus mixture was prepared separately by adding P to KI in the amount to yield 1000 ppm P in KI. This 1000 ppm mixture was diluted with pure KI to yield the final concentrations and was added to the FeS$_2$ crystals to yield 40, 100, 300, 600, and 1000 ppm phosphorus, on a molar basis, in each ampule, respectively. This concentration is equivalent to 0.004, 0.01, 0.03, 0.06, 0.1 atom % P. The ampules were degassed, sealed, and heated at 690 °C for 5 days. This process is visualized in Figure 1(2).

The third approach to incorporating phosphorus into pyrite involved using a self-synthesized iron sulfide−phosphide (hereafter FeS + P) precursor. This precursor was prepared by mixing equimolar amounts of FeS and red phosphorus, followed by heat treatment in a sealed quartz ampule at 450 °C for 3 days. After heating, the FeS + P mixture was extracted and stored for subsequent use. For the synthesis of phosphorus-doped pyrite, this precursor was combined with FeS and sulfur in a quartz ampule. The amounts were calculated to yield stoichiometric FeS$_2$ with phosphorus concentrations of 2, 3, 5, 7, and 10 atomic percent (atom %) relative to sulfur in the final crystals. Potassium iodide flux was added as described previously for the undoped samples. The visual representation is shown in Figure 1(3). The degassed and sealed ampules were then heated at 690 °C for 10 days to complete the synthesis.

A mixture of iron and phosphorus (hereafter Fe + P) was synthesized in the same way as described above and used as an alternative to the FeS + P mixture to synthesize and dope FeS$_2$ crystals in a parallel experiment. Figure 1 represents a schematic depiction of the three doping strategies explored in this study.

2.2. Analytical Techniques. Materials were analyzed by different methods to evaluate the success of each phosphorus treatment and to understand the possible chemical route of phosphorus incorporation into pyrite microcrystals. The phase composition was analyzed by Raman spectroscopy, using a Horiba LabRam HR800 spectrometer equipped with a multichannel CCD detection system in the backscattering configuration. 532 nm laser line with a spot size of 5 μm was applied for excitation. X-ray diffraction (XRD) patterns were recorded on a Rigaku Ultima IV diffractometer with Cu Kα radiation (λ = 1.5406 Å). PDXL 2 software was used to derive crystal structure information from the recorded XRD data.

The conductivity type of crystals was determined by the hot probe method. For this technique, a sample crystal is placed between two contacts. One contact or probe is heated, thermally exciting the charge carriers in the vicinity of the hot probe. Carriers move by diffusion from the hot probe to the "cold" probe, which stays at room temperature. The type of majority carriers defines the electrical potential sign in the multimeter.[21]

The chemical composition of crystals was assessed by energy dispersive X-ray spectroscopy (EDX) using a Bruker Esprit 1.8 system. The EDX measurements were taken from the cross-section (bulk) of materials, from at least 8 individual crystals of each sample. The measurement limit of the EDX system is 0.1 atom %.

Inductively coupled plasma mass spectroscopy (ICPMS) was used to determine the level of impurities in crystals. 0.1 g of solid samples were dissolved in a mixture of 8 mL of HNO$_3$ and 2 mL of H$_2$O$_2$ using an Anton Paar Multiwave PRO microwave digestion system. Samples were digested at 230 °C at pressures between 45−50 bar. The sample solutions were diluted with 2% HNO$_3$. Concentrations of impurity elements were measured using Agilent 8800 ICPMS/MS. Indium was used as an internal standard element added online via mixing T and NIST 1643f, which were used as references for quality control.

The morphology of different crystals was evaluated using high-resolution scanning electron microscopy (SEM) Zeiss ULTRA 55.

3. RESULTS AND DISCUSSION

3.1. Vapor Phase Heat-Treatment of Pre-Synthesized FeS$_2$ Crystals in Phosphorus. Phosphorus incorporation in pyrite crystals was first carried out via vapor-phase treatment. Post-treatment analysis revealed that P reacted with FeS$_2$, resulting in the formation of two distinct phases. Part of the material remained in the FeS$_2$ phase; however, a significant

octahedrally by six P atoms.[33] Phosphorus atoms are arranged as tetrahedra with either two P atoms and two Fe atoms, or three P atoms and one Fe atom. In this configuration, phosphorus is found in the 3- and 2- anionic states.[33]

The FeP and Fe_2P phases in the Fe + P precursor also host P in 3- and 2- charge, but the phosphorus and iron are bound with double and triple bonds with dissociation energies up to 2 or 3 times the Fe−P single bond.[34,35] The synthesis conditions (temperature and pressure) for FeS_2 synthesis in the liquid phase do not allow for the breaking of higher energy Fe−P multinary bonds, making the FeP_4 phase the only available compound for phosphorus doping during the synthesis of pyrite microcrystals. The Fe−P−S phases that are not participating in the doping or synthesis of pyrite dissolve in the liquid salt flux and are removed after the synthesis process.

The proposed doping mechanism is based on the theory of Kröger.[27] Doping takes place in pyrite when phosphorus atoms substitute for sulfur ions within the pyrite lattice. Since sulfur carries a 2- charge and phosphorus in our setup a 3- charge, phosphorus accepts more electrons than sulfur. This substitution leads to the formation of iron vacancies, which act as p-type acceptor defects in pyrite. When FeP_4 is used as a doping compound, four P atoms will substitute for four S atoms, at the same time introducing only one Fe atom. This mechanism generates three Fe vacancies in the pyrite lattice. Phosphorus does not occupy sulfur vacancy sites—the generation and elimination of sulfur vacancy defects are governed by thermal treatments and sulfur vapor pressure.[27,36] Our findings indicate that even under saturated sulfur pressure at 690 °C, sulfur vacancies are not fully suppressed, nor are iron vacancies effectively induced. A comprehensive understanding of synthesis conditions and doping strategies is essential for advancing the use of p-type pyrite crystals as the absorber of photovoltaic devices and for enabling the development of pyrite-based solar cells.

4. CONCLUSIONS

This study investigated three approaches to achieve p-type doping of FeS_2 (pyrite) crystals. The first involved postsynthesis heat treatment of FeS_2 crystals in a phosphorus vapor atmosphere. The second approach utilized high-temperature recrystallization of FeS_2 in a mixture of molten KI and elemental P. Both methods, however, resulted in n-type FeS_2. The third strategy, synthesizing pyrite crystals in a liquid salt medium using a phosphorus-containing precursor, proved successful, yielding p-type FeS_2. This method represents the first scalable approach for phosphorus doping of FeS_2 crystals. The phosphorus precursor was prepared by reacting FeS with elemental P in an evacuated quartz ampule at 450 °C. XRD analysis confirmed that the resulting precursor mixture contained FeP_4, which was identified as the only effective phosphorus compound enabling incorporation into the FeS_2 lattice during synthesis. The resulting doped material was characterized by Raman spectroscopy and XRD, both confirming the formation of the pyrite phase. Although the phosphorus concentration was below the EDX detection limit of ~0.1 atom %, hot-probe measurements indicated a clear conductivity type inversion from n-type to p-type.

A mechanism for phosphorus incorporation into the pyrite lattice is proposed based on theoretical considerations: FeP_4 facilitates the substitution of sulfur sites by phosphorus atoms in the pyrite lattice. For every four phosphorus atoms incorporated, one iron site is occupied, leading to the formation of three iron vacancies, which act as acceptors and enable hole conduction. These findings provide a foundation for future development of photovoltaic devices based on p-type FeS_2, including potential applications in homojunction solar cells.

■ ASSOCIATED CONTENT

ⓢ Supporting Information

The Supporting Information is available free of charge at https://pubs.acs.org/doi/10.1021/acsomega.5c07455.

EDX spectra and mapping results of FeS_2 materials discussed in this study, a discussion on the uniformity of the material across larger batches, the reaction pathway for the creation of the layered $FePS_3$ phase, and a comparison table of the used doping techniques (PDF)

■ AUTHOR INFORMATION

Corresponding Author

Katriin Reedo − Department of Materials and Environmental Technology, Tallinn University of Technology, 19086 Tallinn, Estonia; ⓞ orcid.org/0000-0002-6002-2135; Email: katriin.reedo@taltech.ee

Authors

Taavi Raadik − Department of Materials and Environmental Technology, Tallinn University of Technology, 19086 Tallinn, Estonia

Mare Altosaar − Department of Materials and Environmental Technology, Tallinn University of Technology, 19086 Tallinn, Estonia

Maris Pilvet − Department of Materials and Environmental Technology, Tallinn University of Technology, 19086 Tallinn, Estonia

Annaly Gutjuma − Department of Materials and Environmental Technology, Tallinn University of Technology, 19086 Tallinn, Estonia

Jüri Krustok − Department of Materials and Environmental Technology, Tallinn University of Technology, 19086 Tallinn, Estonia

Peeter Paaver − Institute of Ecology and Earth Sciences, Tartu University, 50090 Tartu, Estonia

Complete contact information is available at:
https://pubs.acs.org/10.1021/acsomega.5c07455

Author Contributions

K.R.: Conceptualization, investigation, formal analysis, data curation, visualization, writing−original draft, writing−review and editing. T.R.: Funding acquisition, investigation, project administration, supervision, writing−review and editing. M.A.: Methodology, supervision, validation, Writing−review and editing. M.P.: Investigation, data curation. A.G.: Investigation, data curation. J.K.: Validation, writing−review and editing. P.P.: Investigation.

Notes

The authors declare no competing financial interest.

■ ACKNOWLEDGMENTS

■ REFERENCES

(1) Ray, D.; Voigt, B.; Manno, M.; Leighton, C.; Aydil, E. S.; Gagliardi, L. Sulfur Vacancy Clustering and Its Impact on Electronic Properties in Pyrite FeS 2. *Chem. Mater.* **2020**, *32* (11), 4820−4831.

(2) Voigt, B.; Moore, W.; Manno, M.; Walter, J.; Jeremiason, J. D.; Aydil, E. S.; Leighton, C. Transport Evidence for Sulfur Vacancies as the Origin of Unintentional N-Type Doping in Pyrite FeS 2. *ACS Appl. Mater. Interfaces* **2019**, *11* (17), 15552−15563.

(3) Zaka, A.; Alhassan, S. M.; Nayfeh, A. Iron Pyrite in Photovoltaics: A Review on Recent Trends and Challenges. *ACS Appl. Electron Mater.* **2022**, *4* (9), 4173−4211.

(4) Rahman, M.; Boschloo, G.; Hagfeldt, A.; Edvinsson, T. On the Mechanistic Understanding of Photovoltage Loss in Iron Pyrite Solar Cells. *Adv. Mater.* **2020**, *32* (26), No. 1905653, DOI: 10.1002/adma.201905653.

(5) Zaka, A.; Alhassan, S.; Nayfeh, A. Understanding the Phase Changes and Optical Properties in the Solvothermal Synthesis of Iron Pyrite. *Sci. Rep.* **2025**, *15* (1), No. 18763.

(6) Wadia, C.; Alivisatos, A. P.; Kammen, D. M. Materials Availability Expands the Opportunity for Large-Scale Photovoltaics Deployment. *Environ. Sci. Technol.* **2009**, *43* (6), 2072−2077.

(7) Kristmann, K.; Raadik, T.; Altosaar, M.; Grossberg-Kuusk, M.; Krustok, J.; Pilvet, M.; Mikli, V.; Kauk-Kuusik, M.; Makaya, A. Pyrite as Promising Monograin Layer Solar Cell Absorber Material for In-Situ Solar Cell Fabrication on the Moon. *Acta Astronaut.* **2022**, *199*, 420−424.

(8) Ennaoui, A.; Fiechter, S.; Pettenkofer, Ch.; Alonso-Vante, N.; Büker, K.; Bronold, M.; Höpfner, Ch.; Tributsch, H. Iron Disulfide for Solar Energy Conversion. *Sol. Energy Mater. Sol. Cells* **1993**, *29* (4), 289−370.

(9) Luo, L.; Luan, W.; Yuan, B.; Zhang, C.; Jin, L. High Efficient and Stable Solid Solar Cell: Based on FeS2 Nanocrystals and P3HT: PCBM. *Energy Procedia* **2015**, *75*, 2181−2186.

(10) Limpinsel, M.; Farhi, N.; Berry, N.; Lindemuth, J.; Perkins, C. L.; Lin, Q.; Law, M. An Inversion Layer at the Surface of N-Type Iron Pyrite. *Energy Environ. Sci.* **2014**, *7* (6), 1974−1989.

(11) Gohri, S.; Madan, J.; Mohammed, M. K. A.; Pandey, R. Inherent Internal P-n Junction Assisted Single Layered n-Type Iron Pyrite Solar Cell. *Mater. Res. Express* **2023**, *10* (2), No. 024001.

(12) Voigt, B.; Moore, W.; Maiti, M.; Walter, J.; Das, B.; Manno, M.; Leighton, C.; Aydil, E. S. Observation of an Internal p−n Junction in Pyrite FeS2 Single Crystals: Potential Origin of the Low Open Circuit Voltage in Pyrite Solar Cells. *ACS Mater. Lett.* **2020**, *2* (7), 861−868.

(13) Voigt, B.; Valor, L. S.; Moore, W.; Jeremiason, J.; Kakalios, J.; Aydil, E. S.; Leighton, C. Controlled P-Type Doping of Pyrite FeS2. *ACS Appl. Mater. Interfaces* **2023**, *15* (23), 28258−28266.

(14) Kristmann, K.; Altosaar, M.; Raudoja, J.; Krustok, J.; Pilvet, M.; Mikli, V.; Grossberg, M.; Danilson, M.; Raadik, T. Pyrite as Prospective Absorber Material for Monograin Layer Solar Cell. *Thin Solid Films* **2022**, *743*, No. 139068.

(15) Kristmann, K.; Raadik, T.; Altosaar, M.; Danilson, M.; Krustok, J.; Paaver, P.; Butenko, Y. Characterization of FeS2 Pyrite Microcrystals Synthesized in Different Flux Media. *Mater. Adv.* **2024**, *5* (4), 1565−1575.

(16) Meissner, D.; Ernits, K.; Gahr, S.; Kapitan, L.; Vetter, M.; Glatz, C.; Syed, R. Kesterite Based Monograin Photovoltaics: The Ideal Solution for Sustainable Power Supply. *Sol. Energy Mater. Sol. Cells* **2023**, *252*, No. 112160.

(17) Mellikov, E.; Meissner, D.; Varema, T.; Altosaar, M.; Kauk, M.; Volobujeva, O.; Raudoja, J.; Timmo, K.; Danilson, M. Monograin Materials for Solar Cells. *Sol. Energy Mater. Sol. Cells* **2009**, *93* (1), No. 65.

(18) Ghisani, F.; Timmo, K.; Altosaar, M.; Mikli, V.; Pilvet, M.; Kaupmees, R.; Krustok, J.; Grossberg, M.; Kauk-Kuusik, M. Characterization of Tetrahedrite Cu10Cd2Sb4S13 Monograin

(19) ScholAR Chemistry. *Material Safety Data Sheet Potassium Iodide* Henrietta Rd, Rochester, NY; 2008.

(20) Voorhees, P. W. Ostwald Ripening of Two-Phase Mixtures 1992 www.annualreviews.org.

(21) Axelevitch, A.; Golan, G. Hot-Probe Method for Evaluation of Majority Charged Carriers Concentration in Semiconductor Thin Films. *Facta Univ. - Ser.: Electron. Energ.* **2013**, *26* (3), 187−195.

(22) Utyuzh, A. N. Influence of Temperature on Raman Spectra of the FeS2 Single Crystal with Pyrite Structure. *Phys. Solid State* **2014**, *56* (10), 2050−2055.

(23) Yuan, X.; Zheng, H. In Situ Raman Spectroscopic Studies of FeS2 Pyrite up to 675 K and 2100 MPa Using a Hydrothermal Diamond Anvil Cell. *Mineral. Mag.* **2015**, *79* (1), 1−10.

(24) Mayorga-Martinez, C. C.; Sofer, Z.; Sedmidubský, D.; Huber, Š.; Eng, A. Y. S.; Pumera, M. Layered Metal Thiophosphite Materials: Magnetic, Electrochemical, and Electronic Properties. *ACS Appl. Mater. Interfaces* **2017**, *9* (14), 12563−12573.

(25) Kleppe, A. K.; Jephcoat, A. P. High-Pressure Raman Spectroscopic Studies of FeS2 Pyrite. *Mineral. Mag.* **2004**, *68* (3), 433−441.

(26) Mutlu, Z.; Debnath, B.; Su, S.; Li, C.; Ozkan, M.; Bozhilov, K. N.; Lake, R. K.; Ozkan, C. S. Chemical Vapor Deposition and Phase Stability of Pyrite on SiO2. *J. Mater. Chem. C* **2018**, *6* (17), 4753−4759.

(27) Kröger, F. A.Detailed Description of Crystalline Solids. In *Chemistry of Imperfect Crystals*; North-Holland Publishing Company, 1964; pp 194−211.

(28) Gonçalves, G. R.; Schettino, M. A.; Schettino, C. S.; Piccoli, V.; de Jesus, H. C.; Vieira, M. A.; Cunha, A. G.; Freitas, J. C. C. Synthesis of Iron Phosphide Nanoparticles Dispersed in Activated Carbon and Their Application in Fenton Processes. *J. Nanopart. Res.* **2022**, *24* (10), No. 193.

(29) Wang, H.; Su, R.; Liu, Y.; Kong, Y.; Ren, Z.; Jiang, B. Iron-group Metal Compound Electrocatalysts for Efficient Hydrogen Production: Recent Advances and Future Prospects. *ChemCatChem* **2024**, *16* (8), No. e202301241, DOI: 10.1002/cctc.202301241.

(30) Tang, X.; Chen, Y. A Review of Flotation and Selective Separation of Pyrrhotite: A Perspective from Crystal Structures. *Int. J. Min. Sci. Technol.* **2022**, *32* (4), 847−863.

(31) Rödl, T.; Pfitzner, A. The Crystal and Molecular Structure of ΓP4S6. *Z. Anorg. Allg. Chem.* **2011**, *637* (11), 1507−1510.

(32) Zunger, A. Practical Doping Principles. In *National Center for Photovoltaics and Solar Program Review Meeting*; National Renewable Energy Laboratory: Denver, 2003.

(33) Sugitani, M.; Kinomura, N.; Koizumi, M.; Kume, S. Preparation and Properties of a New Iron Phosphide FeP4. *J. Solid State Chem.* **1978**, *26*, 195−201.

(34) PubChem, N. L. of M.. Diiron monophosphide (Fe2P). https://pubchem.ncbi.nlm.nih.gov/compound/1310-43-6. (accessed June 30, 2025, 2025).

(35) PubChem, N. L. of M.. Iron phosphide (FeP). https://pubchem.ncbi.nlm.nih.gov/compound/Iron-phosphide-_FeP. (accessed 30 June 30, 2025).

(36) Srivastava, R. P.; Saxena, A. P.; Ingole, S. N-Type Iron Pyrite (FeS2) Thin-Films Obtained at Different Sulfur Vapor Pressures. *Chalcogenide Lett.* **2017**, *14* (6), 227−237.

Materials Grown in Molten CdI2 and LiI. *Thin Solid Films* **2021**, *739*, No. 138980.

■ NOTE ADDED AFTER ASAP PUBLICATION

Due to a production error, the version of this paper that was published ASAP November 26, 2025, was missing an entry at the bottom of Table 1. The corrected version was posted November 26, 2025.
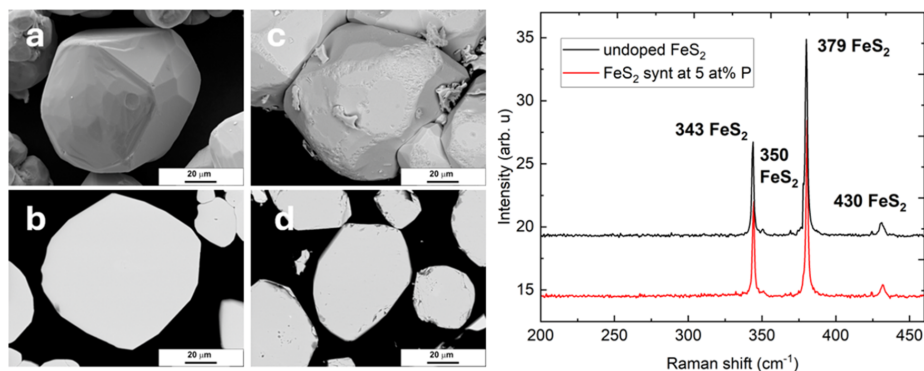
Figure 5. Left: SEM images of the FeS_2 materials synthesized and doped using a previously prepared FeS + P mixture. FeS_2 crystals were synthesized with (a, b) 5 atom % P; and (c, d) 10 atom % P. Right: Raman spectra of the *n*- and *p*-type FeS_2 materials. Black line: *n*-type and undoped FeS_2. Red line: *p*-type FeS_2, synthesized with 5 atom % P, using the FeS + P precursor.
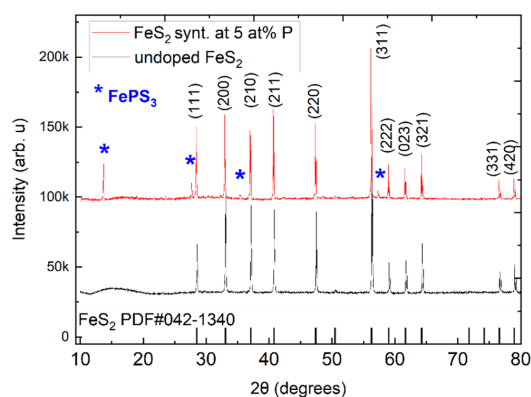

Figure 6. XRD results of the doped and undoped pyrite microcrystals, synthesized and doped by the flux growth method. Black pattern: undoped pyrite crystals. Red pattern: pyrite crystals synthesized with 5 atom % P using the FeS + P precursor.

Figure 7. XRD results of the two different phosphorus precursors. Black pattern: precursor mixture prepared from FeS and P. Purple pattern: the precursor mixture prepared by heating elemental Fe and P.

its conductivity is critical for improving the reproducibility of this doping method.

The observation that the use of Fe + P precursor does not lead to *p*-type doping, whereas the FeS + P precursor yields *p*-type pyrite, suggests that a specific compound that allows phosphorus incorporation in pyrite is present in the latter. This compound, absent in the Fe + P system, likely facilitates phosphorus incorporation into pyrite in a chemically compatible form and promotes hole generation, thereby inducing a transition from *n*-type to *p*-type conductivity. XRD analysis was performed on both types of precursor mixtures to identify the relevant phases present in each precursor system. The phase compositions are shown in Figure 7 and in Table 3. The FeS + P precursor was found to contain P_4S_6, pyrrhotite $(Fe_{0.893}S)$,[30] and FeP_4. In contrast, the Fe + P precursor contained elemental phosphorus, FeP, and Fe_2P. Among these, P_4S_6 and FeP_4 are the possible candidates for P incorporation in FeS_2. P_4S_6 contains phosphorus in the 3+ oxidation state,[31] chemically unsuitable for occupying S^{2-} sites.[32] However, the P_4S_6 phase might be responsible for the creation of the $FePS_3$ minority phase that was recognized by

Table 3. Summary of the Phosphorus Precursors Phase Composition, Based on the XRD Results

used precursor	compounds present, determined by XRD	quantity in the mixture (%)	charge of the phosphorus ion
Fe + P mixture, heated at 450 °C	elemental phosphorus	9	0
	FeP	72	2-; 3-[a]
	Fe_2P	19	3-[a]
FeS + P mixture, heated at 450 °C	P_4S_6	2	3+
	pyrrhotite $(Fe_{0.893}S)$	8	n/a
	FeP_4	90	2-; 3-

[a]In this case, the phosphorus is bound to iron by double and triple bonds, which have higher energy and are not broken under our synthesis conditions.

the XRD measurements of the *p*-type pyrite material, shown in Figure 6. The possible reaction pathway is brought in Supporting Information 4.

The FeS + P precursor also contained FeP_4, which is a distinct iron phosphide phase with the Fe atom surrounded

octahedrally by six P atoms.[33] Phosphorus atoms are arranged as tetrahedra with either two P atoms and two Fe atoms, or three P atoms and one Fe atom. In this configuration, phosphorus is found in the 3- and 2- anionic states.[33]

The FeP and Fe_2P phases in the Fe + P precursor also host P in 3- and 2- charge, but the phosphorus and iron are bound with double and triple bonds with dissociation energies up to 2 or 3 times the Fe−P single bond.[34,35] The synthesis conditions (temperature and pressure) for FeS_2 synthesis in the liquid phase do not allow for the breaking of higher energy Fe−P multinary bonds, making the FeP_4 phase the only available compound for phosphorus doping during the synthesis of pyrite microcrystals. The Fe−P−S phases that are not participating in the doping or synthesis of pyrite dissolve in the liquid salt flux and are removed after the synthesis process.

The proposed doping mechanism is based on the theory of Kröger.[27] Doping takes place in pyrite when phosphorus atoms substitute for sulfur ions within the pyrite lattice. Since sulfur carries a 2- charge and phosphorus in our setup a 3- charge, phosphorus accepts more electrons than sulfur. This substitution leads to the formation of iron vacancies, which act as p-type acceptor defects in pyrite. When FeP_4 is used as a doping compound, four P atoms will substitute for four S atoms, at the same time introducing only one Fe atom. This mechanism generates three Fe vacancies in the pyrite lattice. Phosphorus does not occupy sulfur vacancy sites—the generation and elimination of sulfur vacancy defects are governed by thermal treatments and sulfur vapor pressure.[27,36] Our findings indicate that even under saturated sulfur pressure at 690 °C, sulfur vacancies are not fully suppressed, nor are iron vacancies effectively induced. A comprehensive understanding of synthesis conditions and doping strategies is essential for advancing the use of p-type pyrite crystals as the absorber of photovoltaic devices and for enabling the development of pyrite-based solar cells.

4. CONCLUSIONS

This study investigated three approaches to achieve p-type doping of FeS_2 (pyrite) crystals. The first involved postsynthesis heat treatment of FeS_2 crystals in a phosphorus vapor atmosphere. The second approach utilized high-temperature recrystallization of FeS_2 in a mixture of molten KI and elemental P. Both methods, however, resulted in n-type FeS_2. The third strategy, synthesizing pyrite crystals in a liquid salt medium using a phosphorus-containing precursor, proved successful, yielding p-type FeS_2. This method represents the first scalable approach for phosphorus doping of FeS_2 crystals. The phosphorus precursor was prepared by reacting FeS with elemental P in an evacuated quartz ampule at 450 °C. XRD analysis confirmed that the resulting precursor mixture contained FeP_4, which was identified as the only effective phosphorus compound enabling incorporation into the FeS_2 lattice during synthesis. The resulting doped material was characterized by Raman spectroscopy and XRD, both confirming the formation of the pyrite phase. Although the phosphorus concentration was below the EDX detection limit of ∼0.1 atom %, hot-probe measurements indicated a clear conductivity type inversion from n-type to p-type.

A mechanism for phosphorus incorporation into the pyrite lattice is proposed based on theoretical considerations: FeP_4 facilitates the substitution of sulfur sites by phosphorus atoms in the pyrite lattice. For every four phosphorus atoms incorporated, one iron site is occupied, leading to the formation of three iron vacancies, which act as acceptors and enable hole conduction. These findings provide a foundation for future development of photovoltaic devices based on p-type FeS_2, including potential applications in homojunction solar cells.

■ ASSOCIATED CONTENT

Ⓢ Supporting Information

The Supporting Information is available free of charge at https://pubs.acs.org/doi/10.1021/acsomega.5c07455.

EDX spectra and mapping results of FeS_2 materials discussed in this study, a discussion on the uniformity of the material across larger batches, the reaction pathway for the creation of the layered $FePS_3$ phase, and a comparison table of the used doping techniques (PDF)

■ AUTHOR INFORMATION

Corresponding Author

Katriin Reedo − *Department of Materials and Environmental Technology, Tallinn University of Technology, 19086 Tallinn, Estonia;* ⓞ orcid.org/0000-0002-6002-2135; Email: katriin.reedo@taltech.ee

Authors

Taavi Raadik − *Department of Materials and Environmental Technology, Tallinn University of Technology, 19086 Tallinn, Estonia*

Mare Altosaar − *Department of Materials and Environmental Technology, Tallinn University of Technology, 19086 Tallinn, Estonia*

Maris Pilvet − *Department of Materials and Environmental Technology, Tallinn University of Technology, 19086 Tallinn, Estonia*

Annaly Gutjuma − *Department of Materials and Environmental Technology, Tallinn University of Technology, 19086 Tallinn, Estonia*

Jüri Krustok − *Department of Materials and Environmental Technology, Tallinn University of Technology, 19086 Tallinn, Estonia*

Peeter Paaver − *Institute of Ecology and Earth Sciences, Tartu University, 50090 Tartu, Estonia*

Complete contact information is available at:
https://pubs.acs.org/10.1021/acsomega.5c07455

Author Contributions

K.R.: Conceptualization, investigation, formal analysis, data curation, visualization, writing—original draft, writing—review and editing. T.R.: Funding acquisition, investigation, project administration, supervision, writing—review and editing. M.A.: Methodology, supervision, validation, Writing—review and editing. M.P.: Investigation, data curation. A.G.: Investigation, data curation. J.K.: Validation, writing—review and editing. P.P.: Investigation.

Notes

The authors declare no competing financial interest.

■ ACKNOWLEDGMENTS

REFERENCES

(1) Ray, D.; Voigt, B.; Manno, M.; Leighton, C.; Aydil, E. S.; Gagliardi, L. Sulfur Vacancy Clustering and Its Impact on Electronic Properties in Pyrite FeS 2. *Chem. Mater.* **2020**, 32 (11), 4820−4831.

(2) Voigt, B.; Moore, W.; Manno, M.; Walter, J.; Jeremiason, J. D.; Aydil, E. S.; Leighton, C. Transport Evidence for Sulfur Vacancies as the Origin of Unintentional N-Type Doping in Pyrite FeS 2. *ACS Appl. Mater. Interfaces* **2019**, 11 (17), 15552−15563.

(3) Zaka, A.; Alhassan, S. M.; Nayfeh, A. Iron Pyrite in Photovoltaics: A Review on Recent Trends and Challenges. *ACS Appl. Electron Mater.* **2022**, 4 (9), 4173−4211.

(4) Rahman, M.; Boschloo, G.; Hagfeldt, A.; Edvinsson, T. On the Mechanistic Understanding of Photovoltage Loss in Iron Pyrite Solar Cells. *Adv. Mater.* **2020**, 32 (26), No. 1905653, DOI: 10.1002/adma.201905653.

(5) Zaka, A.; Alhassan, S.; Nayfeh, A. Understanding the Phase Changes and Optical Properties in the Solvothermal Synthesis of Iron Pyrite. *Sci. Rep.* **2025**, 15 (1), No. 18763.

(6) Wadia, C.; Alivisatos, A. P.; Kammen, D. M. Materials Availability Expands the Opportunity for Large-Scale Photovoltaics Deployment. *Environ. Sci. Technol.* **2009**, 43 (6), 2072−2077.

(7) Kristmann, K.; Raadik, T.; Altosaar, M.; Grossberg-Kuusk, M.; Krustok, J.; Pilvet, M.; Mikli, V.; Kauk-Kuusik, M.; Makaya, A. Pyrite as Promising Monograin Layer Solar Cell Absorber Material for In-Situ Solar Cell Fabrication on the Moon. *Acta Astronaut.* **2022**, 199, 420−424.

(8) Ennaoui, A.; Fiechter, S.; Pettenkofer, Ch.; Alonso-Vante, N.; Büker, K.; Bronold, M.; Höpfner, Ch.; Tributsch, H. Iron Disulfide for Solar Energy Conversion. *Sol. Energy Mater. Sol. Cells* **1993**, 29 (4), 289−370.

(9) Luo, L.; Luan, W.; Yuan, B.; Zhang, C.; Jin, L. High Efficient and Stable Solid Solar Cell: Based on FeS2 Nanocrystals and P3HT: PCBM. *Energy Procedia* **2015**, 75, 2181−2186.

(10) Limpinsel, M.; Farhi, N.; Berry, N.; Lindemuth, J.; Perkins, C. L.; Lin, Q.; Law, M. An Inversion Layer at the Surface of N-Type Iron Pyrite. *Energy Environ. Sci.* **2014**, 7 (6), 1974−1989.

(11) Gohri, S.; Madan, J.; Mohammed, M. K. A.; Pandey, R. Inherent Internal P-n Junction Assisted Single Layered n-Type Iron Pyrite Solar Cell. *Mater. Res. Express* **2023**, 10 (2), No. 024001.

(12) Voigt, B.; Moore, W.; Maiti, M.; Walter, J.; Das, B.; Manno, M.; Leighton, C.; Aydil, E. S. Observation of an Internal p−n Junction in Pyrite FeS2 Single Crystals: Potential Origin of the Low Open Circuit Voltage in Pyrite Solar Cells. *ACS Mater. Lett.* **2020**, 2 (7), 861−868.

(13) Voigt, B.; Valor, L. S.; Moore, W.; Jeremiason, J.; Kakalios, J.; Aydil, E. S.; Leighton, C. Controlled P-Type Doping of Pyrite FeS2. *ACS Appl. Mater. Interfaces* **2023**, 15 (23), 28258−28266.

(14) Kristmann, K.; Altosaar, M.; Raudoja, J.; Krustok, J.; Pilvet, M.; Mikli, V.; Grossberg, M.; Danilson, M.; Raadik, T. Pyrite as Prospective Absorber Material for Monograin Layer Solar Cell. *Thin Solid Films* **2022**, 743, No. 139068.

(15) Kristmann, K.; Raadik, T.; Altosaar, M.; Danilson, M.; Krustok, J.; Paaver, P.; Butenko, Y. Characterization of FeS2 Pyrite Microcrystals Synthesized in Different Flux Media. *Mater. Adv.* **2024**, 5 (4), 1565−1575.

(16) Meissner, D.; Ernits, K.; Gahr, S.; Kapitan, L.; Vetter, M.; Glatz, C.; Syed, R. Kesterite Based Monograin Photovoltaics: The Ideal Solution for Sustainable Power Supply. *Sol. Energy Mater. Sol. Cells* **2023**, 252, No. 112160.

(17) Mellikov, E.; Meissner, D.; Varema, T.; Altosaar, M.; Kauk, M.; Volobujeva, O.; Raudoja, J.; Timmo, K.; Danilson, M. Monograin Materials for Solar Cells. *Sol. Energy Mater. Sol. Cells* **2009**, 93 (1), No. 65.

(18) Ghisani, F.; Timmo, K.; Altosaar, M.; Mikli, V.; Pilvet, M.; Kaupmees, R.; Krustok, J.; Grossberg, M.; Kauk-Kuusik, M. Characterization of Tetrahedrite Cu10Cd2Sb4S13 Monograin

(19) ScholAR Chemistry. *Material Safety Data Sheet Potassium Iodide* Henrietta Rd, Rochester, NY; 2008.

(20) Voorhees, P. W. Ostwald Ripening of Two-Phase Mixtures 1992 www.annualreviews.org.

(21) Axelevitch, A.; Golan, G. Hot-Probe Method for Evaluation of Majority Charged Carriers Concentration in Semiconductor Thin Films. *Facta Univ. - Ser.: Electron. Energ.* **2013**, 26 (3), 187−195.

(22) Utyuzh, A. N. Influence of Temperature on Raman Spectra of the FeS2 Single Crystal with Pyrite Structure. *Phys. Solid State* **2014**, 56 (10), 2050−2055.

(23) Yuan, X.; Zheng, H. In Situ Raman Spectroscopic Studies of FeS2 Pyrite up to 675 K and 2100 MPa Using a Hydrothermal Diamond Anvil Cell. *Mineral. Mag.* **2015**, 79 (1), 1−10.

(24) Mayorga-Martinez, C. C.; Sofer, Z.; Sedmidubský, D.; Huber, Š.; Eng, A. Y. S.; Pumera, M. Layered Metal Thiophosphite Materials: Magnetic, Electrochemical, and Electronic Properties. *ACS Appl. Mater. Interfaces* **2017**, 9 (14), 12563−12573.

(25) Kleppe, A. K.; Jephcoat, A. P. High-Pressure Raman Spectroscopic Studies of FeS2 Pyrite. *Mineral. Mag.* **2004**, 68 (3), 433−441.

(26) Mutlu, Z.; Debnath, B.; Su, S.; Li, C.; Ozkan, M.; Bozhilov, K. N.; Lake, R. K.; Ozkan, C. S. Chemical Vapor Deposition and Phase Stability of Pyrite on SiO2. *J. Mater. Chem. C* **2018**, 6 (17), 4753−4759.

(27) Kröger, F. A.Detailed Description of Crystalline Solids. In *Chemistry of Imperfect Crystals*; North-Holland Publishing Company, 1964; pp 194−211.

(28) Gonçalves, G. R.; Schettino, M. A.; Schettino, C. S.; Piccoli, V.; de Jesus, H. C.; Vieira, M. A.; Cunha, A. G.; Freitas, J. C. C. Synthesis of Iron Phosphide Nanoparticles Dispersed in Activated Carbon and Their Application in Fenton Processes. *J. Nanopart. Res.* **2022**, 24 (10), No. 193.

(29) Wang, H.; Su, R.; Liu, Y.; Kong, Y.; Ren, Z.; Jiang, B. Iron-group Metal Compound Electrocatalysts for Efficient Hydrogen Production: Recent Advances and Future Prospects. *ChemCatChem* **2024**, 16 (8), No. e202301241, DOI: 10.1002/cctc.202301241.

(30) Tang, X.; Chen, Y. A Review of Flotation and Selective Separation of Pyrrhotite: A Perspective from Crystal Structures. *Int. J. Min. Sci. Technol.* **2022**, 32 (4), 847−863.

(31) Rödl, T.; Pfitzner, A. The Crystal and Molecular Structure of ΓP4S6. *Z. Anorg. Allg. Chem.* **2011**, 637 (11), 1507−1510.

(32) Zunger, A. Practical Doping Principles. In *National Center for Photovoltaics and Solar Program Review Meeting*; National Renewable Energy Laboratory: Denver, 2003.

(33) Sugitani, M.; Kinomura, N.; Koizumi, M.; Kume, S. Preparation and Properties of a New Iron Phosphide FeP4. *J. Solid State Chem.* **1978**, 26, 195−201.

(34) PubChem, N. L. of M.. Diiron monophosphide (Fe2P). https://pubchem.ncbi.nlm.nih.gov/compound/1310-43-6. (accessed June 30, 2025, 2025).

(35) PubChem, N. L. of M.. Iron phosphide (FeP). https://pubchem.ncbi.nlm.nih.gov/compound/Iron-phosphide-_FeP. (accessed 30 June 30, 2025).

(36) Srivastava, R. P.; Saxena, A. P.; Ingole, S. N-Type Iron Pyrite (FeS2) Thin-Films Obtained at Different Sulfur Vapor Pressures. *Chalcogenide Lett.* **2017**, 14 (6), 227−237.

NOTE ADDED AFTER ASAP PUBLICATION

Due to a production error, the version of this paper that was published ASAP November 26, 2025, was missing an entry at the bottom of Table 1. The corrected version was posted November 26, 2025.

Materials Grown in Molten CdI2 and LiI. *Thin Solid Films* **2021**, 739, No. 138980.

Curriculum Vitae

1. Personal data

Name	Katriin Reedo
Date and place of birth	26 August 1995 Jõhvi, Estonia
Nationality	Estonian

2. Contact information

Address	Tallinn University of Technology, School of Engineering, Department of Materials and Environmental Technology, Ehitajate tee 5, 19086 Tallinn, Estonia
E-mail	katriin.reedo@taltech.ee

3. Education

2021–2026	Tallinn University of Technology Chemical, Materials and Energy Technology, PhD studies
2019–2021	Tallinn University of Technology Materials and Processes for Sustainable Energetics, MSc *cum laude*
2014–2018	Tallinn University of Technology, Industrial Ecology, BSc
2017	Polytechnic Institute of Viana do Castelo, Portugal Exchange student

4. Language competence

Estonian	native
English	fluent
German	beginner

5. Professional employment

2021-2026	Tallinn University of Technology, early stage researcher
2022, 2023, 2025	European Space Agency, the Netherlands, visiting researcher
2021–2025	Estonian Student Satellite Foundation, CEO, earlier public relations manager
2021	Solar Car Estonia, photovoltaics and electronics engineer
2020–2021	Enefit Connect, smart grid engineer
2017–2020	Science Centre AHHAA Foundation, planetarium and activities specialist
2016	Waste water treatment plant of Tartu, plant intern

6. Participation in conferences and summer schools

2025	Luxembourg Space Resources Week
2025	Winter Satellite Workshop, Helsinki, Finland. Oral presentation
2024	Next Generation High Efficiency Photovoltaics (NEXTGEN) International School and Workshop, Mallorca, Spain. Oral presentation
2024	International Astronautical Congress, Milan, Italy. Oral presentation
2024	European Materials Research Society Spring Meeting, Strasbourg, France. Oral presentation

2024	EuroScience Open Forum, Katowice, Poland
2024	Luxembourg Space Resources Week. Oral presentation
2023	International Astronautical Congress, Baku, Azerbaijan.
2023	International Conference on Materials for Advanced Technologies (ICMAT), Singapore. Oral presentation
2023	Graduate School of Functional Materials and Technologies (GSFMT), Tartu. Poster presentation
2023	Luxembourg Space Resources Week. Poster presentation
2022	Graduate School of Functional Materials and Technologies (GSFMT), Tallinn. Poster presentation
2022	Graduate School of Functional Materials and Technologies (GSFMT), Pärnu
2022	International Astronautical Congress, Paris, France. Oral presentation
2022	Luxembourg Space Resources Week. Oral presentation
2021	International Astronautical Congress, Dubai, United Arab Emirates. Oral presentation
2021	European Materials Research Society Spring Meeting, virtual conference. Recorded presentation

7. Honours and awards

2025	Women in Science Fellowship, the Estonian Academy of Sciences
2024	Laureate, "Science in 3 minutes" competition of the Estonian Academy of Sciences
2024	Science popularization of the year, TalTech School of Engineering
2023	TalTech Development Fund award, Riigi Kinnisvara AS scholarship
2022	TalTech Development Fund award, Mati Jostov scholarship
2021	TalTech scholarship for academic excellence
2020	TalTech Development Fund award, Ilmar Öpik scholarship
2020	Rotalia Student Corporation award

8. Supervised dissertations

Mia-Maria Meldorf, Master's student, (sup) Katriin Reedo; Taavi Raadik, Deposition of Nickel Oxide thin Films by Chemical Bath Deposition, Post-Treatments and Characterization, Tallinn University of Technology, 2025

Annaly Gutjuma, Master's student, (sup) Katriin Reedo; Taavi Raadik, Synthesis-Growth and Phosphorus Doping of Pyrite FeS_2 Microcrystals for Monograin Layer Solar Cells, Tallinn University of Technology, 2025

Art Ra Jalakas, High School student, (sup) Katriin Reedo, Deposition and Characterization of Nickel Oxide Films, Rocca al Mare School, 2022

9. List of publications

1. **K. Reedo**[*], T. Raadik, M. Altosaar, A. Gutjuma, P. Paaver. "Scalable Phosphorus Doping of p-Type FeS_2 Microcrystals for Photovoltaic Applications", *ACS Omega*, 2025. DOI: 10.1021/acsomega.5c07455.

2. **K. Kristmann**[*], T. Raadik, M. Altosaar, M. Danilson, J. Krustok, P. Paaver, Y. Butenko. "Characterization of FeS_2 pyrite microcrystals synthesized in different flux media", *Materials Advances*, 5, 1565, 2024. DOI: 10.1039/d3ma00697b.

3. A. Slavinskis, M. F. Palos, J. Dalbins, P. Janhunen, M. Tajmar, ..., **K. Kristmann** et al. "Electric Sail Test Cube–Lunar Nanospacecraft, ESTCube-LuNa: Solar Wind

Propulsion Demonstration Mission Concept", *Aerospace*, 11, 3, 2024.
DOI: 10.3390/aerospace11030230.

4. **K. Kristmann***, T. Raadik, M. Altosaar, M. Grossberg-Kuusk, J. Krustok, M. Pilvet, V. Mikli, M. Kauk-Kuusik, A. Makaya. "Pyrite as promising monograin layer solar cell absorber material for in-situ solar cell fabrication on the Moon", *Acta Astronautica*, 199, 420-424, 2022. DOI: 10.1016/j.actaastro.2022.07.043.

5. **K. Kristmann***, M. Altosaar, J Raudoja, J. Krustok, M. Pilvet, V. Mikli, M. Grossberg, M. Danilson, T. Raadik. "Pyrite as prospective absorber material for monograin layer solar cell", Thin Solid Films, 743, 139068, 2022. DOI: 10.1016/j.tsf.2021.139068.

Elulookirjeldus

1. Isikuandmed

Nimi	Katriin Reedo
Sünniaeg ja -koht	26. august 1995 Jõhvi, Eesti
Kodakondsus	Eesti

2. Kontaktandmed

Aadress	Tallinna Tehnikaülikool, Materjali- ja Keskkonnatehnoloogia Instituut, Ehitajate tee 5, 19086 Tallinn, Estonia
E-post	katriin.reedo@taltech.ee

3. Haridus

2021–2026	Tallinna Tehnikaülikool, Keemia-, materjali- ja energiatehnoloogia, doktoriõpe
2019–2021	Tallinna Tehnikaülikool, Materjalid ja protsessid jätkusuutlikus energeetikas, MSc *cum laude*
2014–2018	Tallinna Tehnikaülikool, Tööstusökoloogia, BSc
2017	Viana do Castelo Polütehniline Instituut, Portugal vahetusüliõpilane

4. Keelteoskus

eesti keel	emakeel
inglise keel	kõrgtase
saksa keel	algtase

5. Teenistuskäik

2021-2026	Tallinna Tehnikaülikool, nooremteadur
2022, 2023, 2025	Euroopa Kosmoseagentuur, Holland, külalisteadur
2021–2025	Eesti Tudengisatelliidi Sihtasutus, tegevjuht, varasem kommunikatsioonijuht
2021	Solar Car Estonia, päikeseenergia ja elektroonikainsener
2020–2021	Enefit Connect, tarkvõrgu insener
2017–2020	Teaduskeskus AHHAA, planetaariumigiid ja tegevusjuhendaja
2016	Tartu Veevärk, veepuhastusjaama praktikant

6. Konverentsidel ja suvekoolides osalemine

2025	Luxembourg Space Resources Week
2025	Winter Satellite Workshop, Helsingi, Soome. Suuline ettekanne
2024	Next Generation High Efficiency Photovoltaics (NEXTGEN) International School and Workshop, Mallorca, Hispaania. Suuline ettekanne
2024	International Astronautical Congress, Milaano, Itaalia. Suuline ettekanne
2024	European Materials Research Society Spring Meeting, Strasbourg, Prantsusmaa. Suuline ettekanne
2024	EuroScience Open Forum, Katowice, Poola

2024	Luxembourg Space Resources Week. Suuline ettekanne
2023	International Astronautical Congress, Baku, Aserbaidžaan.
2023	International Conference on Materials for Advanced Technologies (ICMAT), Singapur. Suuline ettekanne
2023	Graduate School of Functional Materials and Technologies (GSFMT), Tartu. Poster ettekanne
2023	Luxembourg Space Resources Week. Poster ettekanne
2022	Graduate School of Functional Materials and Technologies (GSFMT), Tallinn. Poster ettekanne
2022	Graduate School of Functional Materials and Technologies (GSFMT), Pärnu
2022	International Astronautical Congress, Pariis, Prantsusmaa. Suuline ettekanne
2022	Luxembourg Space Resources Week. Suuline ettekanne
2021	International Astronautical Congress, Dubai, Araabia Ühendemiraadid. Suuline ettekanne
2021	European Materials Research Society Spring Meeting, virtuaalne konverents. Salvestatud ettekanne

7. Autasud

2025	"Women in Science" stipendium, Eesti teaduste akadeemia
2024	"Teadus 3 minutiga" võistluse laureaat, Eesti teaduste akadeemia
2024	Aasta insenerivaldkonna populariseerija, TalTech, inseneriteaduskond
2023	TalTech Arengufond, Riigi Kinnisvara AS stipendium
2022	TalTech Arengufond, Mati Jostovi nimeline stipendium
2021	TalTech tulemusstipendium
2020	TalTech Arengufond, Ilmar Öpiku nimeline stipendium
2020	Korp! Rotalia stipendium

8. Juhendatud lõputööd

Mia-Maria Meldorf, magistrikraad, (juh) Katriin Reedo; Taavi Raadik, "Nikkeloksiidi kilede vesilahusest sadestamine, järeltöötlused ja karakteriseerimine", Tallinna Tehnikaülikool, 2025

Annaly Gutjuma, magistrikraad, (juh) Katriin Reedo; Taavi Raadik, "Püriitsete FeS_2 mikrokristallide süntees-kasvatus ja fosforiga legeerimine monoterakiht-päikesepatareides kasutamiseks", Tallinna Tehnikaülikool, 2025

Art Ra Jalakas, keskkool, (juh) Katriin Reedo, "Nikkeloksiidi kilede sadestamine ja uurimine", Rocca al Mare Kool, 2022

9. Publikatsioonid

Teadusartiklite loetelu on toodud inglisekeelse elulookirjelduse juures.